



Thesis submitted to obtain the title of
Doctor of Philosophy

École Doctorale des Sciences Pour l'Inénieur
Field: Computer Science

Toward Real-Time Simulation of Aneurysm Coil Embolization Using the Discrete Exterior Calculus Method

Prepared by Yiyi WEI at
SHACRA, INRIA Lille and LIAMA, CASIA
Defended on 26th March 2012

Advisors: **Stéphane COTIN**
Research Director at SHACRA Team, INRIA Lille
Songde MA
Professor at LIAMA, Institute of Automation, Chinese Academy of Sciences

Reviewers: **Francis LEBOEUF**
Professor at LMFA, Ecole Centrale de Lyon
Matthias HARDERS
Senior researcher and lecturer at Computer Vision Lab, ETH Zurich

Examiners: **Irène E. VIGNON-CLEMENTEL**
Research Scientist at REO Team, INRIA Paris Rocquencourt
Alejandro F. FRANGI
Professor at Department of Mechanical Engineering, University of Sheffield

President: **Christophe CHAILLOU**
Professor at LIFL, Université des Sciences et Technologies de Lille

ACKNOWLEDGMENTS

This thesis ends a wonderful journey of my Ph.D study with the people who have supported and helped me during the last few years. Nevertheless, my gratitude to these colleagues, friends and family members will never fade. The impressive experience will be a priceless treasure throughout all my life.

Among these people, I would like first thank Prof. Songde Ma, Prof. Chunhong Pan and Prof. Christophe Chaillou. Without their efforts, I would not have this great opportunity to pursue the fun of scientific research and to study in two different countries. They dedicated plenty of time to discussing and defining a promising and interesting Ph.D subject for me, and made the co-tutorial program possible. During these years, they have been concerned about both my work and my life. I really appreciate what they have done for me.

I owe a debt of gratitude to my supervisor Stéthane Cotin. You have a deep and wide understanding of the entire field. Whenever I felt lost, you could always stand at a higher level to understand the difficulty we met. Nevertheless, the main reason I admire you is not only the professional knowledge you have, but more importantly, is the way you think, which has influenced me deeply. I still remember exactly several casual talks we had when I prepared the manuscript. You mentioned more than once that the goal of a thesis was not to show a perfect solution to a problem, because people seldom could do that; the essential was to present what problems we have found, what efforts we have made, and what potential solutions could be. You told me the thesis was not the end of my research, but the beginning of my work in the next ten or twenty years, so it was more valuable to open a door for my future research, rather than to write a conclusion. Lot of students considered the several months' writing just as a final step to get the degree. You let me make this step more meaningful both for me and for other peers. You also talked about your understanding of the defense, which was a good chance to discuss with the experts and benefited both sides, but not a final exam for Ph.D student. Eventually, my defense turned out to be such a success, which allowed us to discuss several key problems in my thesis, as well as future cooperation based on my Ph.D work. Besides, I really appreciate how you regard the relation between professors and students; they are friends, they are equal collaborators. And this was also the way in which you treated your students. In my mind, it is still a clear picture of we climbing over the iron fence of IRCICA when we worked together for the MICCAI deadline till the gate was locked. You never forgot to say thank you for every work I did, and made me feel my efforts had been recognized and respected. And this feeling encouraged me to discuss any of my ideas with you, even rambling and immature ones. You were quite busy but always energetic. Although during your super busy days, you still made time to exchange our thoughts. Even after a whole day's traveling, you came to talk to me in the evening before you left for home. Your such strong sense of responsibility urged me to do better, better and better. Moreover, you never hesitated to support me to do the things which were good

for me. You approved of collaborating with Fang Le in Lyon, with Pierre Alliez in Nice to solve the problems I met. The help from these experts helped me make a great progress efficiently.

Actually you acted not only as a supervisor, but more like a wise and considerate friend. You always considered the situation from my point of view, and gave suggestions which were most favorable for me. When I was unhealthy in the second year, you gave me no stress for my work and emphasized that the health was most important for me. I cannot write down all the memories of working with you in these years, because there are too many, and too many. I can neither express all my thankfulness to you, because there are too much, and too much.

Besides, I would like to thank Jérémie Allard and Le Fang, who made a great contribution to this thesis, and gave me lots of professional and technical advices and suggestions.

I would like to thank Jérémie Dequidt and Christian Duriez for helping me solve the difficulties in my work and finish the manuscript.

I would like to thank Juan Pablo de la Plata, Frédérick ROY, Frédéric Château. You are so excellent engineers. You were always patient to help me solve all the computer problems.

I would like to thank Jean-Philippe Deblonde, Olivier Comos, Hadrien Courtecuisse and Vincent Majorczyk, who shared the lab of "petit lapin" with me. Thank you very much for sharing ideas in our work and helping my living in France. I will never forget the stories happened in the house of "petit lapin".

I would like to thank Anne Rejl for taking your time to arrange my stay in Lille, my travel, and all the things for my thesis and defense.

I would like to thank all my French colleagues for making me feel comfortable in a country far away from my hometown, and of course the Welsh you recommended!

I would like to thank Pierre Alliez and Stephane Tayeb in Sophia Antipolis for supporting me to create a mesh generator plugin in SOFA.

I would like to thank Haifeng Gong and Huaiyu Wu for leading me to the road of this research. Your initial guide was indispensable in my following work. I would like thank all the other Chinese colleagues in LIAMA for sharing their knowledge with me and helping me deal with all the things when I was away.

I want to express my gratitude to Francis Leboeuf and Matthias Harders for taking your time to review my manuscript, as well as all the other jury members, Irène E. Vignon-Clementel, Alejandro F. Frangi, and Christophe Chaillou for attending my defense.

Finally, I am really grateful for my parents, who unconditionally supported me to pursue my study. I am sorry I did not spend too much time with you in the last four years, especially every transitional Chinese new year. I know you did care so much, but still comforted me to let me know you had a good time by yourselves. You were worried about my health and my life when I was sick. I hope this thesis can be a gift for you to express my thankfulness to you.

ABSTRACT

Toward Real-Time Simulation of Aneurysm Coil Embolization Using the Discrete Exterior Calculus Method

Abstract: Over the last decade, remarkable progress has been made to treat cerebral aneurysm with endovascular strategies, essentially using platinum coils. Yet, coil embolization remains a very complex operation which requires careful planning and advanced skills in order to be successful. In this context, a computer-assisted system, allowing physicians to interactively select and test different coils in a patient-specific environment, could make a difference. This involves modeling the vascular structure, medical devices, but also blood flow and its interaction with coils.

We introduce the Discrete Exterior Calculus method to hemodynamic simulation for the first time, along with a series of experiments to understand its accuracy, stability and computational efficiency. More importantly, we improve the numerical stability by optimizing meshes and using advanced backtracking schemes. We also apply several techniques for accelerating the computation. Based on this fast method, we propose a new approach for patient-specific and real-time simulation of coil embolization, from mesh generation to computation of blood-coil bilateral interactions, first involving the impact of flow on the coil during its deployment, and second concerning the decrease of blood velocity within the aneurysm. This allows dynamical planning for two key steps: choice and placement of the first coil, and assessment of coil packing. Our simulated results demonstrated that the bilateral influence is essential in the surgery planning. Besides, we propose a preliminary framework for the simulation of blood-vessel interaction during aneurysm growth, which shows encouraging results in the two-dimensional case.

Keywords: real-time medical simulation, aneurysm coil embolization, discrete exterior calculus, blood flow simulation, fluid-structure interaction

RÉSUMÉ

Vers La Simulation Temps-Réel de l'Embolisation d'un Coil dans un Anévrisme par l'Utilisation de la Méthode du Calcul Extérieur Discret

Résumé: Des progrès ont été réalisés ces dix dernières années dans le traitement des anévrismes via des procédures endovasculaires avec des coils détachables. L'embolisation reste une procédure médicale complexe qui requiert une planification minutieuse et des compétences techniques avancées. Dans ce contexte, un simulateur permettant aux radiologistes de choisir et tester différents coils pour un patient donné est pertinent. Une telle approche nécessite la modélisation du réseau vasculaire, des outils chirurgicaux, du flux sanguin et de son interaction avec les coils.

Nous introduisons la méthode du calcul extérieur discret pour la simulation hémodynamique. Nous avons amélioré la stabilité numérique en optimisant la qualité des maillages. Nous décrivons également un processus complet de la simulation d'embolisation: la génération de maillages à l'aide d'images médicales jusqu'au calcul de l'influence réciproque sang-coil. Nous proposons une nouvelle approche en deux phases pour la simulation de ces interactions, d'abord en prenant en compte l'influence du flux sanguin sur le déploiement du coil, puis en diminuant la vitesse du sang dans l'anévrisme. Cette approche permet une planification interactive pour deux étapes clés de la procédure: choix et placement du coil suivi d'une estimation du nombre de coils à introduire pour réduire la vélocité du sang dans l'anévrisme. Nos résultats de simulations démontrent que l'influence réciproque est essentielle. Enfin, nous proposons une approche préliminaire pour la simulation de l'interaction sang-réseau vasculaire lors de la formation d'un anévrisme. Les résultats de la simulation 2D en utilisant des données patients sont encourageants.

Mots-clés: simulation médicale en temps réel, l'embolisation d'un coil dans un anévrisme, calcul extérieur discret, simulation de flux sanguin, l'interaction fluide-structure

LIST OF PUBLICATIONS

Below is the list of my publications which were produced during my PhD study between 2008 and 2012.

Book

- [1] Y. Wei and S. Cotin. *Aneurysm: A (Near) Real-Time Simulation Method of Aneurysm Coil Embolization, in progress*. InTech, 2012, ISBN 980-953-307-299-4

Journal

- [1] Y. Wei, S. Cotin, J. Allard, L. Fang, C. Pan and S. Ma. *Interactive blood-coil simulation in real-time during aneurysm embolization*. Computers & Graphics, 2011

Conference Paper

- [2] Y. Wei, L. Fang, S. Cotin and S. Ma. *Interactive Blood-Coil Simulation using Discrete Exterior Calculus*. International Conference on Vortex Flows and Vortex Models–ICVFM, 2010
- [3] Y. Wei, S. Cotin, L. Fang, J. Allard, C. Pan and S. Ma. *Toward Real-Time Simulation of Blood-Coil Interaction during Aneurysm Embolization*. Medical Image Computing and Computer-Assisted Intervention–MICCAI 2009, pages 198–205, 2009

CONTENTS

Contents	viii
List of Figures	xi
List of Tables	xii
1 Introduction	1
1.1 Thesis Organization	1
1.2 Background in Medical Simulation	1
1.3 Aneurysm Related Research	3
1.3.1 Aneurysm	4
1.3.2 Treatment	5
1.3.3 Current Researches	8
1.4 Challenges in Computer-Based Simulation	13
1.5 Our Contributions	16
2 Discrete Exterior Calculus Approach	17
2.1 Computational Fluid Dynamics	17
2.1.1 Physical Model: The Navier-Stokes Equations	19
2.1.2 Numerical Approaches	21
2.2 Primal and Dual Complexes	26
2.2.1 Simplicial Complex	26
2.2.2 Dual Complex	29
2.2.3 Discretization of the Space	33
2.3 Discrete Forms	35
2.4 Operators	36
2.4.1 Hodge Star	36
2.4.2 Discrete Exterior Derivative	37
2.5 Implementation	39
2.5.1 Representation of Meshes	39
2.5.2 Discrete Forms and Operators	40
3 Blood Flow Simulation	45
3.1 Physiological Fluid Dynamics	45
3.1.1 Geometry Model	46
3.1.2 Hemodynamic Simulation	47
3.2 Mesh Generation	49

3.3	Numerical Solution	54
3.3.1	Discretization	55
3.3.2	Solving Fluid Equations	57
3.4	Accelerating Techniques	60
3.4.1	Limit Mesh Resolution	60
3.4.2	Optimize Linear Solvers	62
3.4.3	Improve Backtracking Algorithms	62
3.4.4	Improve Stability	62
3.5	Experiments and Results	63
3.5.1	Experiments of Two-Dimensional Simulation	63
3.5.2	Experiments of Three-Dimensional Simulation	76
3.5.3	Computational Time	81
3.6	Discussion	83
3.6.1	Mesh Quality	83
3.6.2	Computational Efficiency	86
4	The Simulation of Blood-Structure Interaction	89
4.1	Introduction	89
4.1.1	Fluid-Structure Interaction	89
4.1.2	Aneurysm Coil Embolization	91
4.1.3	Aneurysm Growth	94
4.2	Blood-Coil Interaction	96
4.2.1	Modeling Blood-Coil Interaction	96
4.2.2	Real-Time Simulation of Coil Embolization	99
4.2.3	Results	100
4.3	Blood-Vessel Interaction	103
4.3.1	Overview of the Method	104
4.3.2	Blood Pressure Computation	105
4.3.3	Brain and Vessel Tissues Modeling	106
4.3.4	Creep Modeling	106
4.3.5	Results	107
4.4	Discussion	108
5	Conclusion and Perspectives	111
5.1	Conclusion	111
5.2	Perspectives	112
5.2.1	Accuracy and Stability	112
5.2.2	Boundary Conditions	113
5.2.3	Computational Efficiency	114
5.2.4	Validation	114
5.2.5	Other Applications	115

References

117

LIST OF FIGURES

1.1	Locations and shapes of aneurysms	4
1.2	Grafting	6
1.3	Clipping and coiling	7
2.1	Orientation of simplices	28
2.2	Induced orientation	28
2.3	The circumcentric subdivision of a triangle	31
2.4	Primal and dual meshes in two dimensions	31
2.5	Primal and dual elements in three dimensions	32
2.6	Example of orienting a dual cell in two dimensions	33
2.7	Induced orientation of dual cells	33
2.8	Examples of discrete primal forms	36
2.9	Transition between forms	39
2.10	Example of a single tetrahedron	41
2.11	Different possibilities of dual edges in non well-centered meshes	42
3.1	Mesh generation from patient-specific data	47
3.2	BCC-based tiling strategy	50
3.3	Meshing a cuboid using the BCC-based tiling strategy	51
3.4	Meshing a cylinder by the CWC tiling strategy	52
3.5	Examples of dual elements in the cylinder model	53
3.6	Examples of low-quality dual elements in the aneurysm model	54
3.7	Backtracking	59
3.8	Geometry model of the T-junction vessel	64
3.9	Comparison of velocity field on the vessel model	65
3.10	Comparison of velocity profiles on the vessel model	66
3.11	Mesh resolution and kinetic energy of the vessel model	66
3.12	Geometry model of the large-neck aneurysm	67
3.13	Geometry model of the small-neck aneurysm	67
3.14	Comparison of velocity field on the large-neck aneurysm model	68
3.15	Comparison of velocity profiles on the large-neck aneurysm model	69
3.16	Comparison of velocity field on the small-neck aneurysm model	69
3.17	Comparison of velocity profiles on the small-neck aneurysm model	70
3.18	The variation as the time step size increases	72
3.19	Comparison on the vessel model between different backtracking schemes and different time step sizes	73

3.20	Comparison on the large-neck aneurysm model between different backtracking schemes and different time step sizes	74
3.21	Comparison on the small-neck aneurysm model between different backtracking schemes and different time step sizes	75
3.22	Comparison of velocity field on two simple geometries	77
3.23	Comparison of velocity profiles on two simple geometries	78
3.24	Mesh resolution and kinetic energy of the cuboid model	78
3.25	Comparison on two simple geometries between different backtracking schemes and different time step sizes	79
3.26	Comparison of velocity field on the patient-specific aneurysm model .	80
3.27	Hodge-optimized triangulation	86
4.1	The shape of detachable coils before and after deployment	97
4.2	Partition of the aneurysm volume	100
4.3	Coil embolization of a small aneurysm	101
4.4	Coil embolization of a large aneurysm	101
4.5	Simulation of coil embolization	102
4.6	The influence the blood flow on coil deployment	103
4.7	Mesh acquisition process	104
4.8	Overview of the approach	105
4.9	Simulation of aneurysm growth on two patient data sets	107

LIST OF TABLES

3.1	Mesh quality of the vessel model	64
3.2	Mesh quality of the large-neck aneurysm model	70
3.3	Mesh quality of the small-neck aneurysm model	70
3.4	Mesh quality and kinetic energy of the cylinder model	76
3.5	Mesh quality and kinetic energy of the patient-specific aneurysm model	81
3.6	Computational time	81
3.7	FPS	82

INTRODUCTION

1.1 Thesis Organization

The thesis is composed of five chapters. Chapter 1 provides the background of medical simulation, in particular the aneurysm related researches, then describes the main challenges in this field and our contributions. Chapter 2 discusses the problem of computational fluid dynamics and its numerical solutions, particularly focuses on the theory of Discrete Exterior Calculus (DEC), along with its implementation. Chapter 3 presents the DEC method for blood flow simulation, including mesh generation, numerical solution and accelerating techniques, as well as a detailed analysis of the results and discussion of the method. Chapter 4 describes the complete frameworks for patient-specific simulation of blood-coil interaction during aneurysm coil embolization, and blood-vessel interaction during aneurysm growth, respectively. In the end, Chapter 5 offers the summary of our work, discusses the remaining limitations and forecasts the potential directions for further improvements.

1.2 Background in Medical Simulation

Medical care has been a branch of sciences for thousands of years, since it highly relates to human being's daily life, helping people to alleviate sufferings, to prevent and cure diseases, as well as to fight death. These cares are required to have minimal impact on patients, leaving little or no room for error. Yet, despite the important development of medical science and related technologies over the last few decades, patient safety remains a major objective of modern medicine. The 1999 Institute of Medicine report, *To Err is Human* [Kohn et al. (1999)], highlighted the high prevalence of medical errors and their impacts on patient safety in the USA. The report concluded that between 44,000 and 98,000 people died each year as a result of preventable medical errors, costing nearly 9 billion dollars in health care expense. Moreover, several novel and complicated treatments

have been developed during recent years, especially minimally invasive procedures, where instruments are introduced into the patient's body through small incisions, such as laparoscopic surgery, interventional radiology, and therapeutic endoscopy. Although the minimally invasive procedure presents several advantages compared to traditional surgery (e.g., a quick recovery of the patient), it places an additionally burden upon the physicians. As a consequence, the need for reducing the occurrence of medical error has been augmenting.

Medical simulations provide an elegant solution to the current need for better medical treatments. Simulation is able to reproduce or represent the phenomena, under test conditions, which are likely to occur in actual performance. Medical simulation is attractive, since it allows trainees to experience realistic patient situations which involve widely varying clinical contents, and to repeatedly practice without exposing patients to the risks inherent in trainee learning. Even for professional surgeons, medical simulations are also helpful to provide preoperative surgical practices aiming at individually patient-specific cases, and the prediction and assessment of the patients' situation after the operation. In addition, simulated surgical operations might then be optimized by a stored data set of movements and replicated with robotic assistance in the real operation [Krummel (1998)] [Chauhan et al. (2011)]. Furthermore, with innovative haptic interface devices and virtual reality technologies, tele-medicine is realizable.

The first idea of medical simulation dates back to as early as 200 AD, which was a model of human body proposed by the Greek physician Galen. Then Leonardo Da Vinci, Andreas Vesalius and other scientists followed him to provide further clarification and refinement of human body models [Kunkler (2006)]. Not until the 1980s, academic and research organizations started to focus on replicating body's normal functioning in a more life-like manner. During these ten years, several mannequins came out as man-made living bodies, including the famous Harvey mannequin as a cardiology patient simulator, and a computerized mannequin designed for anesthesia response by Michael Good and his co-workers [Cooper and Taqueti (2008)]. Nowadays, mannequins were not only physiologically precise, but near human likeness in skin, texture and so on, such as the new iSTAN mannequin [Neil (2009)].

A few years after the introduction of virtual reality (VR) technology by Jaron Lanier [Blanchard et al. (1990)] the first training systems for medicine were developed. Scott Delphand and Joseph Rosen created a representation of the lower limb, which was used for practicing tendon repair and predicting the effect of this procedure [Delp et al. (1990)]. This is also the earliest example of using a surgical simulator for preoperative surgical rehearsal. Dr. Richard Satava and Jaron Lanier then created a simulator based on a graphic drawing of the organs of the upper abdomen [Satava (1993)]. Although it was extremely crude

and simplified, and contained a very limited amount of interactivity, it led the computer-based simulation to a wider range of applications, such as the cholecystectomy simulator KISMET [Kuehnappel and Neisius (1993)], the wound simulator to teach debridement and suturing [Satava (2008)], the simulator for minimally invasive surgery MIST-VR [Wilson et al. (1997)]. As a result of the development of medical imaging techniques, such as Computerized Tomography (CT) scan, Magnetic Resonance Imaging (MRI), the use of patient-specific model became prevalent in the simulation. The hysteroscopy simulator developed by Jeff Levy, could import actual patient data from CT scans, and allowed to practice multiple different surgical approaches and optimize each patient's operative procedure [Levy (1996)]. The liver surgery simulation using patient-specific data sets of liver lesions was designed for preoperative planning as an execution of surgical technique [Marescaux et al. (1998)]. With the ongoing advances in both computer and medical graphics, software design and hardware manufacture, more and more functions have been added into medical simulators, such as motion tracking of hands and eyes [Datta et al. (2001)].

Several commonly admitted benefits have brought increasing attention to the area of medical simulation in recent years. Prior to the advent of medical simulators, traditional alternatives for medical training and planning were animals (which in some instances greatly differed in anatomy), cadavers (which could not provide living reaction to physician's movement), and patients (which suffered potential risks). On the contrary, an ideal medical simulator offers configurable and realistic training environments without exposing patients to eventual errors, and overcomes the problem of waiting for availability of suitable traditional training resources or real-life cases. Furthermore, They allow easy access to a wide variety of clinical scenarios, including new techniques, procedures and instruments. Nevertheless, the cost of using modern medical simulators is often less than the cost entailed in the number of hours that instructors must spend in training residents and the expense of supplies and resources required in the training.

1.3 Aneurysm Related Research

In this PhD study, we do not cover all the aspects of medical simulation. Instead, we concentrate on the computation-based simulation of physiological fluid and its interaction with other structures (e.g., tissues or medical instruments). Currently, our research is focused on the issues related to the aneurysm disease.

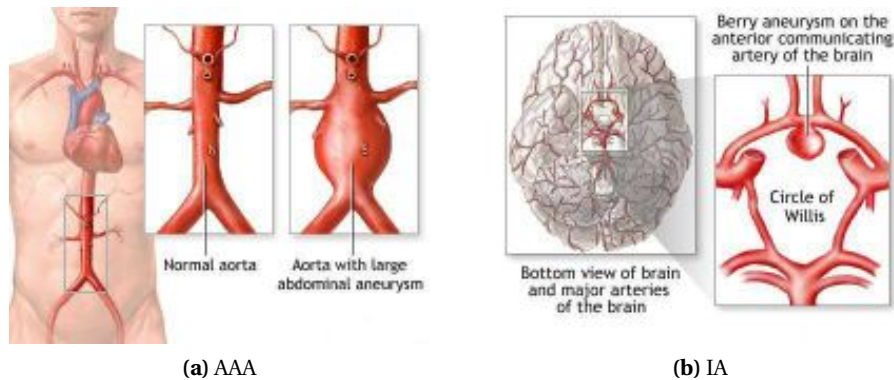


Figure 1.1: Locations and shapes of aneurysms. (a) An abdominal aortic aneurysm (AAA) is when the large blood vessel, which supplies blood to the abdomen, pelvis, and legs, becomes abnormally large or balloons outward. (b) A common location of intracranial aneurysms (IA) is in the arteries at the base of the brain, known as the Circle of Willis. (Images from <http://www.nlm.nih.gov>)

1.3.1 Aneurysm

Aneurysm is abnormal widening or ballooning of a portion of blood vessel wall. More precisely, aneurysm is defined by a permanent dilatation of 50% or more compared with the expected normal diameter of the vessel [Johnston et al. (1991)]. Aneurysms are usually found in the abdominal and thoracic portions of the aorta, which are the largest artery in the body starting from the left ventricle of the heart and extending down to the abdomen. And they also locate in the cerebral arteries surrounding the Circle of Willis, which are rather small vessels in the brain. The abdominal aortic aneurysm (AAA) is commonly in fusiform shape, while the intracranial aneurysm (IA) is usually in saccular shape (Figure 1.1).

The health impact of AAA is not readily apparent. Because the majority of patients suffer nothing over many years, while IA may cause fatigue, loss of perception or balance, speech or vision problems, etc. Besides, another associated problem is blockage in the blood circulation, since thrombus may form within the dilated aneurysm, and a fragment of this blood clot may tear off and travel with the blood stream. Nevertheless, the most serious symptom appears when the aneurysm grows larger, thus the vessel gets thinner and finally leads to a significant risk of rupture. If the rupture happens, the hemorrhage causes rapid decrease of blood pressure, fainting, sense of an impending doom, and shock, which could be fatal. The rupture of cerebral aneurysm causes the hemorrhage in brain and severe headache, and leads to disability of senses, stroke (paralysis, coma) and/or death.

The prevalence of aneurysms was approximately estimated to be 1% of the

adult population, and it was reported that the prevalence increased with age [Komotar et al. (2008)]. More precisely, AAA was found in 5.0% of men and 1.5% of women older than 65 years of age [Ballard et al. (2008)]. In the UK and the Netherlands the risk of rupture was estimated to be the order of 1/10,000 people annually [Dillon et al. (2007)] [Boll (2008)]. The prevalence of IA ranged from 2% to 6% in adults in Japan, and rupture rate was estimated to be 1%, subarachnoid hemorrhage was presumed to occur in 20 to 60 patients per 100,000 people each year [Akiyama et al. (2010)]. Although the rupture did not happen to most of the patients, the mortality after rupture was considerably high; the death happened to 80% of the patients reaching hospital and 50% of patients who were undergoing surgery for emergency repair [Cosford and Leng (2007)].

The high mortality of aneurysm rupture has been at all times urging people to explore the causes of aneurysm in order to prevent and treat this fatal disease. But it is not clearly enough what exactly induces aneurysm. It is proposed that defects in some parts of the artery wall may be responsible. Among these defects, some are believed to be the result of congenital or inherited weakness in artery walls, while other risk factors include increasing age, male gender, hypertension, atherosclerosis, high cholesterol, tobacco use, alcoholism, copper deficiency and so on [Annambhotla et al. (2008)].

1.3.2 Treatment

The inadequately understood causes of aneurysms have left us lots of difficulties in prevention and treatment of this disease. Generally, it is suggested to follow a healthy diet, get regular exercise, control high blood pressure, maintain a healthy level of cholesterol, and keep away from cigarette and alcohol. Once aneurysm is diagnosed, there is no drug to shrink the ballooned out artery to the normal state, since it is an anatomic or structural pathology. Instead, patients can resort to different preventative treatments. The choice of treating strategies depends on the risk assessment by the size, growth rate and location of aneurysm, as well as status of the patient. Once aneurysm is ruptured, the patient needs to take the emergency treatment immediately, which leaves so little room for teaching and operative errors that only experts do this. Undoubtedly, preventative treatment is a preferred option. Surgeries are merely recommended if the risk of rupture is thought to be obviously higher than operation failure. They require careful planning and extensive training, which simulation can greatly help.

The preventive treatment cannot absolutely cure all the patients, as rupture may still happen several years after the surgery. In case of rupture, patient should be rescued as soon as possible to stem bleeding and repair the aneurysm. Usually, emergency operations are based on the same principles as preventative operations.

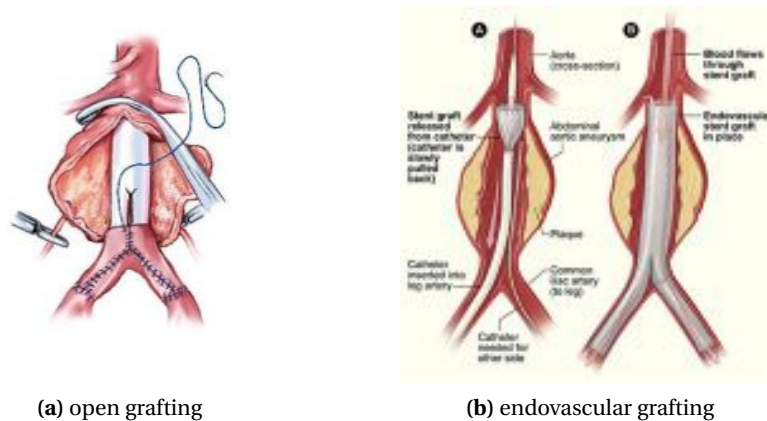


Figure 1.2: Grafting. (a) A sutured graft or (b) an endovascular stent graft is placed in an AAA. (Images from <http://www.stevens.edu> and <http://www.hearthealthywomen.org>)

The most commonly used surgical intervention for aortic and peripheral aneurysms is grafting (Figure 1.2). The weakened segment of the vessel is removed, and replaced by a piece of synthetic tube, known as graft, which is sutured at the vascular stumps and bridges the gap. Alternatively, instead of sewing, the graft tube ends, made by rigid and expandable nitinol wireframe, can be easily inserted into the vascular stumps in a reduced diameter, then expand up to the most appropriate diameter and be permanently fixed there by external ligature [Nazari et al. (1996)]. There are other newly developed devices to substitute the external ligature by expandable ring, which allows the use in acute ascending aorta dissection, as well as provides airtight, easy and quick anastomosis extended to the arch concavity [Nazari (2010)]. Grafting can be done by either open surgery or endovascular surgery. In an open surgery, the aorta is exposed and the graft is inserted through a large incision which is made in patient's abdomen, while endovascular surgery involves inserting a thin flexible tube, called delivery catheter, into the femoral artery (in patient's leg). Dye flows through this catheter so that the artery can be seen on medical images, which helps physicians to advance the catheter in the vascular network to reach the position of aneurysm. The graft is then delivered through the catheter and deployed at the site of aneurysm. Afterwards, the catheter is withdrawn from the femoral artery. Obviously, endovascular surgery is minimally invasive, and allows a quicker recovery time, especially suitable for those who are under other unwell health conditions. Moreover, research also suggested that, compared to the open surgery, it offered a slightly better chance of reducing the risk of death caused by aneurysm rupture. Nevertheless, it is associated with more complications and needs for monitoring or even re-intervention. In an addition, it was reported that long-term results after endovascular repair were worse for large

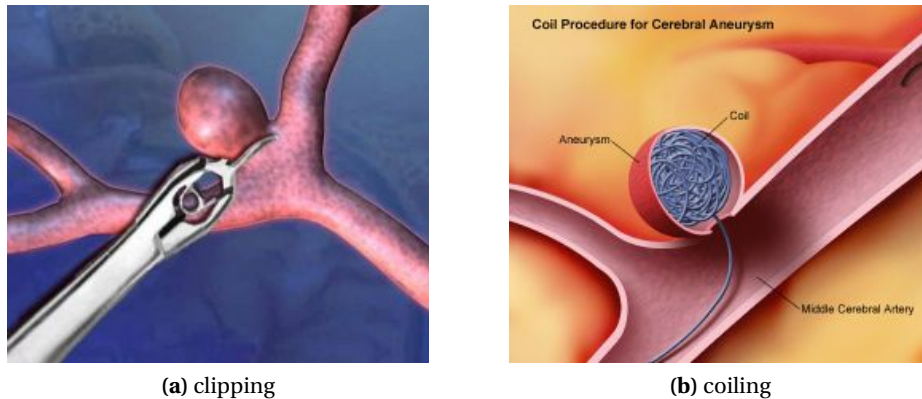


Figure 1.3: Clipping and coiling are two successful surgical strategies used for treating IAs. (Images from <http://www.microvention.com> and <http://www.yalemedicalgroup.org>)

aneurysms, which were most in need of repairs [Wilt et al. (2006)].

As for IAs, several surgical techniques has proved a great success: neurosurgical clipping, endovascular coiling and stenting (Figure 1.3). Clipping is carried out under patient's general anesthesia by craniotomy, which means an incision is made in the scalp, and a small piece of skull is removed to reveal the brain underneath. When the aneurysm is located, the surgeon seals the aneurysm from the normal blood circulation by placing a tiny metal clip across the aneurysm neck. After the bone is replaced at the initial position, the scalp is stitched together. Thus, the clip remains permanently on the artery, and prevent the blood flow from entering the aneurysm. It is believed that surgical clipping remains the best method to permanently eliminate aneurysms. But it is difficult to perform if the neck of aneurysm is wide. More importantly, because of its invasiveness, risk of complications and danger of death during or shortly after surgery, people always resort to another alternative, endovascular embolization. Similar to the endovascular grafting, this procedure also starts with the insertion of a catheter and advancement to the brain aneurysm. Instead of graft, physician delivers some filling material through the catheter into the cerebral aneurysm, such as small plastic particles, glue, metal coils, foam, or a balloon. The presence of obstructer in the aneurysm reduces blood flow into it, and decreases the wall pressure against the aneurysmal wall, thus progressively creating a favorable hemodynamic environment for flow stasis and thrombus embolization. Finally, the formation of a blood clot blocks off the aneurysm, thus considerably reducing the risk of rupture. In the case of irregularly shaped or fusiform aneurysms, or aneurysms with wide necks, stenting of the parent artery can be used in combination with coils.

1.3.3 Current Researches

Due to the high mortality of aneurysm rupture and the difficulties existing in the treatments, great attention has been paid on the researches related to aneurysm involving multiple disciplines, such as clinicopathology, pathophysiology, genetics, biomechanics, and computer science.

1.3.3.1 Aneurysm Evolution

The formation and growth of aneurysm involve a series of extremely complex pathological changes and biomechanical processes, and still remain poorly understood at present. It is generally believed that the process is associated with local hemodynamic impact, degradation of arterial wall and the local environment.

Several clinical reports highlighted the pathogenic significance of hemodynamic conditions on AAA progression. A number of studies meanwhile indicated the close relationship between high wall shear stress (WSS) and the initiation of cerebral aneurysm formation, growth and rupture [Shojima et al. (2004)]. The repeated trauma of a reflected arterial wave may contribute to pathologic fragility of the wall, and cause the arterial wall to be incapable of resisting the expansile force of each systolic contraction. Then continuous aneurysm expansion leads to increasing arterial wall tension or stress, which, in turn, contributes to more enlargement of the aneurysm dome.

Regarding the angioarchitecture, elastic fibers and fibrillar collagens are two determining factors of arterial mechanical properties. Elastin and associated proteins form a network of elastic fibers responsible for the viscoelastic properties, while collagens provide tensile strength and help maintain the structural integrity of the vascular wall [Sakalihan et al. (2005)]. The loss of elastic fibers seems to be an early step in aneurysm formation. Ultimately, collagen degradation leads to the aneurysm rupture [Dobrin and Mrkvicka (1994)].

When expanding, aneurysm could touch the surrounding anatomical elements, such as cranial nerves, bridging and surface veins, small arteries. The contact between growing aneurysms and other structures may cause not only nerve symptoms by the adhesive compression, but also the deformation and bleb formation of the aneurysm dome due to the limitation in spatial expansion. These extrinsic factors also play a role in the growth and rupture of aneurysms [San Millán et al. (2002)] [Satoh et al. (2005)]. In Section 4.3, our simulation of aneurysm development not only considers the interaction between blood and vessel, but also includes the surrounding tissues as an impact.

Rupture is a mechanical failure when the stress experienced by the vessel wall exceeds wall strength. Not all aneurysms end in rupture; some of them grow slowly and stop expanding when reaching a certain size. So far, it is still impossi-

ble to accurately predict where and when the rupture will take place. Researches only proposed several guidelines for rupture assessment, such as the morphological parameters, location, growth rate of aneurysm, and patient's age, gender, family history, and health conditions.

It has been universally recognized that the maximum diameter of aneurysm is an important factor to forecast rupture since the 1960s [Szilagyi et al. (1966)]. Usually, an IA exceeding 10 mm in diameter is deemed to have higher possibility of rupture [Dhar et al. (2008)]. Nevertheless, the real controversy exists in assessing small aneurysms. Several reports demonstrated that some aneurysms in fact ruptured at an unusually small size [Beck et al. (2003)]. The relationship between the rupture risk and aneurysm size still remains to be elucidated. Recently, instead of size metric, more comprehensive morphological characteristics were applied to describe the dimension and shape of aneurysm, such as non-spherical (both elliptical and multilobed) shape, size ratio, aneurysm angle, parent vessel geometry [Dhar et al. (2008)]. Growth rate is another assistant metric to predict rupture. Rapid expansion of aneurysm diameters preceding rupture was observed in IAs independently of their initial sizes [Juvela et al. (2001)]. As a result, it is suggested that the size of aneurysm, whatever its practical significance, is probably not the sole useful determinant for rupture assessment. Since the rupture is the result of interaction between blood flow and wall vessel, hemodynamics also plays a significant role in the assessment. Flow rate, blood pressure, wave form, hemodynamic forces are usually observed to monitor aneurysms. Some studies demonstrated that the ruptured IAs had unstable flow patterns, smaller impinging jet diameters, and smaller impingement zones [Cebal et al. (2005)], as well as a higher average wall shear stress in the sac [Shojima et al. (2004)], compared to the unruptured aneurysm.

1.3.3.2 Hemodynamics

Hemodynamic factors are thought to play an important role not only in all the stages of aneurysm life cycle, i.e., initiation, growth, and rupture, but also in clinical evaluation and treatment. The pathogenesis is highly relevant to the hemodynamic forces, among which there are three major components associated with aneurysm evolution: (1) hydrostatic pressure, the perpendicular force acting on the vascular wall; (2) relative wall strain (RWS), the circumferential stretch of the vessel wall caused by pressure changes due to cyclical systolic contractions and the resulting tensile stress; (3) wall shear stress (WSS), the tangential force exerted by moving blood along the axis of flow. The arteries and aneurysms pulsate under repetitive blood pressure over years, and the composition of the wall and strength may degrade because of material fatigue. In recent years, great progresses were made in studies of pressure and WSS obtained in vivo [Bieg-

ing et al. (2011)], experimentally [Takeuchi and Karino (2010)] and theoretically [Baek et al. (2010)].

Historically, a geometrical model of vessel and aneurysm was established, and the hemodynamics within and around the aneurysm was studied by experimental flows [Strother et al. (1992)]. However, a better method for evaluating aneurysmal flow would be in vivo analysis, and some novel techniques of angiography made it possible to assess blood velocity in human arteries by using particle imaging velocimetry and laser Doppler velocimetry [Tateshima et al. (2007)], or by ultrasound beams to achieve noninvasive and simultaneous assessment in real time [Tortoli et al. (2006)]. Complex arterial flow patterns were readily visible by flow-sensitized four-dimensional MRI and three-dimensional phase-contrast MRI [Wetzel et al. (2007)]. But these velocity data was still far away from the ideal information for aneurysm analysis, which required high spatial and temporal details and complete three-dimensional coverage including the adjacent arteries, particularly in intricate anatomical structures. This is almost impossible for conventional angiography at present. As a result, computational simulation, combined with medical imaging techniques, becomes attractive for studying patient-specific hemodynamic conditions. It allows very detailed flow field representations, and provides any required flow quantities, such as vorticity and wall shear stress. More detailed computational simulation result has motivated lots of researches to investigate its use in the diagnosis and treatment of aneurysm, and prediction of aneurysm evolution. Nevertheless, computer-based method usually requires profound numerical knowledge, as well as enormous computational power and time. The survey revealed that clinicians only showed an interest in computational simulation of blood flow, but still lacked awareness concerning the role of computer simulation in aneurysm related research [Singh et al. (2009)]. Consequently, computer-based simulation, which has a great potential, has to be more deeply investigated for future clinical use.

Cerebral aneurysms appear at different locations, such as carotid and basilar artery. The hemodynamic quantities were speculated to be partially dependent on aneurysm positions according to the comparison of values in cerebral aneurysms at different positions [Chien et al. (2009)]. Another important effect on hemodynamics is the geometry of either aneurysm or parent artery. For example, faster flow velocity and higher WSS were observed in the relatively small aneurysms and aneurysms with wider neck [Tateshima et al. (2010)]. Significant increase of WSS was detected in the aneurysm lateral to the curve of the parent artery compared to the one inside or outside the curve of the artery, even with the same shape of the aneurysm [Sato et al. (2008)]. So it is important to accurately define the patient-specific geometry of aneurysm and parent vessels.

Thanks to modern angiography techniques, patient-specific geometry

model can be reconstructed, and used in simulations or experiments to analyze hemodynamic parameters in a cerebral artery before and after the formation of aneurysm (e.g., [Mantha et al. (2006)]), and to compare hemodynamic characteristics qualitatively or quantitatively between unruptured and ruptured aneurysms (e.g., [Cebal et al. (2011)]). These studies were aimed at learning the association between the hemodynamics and the whole life cycle of aneurysm, and finally discovering the pathogenesis of aneurysm. Besides, a significant contribution of hemodynamics to the aid and assessment of surgeries can be expected. WSS and pressure distribution is useful to estimate the risk of rupture, and to determine whether a preventive surgery is necessary and urgent for the patient. Hemodynamic environment can be theoretically reproduced and then applied to treatment planning (e.g., [Kakalis et al. (2008)]) or treatment rehearsal (e.g., [Wei et al. (2009)]). After the treatment, the comparison between the post-operative and pre-operative status of hemodynamics can be used to evaluate the effect of the operation and the patient's safety (e.g., [Fu et al. (2010)]).

1.3.3.3 Artery

It is being perennially debated among researchers whether aneurysm is initialized by hemodynamic stimuli that could induce a degenerative response on the arterial wall, or by degeneration of the vessel wall itself. The recent consensus is inclined to believe that aneurysm evolves as a result of an extremely complex interplay between hemodynamic factors and biomechanical process of artery degrading triggered by inherited biochemical and structural defects, aging, infection or diseases. Besides the studies on local hemodynamic environment in the vessel or around the aneurysm, there has been a large amount of work devoted to the biological and mechanical studies on the artery, as well as mathematical and physical model of the vessel wall.

As a basis of further research on the underlying mechanism of artery deformation, the biological structure of arterial wall represents a significant area to be explored. The wall is usually composed of three layers [Fung (1993)], some of which may be exceptionally very thin or absent in certain intracranial arteries [Lee (1995)]. It is a complex biological structure of living cells, and a structural network of sheets and fibers of polymerized proteins, whose compositions and constructions (partially) control the degree of elasticity and stiffness. These cells and fibers respond to the mechanical stimuli from the internal blood flow or external organs by actively modifying their mechanical properties. But more importantly, they are responsible for permanent transformations (i.e., remodeling) by adjusting their morphological characteristics, compositions or organization as a result of biological processes. Actually, this is a feedback control system to maintain the stability of the integral body. The mechanism of artery remodeling

is one of key problems to study the association between aneurysm evolution and biological processes, such as, degenerative processes, infection, aging, etc. The biological factors responsible for aneurysm have been widely investigated from cellular level to molecular level, from biomechanic field to genetic field.

The theoretical studies demonstrated the difference of hemodynamics between simulations using rigid and elastic wall models, and obviously the superiority of elastic model regarding the reality [Zhao et al. (2008)] [Zhao et al. (2009)]. As a result, it is necessary to study the mechanics of the vessel wall not only for its own deformation, but also for a more realistic local hemodynamic environment.

Above all, the mechanical properties (for example, elasticity, viscoelasticity, stiffness, contractility, wall thickness) of arteries should be measured in order to establish the mechanical model. With present noninvasive medical imaging techniques, it is still hampered to measure in vivo patient-specific mechanical properties and the nonuniform distribution of wall thickness [Lasheras (2007)]. Thus, measurements were usually made by experiments on artery or aneurysm samples from autopsy [MacDonald et al. (2000)]. These properties were also studied with regard to the changes during the normal course of aging [Hayashi et al. (1980)], since they varied as the vessel undergoes long-term remodeling under the coupling between mechanical stimuli and the biological processes. Mechanically, the formation of aneurysm is considered as a process of fatigue failure. This is a typical problem in structural engineering, involving the plastic deformation, permanent bulging, and subsequent rupture of a pipe under the effect of an oscillatory internal pressure caused by periodic blood ejection from heart into aorta. In mechanical field, the deformation is commonly explained with the instability theory of structure, while the rupture is explained with the strength theory of material. Among the diverse mechanical aspects of aneurysm evolution, there are many clinical and laboratory researches focused on characterizing the constitutive equation quantifying the relationship between the wall stresses and the strain response of blood vessels, such as simple linear elastic model, pseudoelastic model, randomly elastic model, poroelastic model, and viscoelastic model [Vito and Dixon (2003)]. The response to the WSS within vessel or aneurysm was widely recognized to be significant to control the aneurysm evolution, except for IAs, where, rather than WSS, tensional stresses was thought to be the determinant factor [Lasheras (2007)].

A lots of mathematical and physical models for aneurysm mechanics are available in the literature, including hyperelastic model to examine the mechanical response of the arterial wall under the combined action of inflation, axial extension, and torsion [Ren and Yuan (2010)], an AAA failure model based on the constitutive theory of softening hyperelasticity, coupled with a growth model by phenomenological theory of soft tissue [Volokh and Vorp (2008)], a thin shell model of a saccular aneurysm to describe the shape deformation when interact-

ing with a viscous interior fluid [Calvisi et al. (2010)]. Finally, the mathematical models are solved by numerical techniques which are implemented on computer.

1.4 Challenges in Computer-Based Simulation

Although the rapid development has taken place in the area of medical simulation for tens of years, it still remains lots of fundamental problems to be solved for a wide and reliable use of computer-based simulation in clinical trails and treatments. An ideal medical simulator is supposed to provide interaction between the physician and the patient's anatomy in a clinically realistic manner. The virtual tissues are supposed to move as they do in a living body, for example, the heart beats, the blood flows. As well, the tools should be able to interact with these moving tissues, but not simply move above them. So that the physiological and physical responses of the body to interventions such as cutting, suturing, probing, and dilating must be realistic. The realism means not only in visual sense but also in haptic or even acoustical sense, which requires the color, texture, physical properties to reflect the simulated tissues. As a result, a realistic medical simulator is an offspring of multiple disciplines, that is, an integration of state-of-the-art solutions in areas, which are as diverse as visualization, biomechanical modeling, haptic and contact modeling. Besides, some other crucial challenges for now are not technical in the area of computer science, but to understand the value and proper application of the new technology, to determine the metrics for validating and assessing medical simulators, and to set standards for evaluating trainee's performance as well. Here we discuss some main challenges of computer-based medical simulations in general, and more specifically, the difficulties in the simulations concerning cerebral aneurysm, such as blood flow around aneurysm, pulsatile deformation of arterial wall, evolution of aneurysm, interaction between operative instruments and patient's tissue or organ. Such simulations are expected to understand the pathogenesis and progression of aneurysm, to predict rupture, to train residents or to rehearse medical procedures. However, lots of them are still far from being capable of functioning as a reliable tool to guide the clinical management of aneurysm, despite multidisciplinary effort over years.

Geometry Modeling Although the patient-specific geometry model can be obtained by reconstruction from medical images, these images can neither provide a high resolution nor avoid the noises due to the current restrictions of imaging techniques and image processing tools. Consequently, a precise description of three-dimensional geometry is not always available. The fusiform AAA in large size can be reconstructed with relatively good accuracy. But a precise geometri-

cal model of IA is more difficult to obtain because of its small size and complex network of surrounding arteries, especially when taking into account the exact curvature and connectivity to parent and daughter arteries [Lasheras (2007)].

Physiological and Physical Modeling Human body is such a complicated system, no matter in geometrical, physical or physiological aspect, that it still leaves thousands of mysteries to current researchers. One of important technical challenges consists in acquiring accurate measurements in vivo, such as kinematics, biochemical, and physiologic parameters, and physical properties. Even if some parameters of individual organs and tissues are not too difficult to measure, it is still an enormous labor to collect all the essential measurements to represent the properties and physiologic processes accurately, and then to integrate them into an overall simulation. A further complication is the case that each individual is more or less alike, but still quite different in detail. For the purpose of realism, patient-specific data becomes a necessary trend in medical simulation. Moreover, it is a task that could never be completed, since it will always be possible to reach another level of fidelity: initially from the organ and tissue level, to the glandular level, then to the cellular level, and finally to the molecular level and beyond. With each level succeeded, the realism will be further improved.

To model the artery, the real deficiencies stem from the current difficulty in obtaining personalized biological or mechanical properties of vessel wall in vivo. It is a challenge to resolve the distribution of nonuniform wall thickness throughout the entire aneurysm, and even more difficultly, the precise composition and structure of the wall at each location. And the results obtained from experiments suggested that the estimation of the mechanical properties was mainly influenced by the image spatial resolution and the chosen registration configuration, thus the reliability of current measuring methods was doubtful [Balocco et al. (2010)]. Furthermore, these characteristics not only differ in individuals, but also vary over time and position inside the identical body. The inadequacy of biomechanical parameters together with the complication of poorly understood physiological processes makes it challenging to establish a physical model including all important factors.

Data Acquisition Up-to-date imaging techniques are incompetent to provide images with a high resolution either in space or in time. This brings about difficulties in acquiring important hemodynamic information of living bodies, such as blood flow pattern, velocity. Particularly, WSS is difficult to measure as it is derived from the velocity close to the wall where most conventional imaging techniques are least reliable [McGregor et al. (2009)]. The lack of actual hemodynamic information in vivo hampers in vitro simulation from accurately approximating to the reality. For example, it is still controverted what proper initial

and boundary conditions for simulations of blood flow and wall deformation are. Acquiring such data, which is time-varying and transient, for each inlet and outlet is impractical. As a result, physical and mathematical models are required to be established [Vignon-Clementel et al. (2010)].

Interaction Most simulations concern the computation of not only visual rendering but also interactions between medical devices and anatomical structures. Generally speaking, these interactions involve detection of collisions between objects, and response to deformation and collision. Finally, the resulting state of interactions is visually and haptically rendered. Usually these simulations target at assisting in making a rapid decision or rehearsing in a virtual environment, thus require fast or even real-time computation, which cannot always be guaranteed by modern computers with certain limitations both in memory and frequency. Therefore, the need still remains to increase computing speed by both optimizing algorithms and improving hardware.

Validation and Assessment Before put to wide clinical utilization, the medical simulation should be validated and assessed to make sure that the simulation is accurate and effective; otherwise, it is useless in a clinical sense. However, current techniques (e.g., the difficulty in data acquisition) somehow hinder us from comparing numerous simulations to the actual state on a real patient, sometimes also between pre-operative and post-operative statuses. In addition, standardized and reliable validation techniques are needed, and further efforts to develop validation methodologies should be made.

Evaluation of Performance As a training tool for residents, it is important to evaluate their performance on the surgical procedure, and to determine whether they are proficient and qualified in this specific operation. At present, we still lack sufficient evidence to support the reliability of assessments of medical student's performance using the simulator as an evaluation tool. Developing the metrics for evaluating performance is also a problem demanding prompt solution.

Visualization Efforts must be made to create high-quality visuals that effectively convey the real world to the user. Realism could be achieved in the field of data visualization by using appropriate rendering, including colors, textures, brightness, shadows, refraction, transparency, refraction, diffraction, etc. Additionally, speed (especially for the volume rendering) and interactivity are also important issues, as the rendering speed of one image directly affects interactivity of visualization, for example, zoom and rotation in real time, which could happen in the navigation of medical instruments and other simulated processes.

1.5 Our Contributions

In this thesis, we present a theoretical approach, Discrete Exterior Calculus (DEC), initially developed in the field of computer graphics, along with its practical implementation. This new approach is introduced to hemodynamic simulation for the first time, in order to achieve accurate and fast (real time or near real time) computation of the blood flow and blood-structure interaction in specific applications. To this end, we introduce several improvements as well as a much deeper analysis of the results, in the context of very different applications than initially aimed by the DEC method.

- We improve the numerical stability of the method by using more advanced backtracking schemes, and more importantly by optimizing quality of the mesh used in the computation.
- A detailed analysis of the results and comparison with a reference software are performed to understand the stability, accuracy and computational efficiency of the method, as well as the factors affecting these aspects.
- We add extra terms to the Navier-Stokes equations in order to describe the interaction between blood and the deformable surgical instruments during the procedure of aneurysm coil embolization.
- While the existing studies of aneurysm embolization only concerned the impact of the deployed coil(s) on the blood flow, we also propose an effective way to compute the reverse effect of the blood flow on the coil during the surgery, and provide higher reality for the simulation of placing coils into the aneurysm compared to the case without considering the interaction with blood flow.
- Our simulated results of blood-coil interaction show that our approach permits to describe the influence between coils and blood flow during coil embolization, and that an optimal trade-off between accuracy and computational time can be obtained.
- We propose a new approach for modeling the development of aneurysm based on computationally efficient numerical techniques for solving both the fluid simulation and the soft tissue deformation problems. In addition, we consider the influence of the soft tissues surrounding the vessels in aneurysm growth, and rely on a creep model for describing the interactions between fluid and tissues as they involve very different time scales. Our simulations in two-dimensional space using actual patients data sets provide encouraging preliminary results.

DISCRETE EXTERIOR CALCULUS APPROACH

In this chapter, after a brief historical review over the topic of computational fluid dynamics in Section 2.1, we mainly introduce a newly developed numerical tool for solving fluid equations, which is the discrete exterior calculus approach. In Section 2.2, a differentiable manifold, where we do exterior calculus, is discretized as a manifold-like oriented simplicial complex (referred to as primal mesh) and a corresponding dual mesh. In Section 2.3, discrete forms, which are the objects to represent discrete physical variables, are presented. Afterwards the transition between forms by two fundamental operators is explained in Section 2.4. Finally, in Section 2.5, we show the implementation of the DEC theory is quite understandable and approachable for engineers.

2.1 Computational Fluid Dynamics

In physics, fluid dynamics is a discipline that deals with fluid flow, and understands the physical events that occur in the flow of fluids (liquids or gases) around and within designated objects. These events are related to the action and interaction in the phenomena such as dissipation, diffusion, convection, slip surfaces, turbulence. The solution to a fluid dynamics problem typically involves calculating various characteristics of the fluid, such as velocity, pressure, density, and temperature, as functions of space and time. The research of this discipline was initially motivated by the development of aircraft industry in the 1930s. In the following years, the fluid dynamics has continuously made new academic theories and new models, which have brought more and more applications in a number of various industrial fields.

Generally speaking, there are three basic approaches that can be employed to solve fluid dynamics problems, experimental approach, analytical approach, and computational approach. Traditionally, both experimental approach and analytical approach are applied to study various aspects of fluid dynamics and to assist engineers in the design of equipments and industrial processes involv-

ing fluid flow. Thanks to the advent of digital computer in the early 1950s, the modern computational fluid dynamics (CFD) provides another alternative to the traditional approaches. Although experiments continue to be significant and the analytical method is still practiced, the trend is obviously towards dependence on CFD for industrial applications, especially in some complex cases.

CFD is a new branch of science integrating not only the disciplines of fluid dynamics with mathematics but also the field of computer science. The physical properties of the fluid motion are described through fundamental mathematical equations, normally in a partial differential form. These equations which govern a flowing process of interest, are often called governing equations in CFD. In many cases, the partial differential equations can be approximated by a series of discrete equations which are then converted by computer scientists using high-level programming languages into computer programs or software packages. Finally, the results calculated by the computer, called numerical solutions, are considered to be an approximate solution to the original equations.

CFD becomes more and more appealing in both fluid dynamics area and industrial design, since it offers a lot of outstanding benefits.

1. CFD is a method based on physical theoretical model (i.e., the governing equations), and takes advantage of the academic findings which have been developed for over a hundred year. On the other hand, computer science then focuses on discretizing and solving the governing equations, and investigates various methods to approximate these equations.
2. CFD is a feasible alternative of simulating real fluid flows that completes the traditional approaches.
 - Experiments for the fluid simulation are usually time-costing and money-consuming, while CFD reduces preparing time and designing/producing cost, especially when the computing power of computers is increasing and the manufacturing cost of hardware is decreasing rapidly. Moreover, CFD is able to reproduce almost any scenarios and flow conditions, even a theoretically ideal situation, which is impossible for experiment-based methods.
 - Analytical approach only provides solutions to a limited amount of problems, while CFD has the capability of solving a wide range of complicated flow problems which lack analytical solutions.
3. CFD offers an easier method to simulate the fluid under different conditions by tuning the certain dimensionless parameters, such as, Reynolds number, Mach number, Rayleigh number. This attribute is very useful in the early periods of engineering design.

4. Compared to experimental and analytical fluid dynamics, CFD provides rather detailed and comprehensive results, which contain almost all the characteristics of the flow during the overall process of the simulation. Visualization of these results using vector fields, contours, and animated movies is an effective way to display the huge amount of data generated by numerical simulation.

Nevertheless, plentiful advantages that we benefit from CFD do not mean that traditional methods are going to disappear forever. Some engineering projects, especially in aircraft industry, are by far greatly dependent on experiments, for instance, wind tunnel experiments. Furthermore, there are many applications where CFD are relatively in its infancy of development, and the traditional approaches still remain as the primary source of information. For example, some complex flows, such as high Reynolds flow, turbulent flow, multiphase flows, boiling, and condensation, are governed by complicated nonlinear equations, and it is still difficult to numerically solve these governing equations using the state-of-the-art mathematical tools. What's more, numerical errors are irresistible in computations, and there is always difference between the CFD result and the reality. Last but not least, the difficulty for CFD also lies in setting boundary conditions. Under many circumstances, the CFD solution is highly dependent on the initial or boundary conditions, but there is no easy way to deal with these conditions in some cases. Take the blood flow simulation in small vessels for example, the flow distribution and pressure field in the modeled domain are not impractical to obtain from patients, thus no prescribed inflow or outflow can be used to set boundary conditions. An alternative approach is to couple the solution at the boundaries of the domain with other models of the downstream domain [Vignon-Clementel et al. (2010)] [Vignon and Taylor (2004)].

2.1.1 Physical Model: The Navier-Stokes Equations

As mentioned above, CFD approach is based on physical models, and represented by fundamental mathematical equations. Among these models, the Navier-Stokes equations are usually regarded as the basic governing equations of CFD, and widely used in researching and engineering. This set of equations is derived from the Newton's second law, that is, conservation of momentum, together with the assumption that the fluid stress is the sum of a diffusing viscous term (proportional to the gradient of velocity), plus a pressure term. The equations, are a milestone in the field of fluid mechanics, and named after Claude-Louis Navier and George Gabriel Stokes who made great contributions.

The standard Navier-Stokes equations given below (Equation 2.1) are used to describe the incompressible flows of Newtonian fluids whose stress is directly proportional to the velocity perpendicular to the direction of strain rate ($\partial v / \partial t$)

[Batchelor (2000)].

$$\begin{aligned}\rho \frac{\partial \mathbf{v}}{\partial t} + \rho(\mathbf{v} \cdot \nabla) \mathbf{v} &= -\nabla p + \mu \Delta \mathbf{v} + \mathbf{f}, \\ \nabla \cdot \mathbf{v} &= 0,\end{aligned}\tag{2.1}$$

where \mathbf{v} is the velocity vector, that is, (v_x, v_y) in two dimensions or (v_x, v_y, v_z) in three dimensions, of the fluid with density ρ and viscosity μ , p is the pressure, and \mathbf{f} is the external force vector (such as buoyancy, gravity, stirring), represented as (f_x, f_y) or (f_x, f_y, f_z) . The symbol ∇ is the vector of spatial partial derivatives, and we also use the notation $\Delta = \nabla \cdot \nabla$. More precisely, in two and three dimensions, these symbols are respectively

$$\begin{aligned}\nabla &= \left(\frac{\partial}{\partial x}, \frac{\partial}{\partial y} \right) & \Delta &= \frac{\partial}{\partial x^2} + \frac{\partial}{\partial y^2}, \\ \nabla &= \left(\frac{\partial}{\partial x}, \frac{\partial}{\partial y}, \frac{\partial}{\partial z} \right) & \Delta &= \frac{\partial}{\partial x^2} + \frac{\partial}{\partial y^2} + \frac{\partial}{\partial z^2}.\end{aligned}$$

In almost all the real situations, the Navier-Stokes equations are nonlinear partial differential equations; they can only be simplified to linear equations in a few specific cases, such as one-dimensional flow and Stokes flow. The nonlinearity is due to convective acceleration $(\mathbf{v} \cdot \nabla)\mathbf{v}$, which is an acceleration associated with the change in velocity over position. Generally speaking, the nonlinearity makes most problems difficult or even impossible to be solved. Hence, dealing with the term of convective acceleration is a key concern to solve the Navier-Stokes equations. The solution of these equations is a velocity field, a description of the velocity of the fluid at any given point in space and time. Once the velocity field is known, other properties of interest, such as pressure, flow rate, or drag force, can be further calculated.

The Navier-Stokes equations can be used to model both laminar and turbulent flow. Laminar flow occurs at relatively low velocities. Fluid tends to flow without either lateral mix, eddies or swirls of fluids. The motion of the fluid particles is so orderly that all particles move in straight lines parallel to the pipe walls, and adjacent layers slide past one another without cross currents perpendicular to the direction of flow. When the velocities increase (usually, it is estimated by Reynolds number, which goes over 2000 or 3000), the turbulent flow with chaotic behavior can be observed. The numerical solution of the Navier-Stokes equations for turbulent flow is extremely difficult, as a stable solution usually requires such a fine mesh resolution that the computational time becomes significantly impracticable for simulation. To model the turbulent flow, time-averaged equations (e.g., Reynolds-averaged Navier-Stokes equations) together with turbulence models are applied in practical CFD simulation.

2.1.2 Numerical Approaches

Lots of numerical approaches have been developed to solve differential equations. Many of them are based on three classical numerical methods, which are finite difference method (FDM), finite element method (FEM), and finite volume method (FVM).

FDM was proposed as early as 1910 by Richardson for the stress analysis of a masonry dam [Richardson (1911)]. This method is easy to understand and to formulate, so it is widely used in engineering till nowadays. The differential is approximated by forward, backward or central difference:

$$\begin{aligned}\left. \frac{dv}{dx} \right|_{x=x_i} &\approx \frac{v_{i+1} - v_i}{x_{i+1} - x_i} && \text{forward difference,} \\ \left. \frac{dv}{dx} \right|_{x=x_i} &\approx \frac{v_i - v_{i-1}}{x_i - x_{i-1}} && \text{backward difference,} \\ \left. \frac{dv}{dx} \right|_{x=x_i} &\approx \frac{v_{i+1} - v_{i-1}}{x_{i+1} - x_{i-1}} && \text{central difference.}\end{aligned}$$

Similarly, higher-order differential is written as, take forward difference as an example,

$$\left. \frac{d^2v}{dx^2} \right|_{x=x_i} \approx \frac{1}{x_{i+1} - x_i} \left[\left. \frac{dv}{dx} \right|_{x=x_{i+1}} - \left. \frac{dv}{dx} \right|_{x=x_i} \right].$$

Historically, FDM has dominated the CFD community due to its simplicity in formulations and computations. But for curved mesh, transformation into orthogonal Cartesian coordinates is the prerequisite; otherwise, finite difference equations cannot be written on structured Cartesian mesh. However, some new methods have extended FDM to satisfy unstructured mesh. Among these methods, DEC is a newly developed tool for solving differential equations discretized on triangular or tetrahedral mesh.

To compute on unstructured mesh, FEM is an alternative, first published in the Journal of Aeronautical Science to analyze aircraft stress in 1956 [Turner et al. (1956)]. Since then, both FDM and FEM have been widely applied in fluid dynamics, heat transfer, and other similar problems. In FEM, the problem domain is divided and approximated by a set of elements. On each element, the unknown variable $u(x)$ is approximated by a known function dependent on the geometrical location x , for example linear function or high-order polynomial function. The governing equations are transformed into a weak form by integrating over the whole domain, thus leading to a weak solution rather than a strong solution that represents the analytical solution. However, the underlying principles and formulations based on rigid mathematical theory are somehow a barrier for practical use.

Because of the simple data structure and the ability to handle unstructured mesh, FVM has become increasingly popular in recent years. Its formulations

can be derived from either FDM or FEM. Finite volume refers to the small volume surrounding each node point on the mesh, and volume integrals are converted to surface integrals, using the divergence theorem. These terms are then evaluated as fluxes at all the surfaces of each finite volume. Because the flux entering a given volume is supposed to be equal to the flux leaving the adjacent volume, FVM is conservative.

Besides these general approaches to numerically solving differential equations, there are also other methods and techniques specifically aimed at the computation of fluid flow. Hereby, we review some of them, including statistical methods, particle-based methods, vortex methods and the DEC method.

2.1.2.1 Statistical Methods

The Navier-Stokes equations are derived from macroscopic continuum mechanical theory, while other numerical approaches that have been developed lately model physics in fluids from a micro-scale or even nano-scale perspective. Among these approaches, we would like to briefly introduce two promising methods using statistical ideas to transfer micro-scale state to macro-scale value, which are Lattice Boltzmann Method (LBM), and Direct Simulation Monte Carlo (DSMC).

LBM is a simulation method based on the mesoscopic kinetic equations [Chen and Doolen (1998)]. The fundamental idea behind LBM is to establish a simple kinetic model that concerns only the essential physics of microscopic or mesoscopic processes, meanwhile, the macroscopic averaged quantities obey the desired macroscopic equations. The incompressible Navier-Stokes equations can be obtained in the nearly incompressible limit of LBM. This method has proved a good candidate for many applications, such as interface dynamics, boiling dynamics, and multiphase or multicomponent fluid flows, where traditional macroscopic methods cannot perfectly handle with.

DSMC is designed for some specialized flows with low-speed and high Knudsen number [Binder and Heermann (2010)]. Its basic idea is to track a large amount of statistically representative particles, and record their positions and velocities. In this method, particle motion is modeled deterministically, while the collision is treated statistically. DSMC is able to overcome some difficulties associated to the macroscopic methods in modeling unsteady flow, for instance, applications in computing non-equilibrium structure of shocks and boundary layers, as well as hypersonic viscous flows and high temperature rarefied gas dynamics.

2.1.2.2 Particle-Based Methods

In particle-based methods, the governing equations of fluid motion (e.g., the Navier-Stokes equations) are discretized using a set of moving particles and their interactions. The trajectories of particles are obtained by solving ordinary differential equations. Similarly, the evolution of properties carried by these particles, such as density, temperature, and vorticity, can also be calculated by solving other governing equations.

Particle-based methods are implemented using the Lagrangian formulation, usually without any mesh to describe the fluid space. This meshless strategy gets rid of the tedious task in meshing and remeshing processes, and is very attractive in lots of applications in the sense of simple description, easy implementation and intuitive user interaction. Moreover, it is also appropriate for large scale problems, multiphase flows, multiple fluids mixing and sedimentary flows. One popular method in under this category is smooth particle hydrodynamics (SPH) [Monaghan (2005)].

2.1.2.3 Vortex Methods

Vorticity, in an intuitive sense, explains the tendency of the fluid spinning; it measures the circulation per unit area at a point in fluid flow field. Mathematically, vorticity is also a vector field, defined as the curl of velocity field, $\boldsymbol{\omega} = \nabla \times \boldsymbol{v}$. The theorems of Helmholtz and Kelvin illuminate a natural fact that vorticity moves with the local velocity in the inviscid motion of a fluid, leading to a novel branch of methods for solving fluid flow problems, especially unsteady flow problems. Vortex methods essentially represent a direct translation of this fact into numerical algorithms, which formulate the Navier-Stokes equations in terms of vorticity (Equation 2.2). Therefore, vorticity field, instead of velocity field, is discretized as vortex elements, and the convection of each vortex element is tracked to simulate time evolution of the flow. Finally, velocity field is, in turn, converted from vorticity field by solving a Poisson equation, usually in terms of the Green's function or Biot-Savart integration.

$$\begin{aligned} \frac{\partial \boldsymbol{\omega}}{\partial t} + \mathcal{L}_v \boldsymbol{\omega} &= \frac{\mu}{\rho} \Delta \boldsymbol{\omega} + \frac{1}{\rho} \nabla \times \boldsymbol{f}, \\ \nabla \boldsymbol{v} &= 0 \quad \boldsymbol{\omega} = \nabla \times \boldsymbol{v}, \end{aligned} \tag{2.2}$$

where $\boldsymbol{\omega}$ is the vorticity, Lie derivative $\mathcal{L}_v \boldsymbol{\omega}$ (in this case equals to $\boldsymbol{v} \cdot \nabla \boldsymbol{\omega} - \boldsymbol{\omega} \cdot \nabla \boldsymbol{v}$), is the advection term. In two dimensions, the vorticity vector is perpendicular to the plane spanned by the fluid domain, and can be represented by signed scalars; the sign describes the either direction, while the magnitude measures the amount of circulation. In three dimensions, the vorticity is also a vector field

as velocity, $(\omega_x, \omega_y, \omega_z)$. The vorticity-based equations are deduced by taking curl of the Equation 2.1, and the pressure term disappears.

Obviously, vortex methods offer an easy way to analyze and visualize the development of vorticity field, and they get rid of the pressure term, which is only required to be solved when and where force measurements are desired. This feature simplifies the design of numerical algorithms to solve the Navier-Stokes equations. Furthermore, compared to traditional methods, vortex methods, to some degree, overcome the issues of numerical diffusion and instability by not directly approximating the convection term, thus result in higher accuracy and stability. More comprehensive introductions and reviews of the methods under this category are presented in [Cottet and Koumoutsakos (2000)].

2.1.2.4 Discrete Exterior Calculus

As a matter of fact, numerous physical theories have strong underlying geometrical structures, such as general relativity, electromagnetism (E & M), as well as solid and fluid mechanics. The best way to formulate these theories is to use simple geometric descriptions that formalize apparent symmetries and experimental invariants. Unfortunately, this intrinsic geometric nature is often concealed by the traditional formulations in coordinate system. On the contrary, the Exterior Calculus of Differential Forms, first proposed by Cartan, offered a better expression for plenty of physical and mathematical theories [Cartan (1947)]. The exterior calculus was extended and improved over the twentieth century, and became the foundation of the modern theory of differential geometry. In the end of last century, Sharpe stated that it was possible to express every differential by exterior derivative of differential forms [Sharpe (1997)]. As a result, several recent initiatives aimed at formulating the physical laws in terms of differential forms [Frankel (2004)].

Regarding the representation of physical variables, line integrals, as well as face and volume integrals are often used, for example, circulation along a closed loop in fluid mechanics or the line integral of electric field intensity in electromagnetism. So it is not proper to evaluate or approximate all the quantities uniquely pointwise, but more generally attached to a line, a surface or a volume. At the same time, these quantities should be stored and manipulated at their geometrically meaningful locations. Differential form is a good choice for such a geometrical description of physical quantities. The classical operations of gradient, divergence and curl, as well as the theorems of Green, Gauss and Stokes can be expressed concisely in terms of differential forms and operators on these forms called exterior derivatives.

Obviously, the geometry-based calculus has several advantages compared to the classical tensorial calculus. Firstly, it is the mother tongue of numerous phys-

ical and mathematical theories based on geometrical structures. Secondly, it is easier to discover invariants in the expression of differential forms by applying Stokes' theorem, Poincaré lemma, or by applying exterior differentiation.

There is always a significant gap between mathematical theories and applied sciences. Even though one has a comprehensive mathematical background, he will meet other obstacles, such as, discretization of the mathematical description. Some conventional discretization methods (for example, FDM or particle-based methods), focusing on accurately discretizing the local laws, usually lose important global structures and invariants. Later methods such as FEM, solved this problem to some extent by satisfying local conservation laws on average and preserving some important invariants. Although many important improvements have been made in error control, convergence, and stability of these finite approximations, the underlying structures of the simulated continuous systems are mostly destroyed. Some phenomena, such as gain or loss momentum of a moving rigid body, reveal that the discretization process usually fails to preserve some fundamental geometric and topological structures of the underlying continuous models. As a consequence, some recent scientists believed that we should think from a geometric point of view, and introduced some new concepts of DEC in a systematic way [Hirani (2003)].

Yet, the calculus of differential forms has not been widely applied in computational fields till now, except computational E & M community [Bossavit (2001)]. This community seems to have gone the furthest in the application of DEC-like ideas, because differential forms provide a perfect description of all Maxwell's equations. Afterwards, Desbrun and his coworkers presented some potential problems in the fields of computation vision and graphics, where DEC was applicable [Desbrun et al. (2003)], and they were pioneers in several applications: by using 0-forms to describe the coordinates of the surface, Tong created discrete harmonic forms for surface tiling [Tong et al. (2006)]; Fisher represented tangent vector fields as discrete 1-forms, i.e., scalars on edges, and generated such fields with user-assigned constraints over arbitrary triangle meshes [Fisher et al. (2007)]; Wang interpreted vertex- and face-based subdivision schemes as defining bases for 0- and 2-forms, and introduced edge-based subdivision schemes to construct the missing bases for 1-forms [Wang et al. (2006)]; Elcott described problem quantities, for example flux and vortex, as differential forms, and developed a strategy to preserve circulation along discrete loops in the mesh during the fluid simulation [Elcott et al. (2007)].

Although the theory of exterior calculus is not easy to manipulate for non-specialists, the discrete counterpart is much simpler to define and more intuitive to understand. In the following sections of this chapter, we do not offer a rigorous mathematical definition or deduction of the objects in DEC. Instead, we try to simply recall the fundamental definitions and theories needed to develop

a novel approach for fluid simulation. For more details about the DEC theory please refer to [Hirani (2003)].

2.2 Primal and Dual Complexes

The fluid domain is formalized as an n -dimensional manifold \mathcal{M} , which can be discretized as an n -dimensional simplicial complex satisfying certain conditions. In this section, we first review some fundamental definitions concerning simplicial complex and its dual cell complex, as well as the notion of orientation. Afterwards, discretization of the space is discussed.

2.2.1 Simplicial Complex

A p -simplex gives a general description of an element in the mesh (e.g., vertex, edge). Let $\{v_0, \dots, v_p\}$ be a set of geometrically independent points in the space \mathbb{R}^N , i.e., the vectors $\{v_1 - v_0, \dots, v_p - v_0\}$ are linearly independent.

Definition 2.1. A p -simplex σ^p is the convex hull of $(p + 1)$ geometrically independent points v_0, \dots, v_p :

$$\sigma^p = v_0 \dots v_p = \{x \in \mathbb{R}^N \mid x = \sum_{i=0}^p \mu_i v_i \text{ where } \mu_i \geq 0 \text{ and } \sum_{i=0}^p \mu_i = 1\}.$$

p is the **dimension** of the simplex. Any simplex σ^q ($0 \leq q \leq p - 1$) spanned by a subset of $\{v_0, \dots, v_p\}$ is called a q -**face** of σ^p , denote $\sigma^q < \sigma^p$. The union of these faces is called **boundary** of σ^p . $|\sigma^p|$ is the notation for p -**volume** of σ^p in \mathbb{R}^N . \diamond

Considering the simplex $\sigma^p = v_0 \dots v_p$ ($p \geq 1$), there are $(p + 1)$ faces of dimension $(p - 1)$. We can enumerate these faces by deleting one vertex each time, represented as $\sigma_i^{p-1} = v_0 \dots \hat{v}_i \dots v_p$ ($i = 0, \dots, p$), where the hat means omitting that vertex.

Definition 2.2. A **simplicial complex** K in \mathbb{R}^N is a set of simplices in \mathbb{R}^N satisfying:

1. Every face of a simplex of K is still in K .
2. The intersection of any two simplices of K is either a face of each of them, or empty.

The **dimension** of K is the largest number of dimension among all the simplices in K . Two p -simplices are called **adjacent** if they share a $(p - 1)$ -face. Two simplices are called **incident** if they intersect. \diamond

Definition 2.3. There are two equivalence classes of the vertex orderings in a simplex σ^p ($p \geq 1$). If two orderings differ from each other by an even permutation, they are equivalent, thus in the same equivalence class. Either class is called an **orientation** of σ^p . An **oriented simplex** is a simplex along with an orientation. We use $[v_0 \dots v_p]$ for an oriented simplex σ^p with the equivalence class of the ordering $(v_0 \dots v_p)$. Note that a 0-simplex has no orientation. \diamond

Definition 2.4. The orientation of $\sigma^p = [v_0 \dots v_p]$ ($p \geq 1$) defines an **induced orientation** for each $(p-1)$ -dimensional faces as follow: if i is even, the induced orientation of the face $\sigma^{p-1} = [v_0 \dots \hat{v}_i \dots v_p]$ is positive, written as $\text{sgn}(\sigma^p, \sigma^{p-1}) = +1$; otherwise, it is negative. \diamond

Definition 2.5. If two p -simplices σ_1^p and σ_2^p are adjacent with a shared $(p-1)$ -face σ^{p-1} , their orientations can be compared. We use **relative orientation** $\text{sgn}(\sigma_1^p, \sigma_2^p)$ of $+1$ or -1 to describe the comparison result. The positive means $\text{sgn}(\sigma_1^p, \sigma^{p-1}) = -\text{sgn}(\sigma_2^p, \sigma^{p-1})$ (in this equation, sgn represents induced orientation, which is not discriminated from the notation of relative orientation, since they are not confusing in a given context). The negative is on the contrary. \diamond

Definition 2.6. In a **manifold-like simplicial complex** K of dimension n , all p -simplices ($0 \leq p \leq n-1$) must be a face of some simplex of dimension n in the complex. Also, each point in K has an n -simplex neighborhood (i.e., all the incident n -simplices on this vertex) that has all the same topological properties of n -dimensional ball or half-ball. If the relative orientation of every pair of adjacent n -simplices is positive, we call K **oriented manifold-like simplicial complex**. \diamond

From now on, we will only work with oriented manifold-like simplicial complexes, referred to as **primal mesh**. In order to make the definitions above straightforward, we give some concrete examples which will be used later.

In the two-dimensional space \mathbb{R}^2 or three-dimensional space \mathbb{R}^3 , an oriented triangular or tetrahedral mesh can be considered as a *primal mesh*. We denote the the p -simplex set as follows:

$$0\text{-simplex (vertex) set: } V = \{\sigma_i^0 = v_i\},$$

$$1\text{-simplex (edge) set: } E = \{\sigma_{ij}^1 = e_{ij} = [v_i v_j]\},$$

$$2\text{-simplex (triangle) set: } F = \{\sigma_{ijk}^2 = f_{ijk} = [v_i v_j v_k]\},$$

$$3\text{-simplex (tetrahedron) set: } T = \{\sigma_{ijks}^3 = t_{ijks} = [v_i v_j v_k v_s]\},$$

($0 \leq i, j, k, s \leq |V|$, where i, j, k, s are serial numbers of vertices, and $|V|$ is the total number of vertices). The p -volume ($p = 0, 1, 2, 3$) is $|v_i| = 1$, $|e_{ij}|$ (length of the edge), $|f_{ijk}|$ (area of the triangle), or $|t_{ijks}|$ (volume of the tetrahedron), respectively. Note that we use the order of subscripts i, j, k, s to indicate the *orientation* of the simplex. 0-simplex v_i only has one possible orientation, while the others can be oriented in two opposite directions (Figure 2.1). The orientation of e_{ij} is

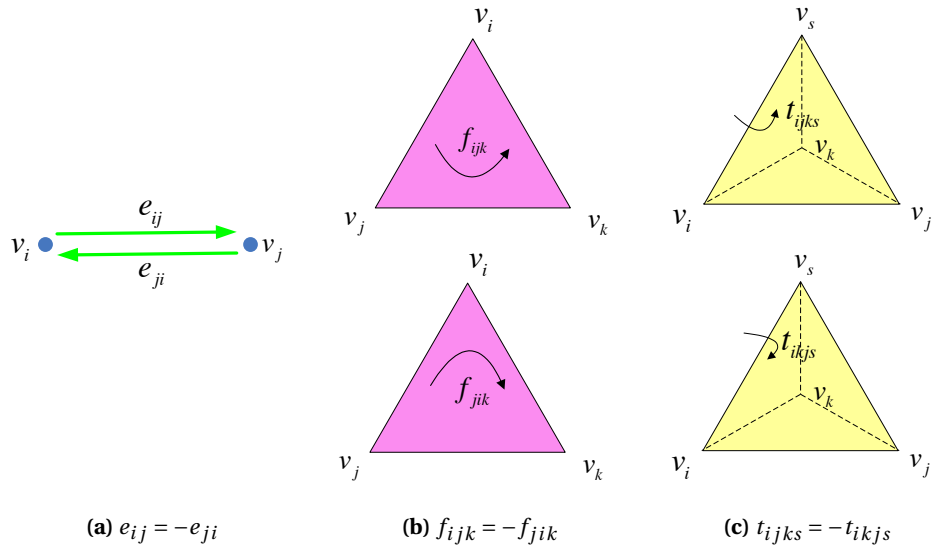


Figure 2.1: Orientation of simplices. (a) Two opposite directions of an edge; (b) clockwise and counter-clockwise orientations of a triangle; (c) right-handed and left-handed orientations of a tetrahedron.

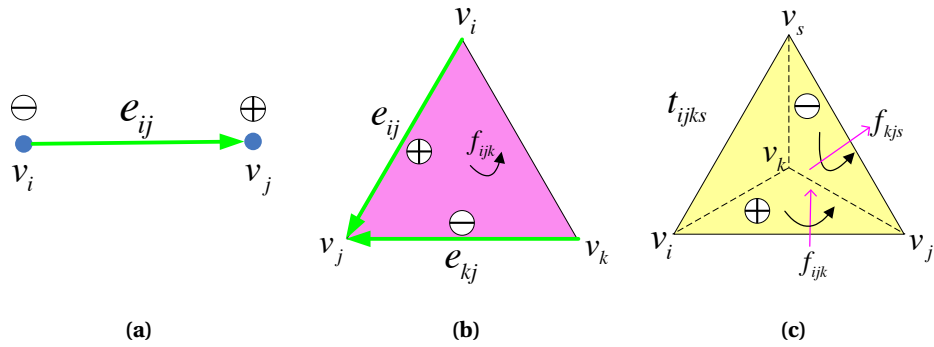


Figure 2.2: Induced orientation. (a) $\text{sgn}(e_{ij}, v_i) = -1$, $\text{sgn}(e_{ij}, v_j) = +1$; (b) $\text{sgn}(f_{ijk}, e_{kj}) = -1$, $\text{sgn}(f_{ijk}, e_{ij}) = +1$; (c) $\text{sgn}(t_{ijk_s}, f_{kjs}) = -1$, $\text{sgn}(t_{ijk_s}, f_{ijk}) = +1$, here t_{ijk_s} has right-handed orientation.

opposite to that of e_{ji} . The two orientations of a triangle can be explained intuitively as clockwise ($f_{ijk}, f_{jki}, f_{kij}$) or counter-clockwise ($f_{kji}, f_{ikj}, f_{jik}$). There are 24 orderings of 4 vertices, which can be classified into two sets by right hand rule: in $t_{ijk_s} = [v_i v_j v_k v_s]$, we define three vectors $\overline{v_i v_j}, \overline{v_i v_k}, \overline{v_i v_s}$, which are either right-handed or left-handed.

In Figure 2.2, the two 0-faces of edge e_{ij} are v_i with a negative *induced orientation* and v_j with a positive *induced orientation*. The three incident edges to a triangle are 1-faces of the triangle, and the *induced orientation* is positive when

the edge's orientation coincides with the triangle's orientation. The *induced orientation* of a 2-face in a tetrahedron can be identified by whether the direction of the triangle's normal points inside or outside of the tetrahedron. Here the direction of the triangle's normal is decided by right/left hand rule if the tetrahedron has right/left-handed orientation.

When the two adjacent triangles both are clockwise or counter-clockwise, or two tetrahedra adjacent both have right-handed or left-handed orientation, the *relative orientation* is positive; otherwise, it is negative.

Definition 2.7. The **barycenter** of a p -simplex σ^p is the geometric center of all its points v_0, \dots, v_p , given by

$$bc(\sigma^p) = \frac{\sum_{i=0}^p v_i}{p+1}.$$

Here v_i represents the geometric location of the point. The p -**circumsphere** of σ^p is the unique p -sphere on whose surface $(p+1)$ vertices v_0, \dots, v_p all locate, and the center of this p -sphere is the **circumcenter** of σ^p , denoted $c(\sigma^p)$. Obviously, the distance between $c(\sigma^p)$ and v_i is equivalent for each $i = 0, \dots, p$. \diamond

The barycenter of a simplex is always inside the simplex, but this is not always true for circumcenter. So we define the following term to describe this property of circumcenter.

Definition 2.8. If the circumcenter of a simplex lies in its interior we call it **well-centered (WC) simplex**. If all the faces of a WC simplex are also WC, this WC simplex is a **completely well-centered (CWC) simplex**; otherwise, we call it weakly well-centered (WWC). A simplicial complex all of whose simplices (of all dimensions) are CWC is called **completely well-centered simplicial complex**. \diamond

In two dimensions, a triangle with all acute angles is an example of WWC 2-simplex, equivalent to CWC in two dimensions, thus a triangular mesh with only acute triangles is a CWC simplicial complex. In three dimensions, the requirements of CWC tetrahedron is much stricter; not only the tetrahedron but also all of its triangle faces should be (weakly) well-centered. The well-centered property plays an important role in constructing dual complex. Furthermore, it has an impact on stability and accuracy of the simulation, which we will further discuss in Chapter 3.

2.2.2 Dual Complex

The dual complex of a simplicial complex is also a discretization of the same space spanned by the primal simplicial complex, and is indispensable in DEC.

Here we only introduce the circumcentric dual complex used in our approach, but keep in mind there exists an alternative, that is, barycentric dual complex.

From a given CWC simplicial complex, we first generate another simplicial complex with smaller simplices, which shares the same underlying spaces as the original one, then combine some of the smaller simplices to give the dual complex as introduced in [Hirani (2003)].

Definition 2.9. The **circumcentric subdivision** of a CWC simplicial complex K of dimension n is denoted $\text{csd}K$, and it consists of **subdivision simplices**, which are simplices in the form $[c(\sigma_1), \dots, c(\sigma_p)]$ for $1 \leq p \leq n$ (note that the subscript is not dimension). Here $\sigma_i (i = 1, \dots, p)$ are in K , and $\sigma_1 < \sigma_2 < \dots < \sigma_p$, i.e., σ_i is a face of σ_j for all $i < j$. A subdivision simplex σ^q in a given simplex σ^p ($q \leq p$) is called a **subdivision q -simplex of σ^p** . \diamond

The fact that all circumcenters lie inside their simplices make $\text{csd}K$ satisfy the requirements of simplicial complex. The underlying space of K can be partitioned into dual cells, each of which is made by combination of certain simplices belonging to $\text{csd}K$.

Definition 2.10. Let σ^p be one simplex of a CWC primal mesh K of dimension n . The **circumcentric dual cell** of σ^p , $D(\sigma^p)$, is defined as

$$D(\sigma^p) = \bigcup_{r=0}^{n-p} \bigcup_{\sigma^p < \sigma_1 < \dots < \sigma_r} \text{Int}(c(\sigma^p)c(\sigma^1)\dots c(\sigma^r)).$$

For $r = 0$, $\sigma^p < \sigma_1 < \dots < \sigma_r$ is interpreted as σ^p . $\text{Int}(v_0\dots v_r)$ denotes the interior of the space spanned by the points $\{v_0, \dots, v_r\}$, without boundary. The closure of the dual cell with boundary is written as $\overline{D}(\sigma^p)$, and called the **closed dual cell**. Each $(n-p)$ -simplex $c(\sigma^p)c(\sigma^{p+1})\dots c(\sigma^n)$ is called an **elementary dual simplex** of σ^p . The collection of all dual cells is a cell complex, named **dual cell complex** $D(K)$. \diamond

Consider a two-dimensional primal mesh K as an example. K has vertex, edge and triangle subsets, which are $V = \{v_i\}$, $E = \{e_{ij}\}$, and $F = \{f_{ijk}\}$ respectively. Let L be the *circumcentric subdivision* of K , consisting of three p -simplex subsets, $L^{(p)}$, $p = 0, 1, 2$ (Figure 2.3):

- $L^{(0)}$ consists of circumcenter of each vertex, $c(v_i) = v_i$; midpoint of each edge, $c(e_{ij}) = c_{ij}$; and circumcenter of each triangle, $c(f_{ijk}) = c_{ijk}$ (c_{ijk} refers to the circumcenter of $v_i v_j v_k$).
- $L^{(1)}$ consists of two halves of each edge e_{ij} , $v_i c_{ij}$ and $v_j c_{ij}$; edges that connect the circumcenter of each triangle c_{ijk} to the vertices v_i, v_j, v_k , and to the midpoints of the edges c_{ij}, c_{jk}, c_{ki} .

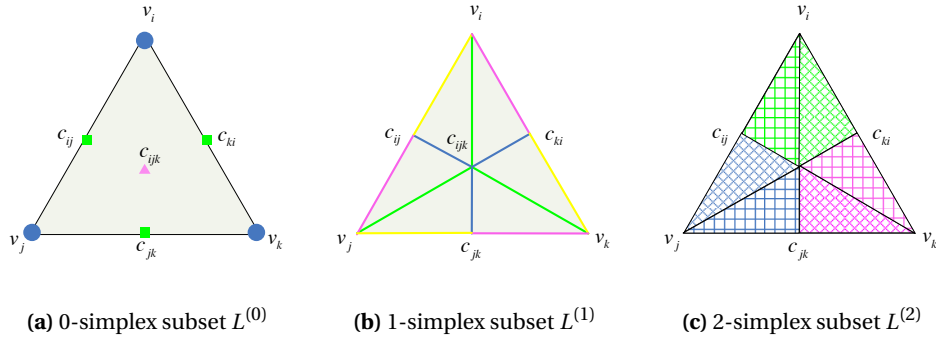


Figure 2.3: The circumcentric subdivision of a triangle, $L = \text{csd}K$, consists of (a) 0-simplex subset $L^{(0)}$, (b) 1-simplex subset $L^{(1)}$, and (c) 2-simplex subset $L^{(2)}$.

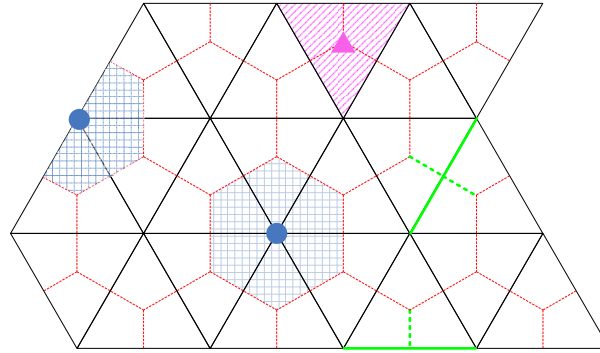


Figure 2.4: Primal and dual meshes in two dimensions. The primal mesh is a triangular mesh displayed in black lines, while the dual mesh is a cell complex in red dotted lines. Primal and dual elements marked in the same color explain their duality.

- $L^{(2)}$ consists of triangles of the form $v_i c_{ij} c_{ijk}$, and there are six such subdivided triangles in a primal triangle.

When $n = 2$, by definition, the dual 0-cell of a triangle $\sigma^2 = f_{ijk}$ is

$$D(f_{ijk}) = \text{Int}(c(\sigma^2)) = c_{ijk},$$

which is simply the circumcenter of the primal triangle. The dual 1-cell of an edge $\sigma^1 = e_{ij}$ is

$$D(e_{ij}) = c_{ij} \bigcup_{e_{ij} < f_{ijk}} \text{Int}(c_{ij} c_{ijk}),$$

which is its midpoint plus combined with open edge(s) connecting the midpoint to the circumcenter(s) of incident triangle(s). Finally, the dual 2-cell of a vertex $\sigma^0 = v_i$ is

$$D(v_i) = v_i \bigcup_{v_i < e_{ij}} \text{Int}(v_i c_{ij}) \bigcup_{v_i < f_{ijk}} \text{Int}(v_i c_{ijk}) \bigcup_{v_i < e_{ij} < f_{ijk}} \text{Int}(v_i c_{ij} c_{ijk}),$$

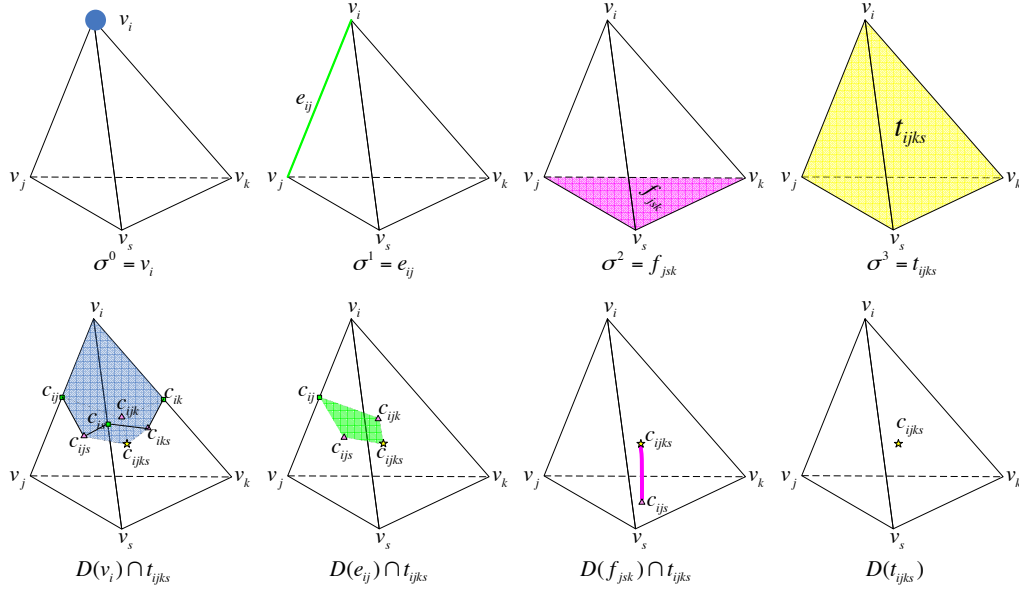


Figure 2.5: Primal and dual elements in three dimensions. The top row shows the primal mesh with a highlighted p -simplex, $p = 0, 1, 2, 3$, respectively; the bottom row shows the intersection of t_{ijks} and dual cells corresponding to the primal simplices on top.

where the first term is the primal vertex itself, and the second and third term is the all the open edges starting at v_i and going to the circumcenters of the primal edges and triangles incident on v_i , and the last term is the union of all the open subdivided 2-simplices containing v_i . Therefore, by combining these three terms, we get an open Voronoi cell around v_i . The dual cells of several p -simplices ($p = 0, 1, 2$) in a two-dimensional simplicial complex K are displayed in Figure 2.4. Similarly, we can construct the dual cells in three dimensions as depicted in Figure 2.5.

The dual cells described above are without orientation. Next we will discuss how to orient these dual cells. Let $\sigma^0 < \sigma^1 < \dots < \sigma^n$ be oriented simplices in an n -dimensional primal mesh K , and σ^p be one of these simplices ($1 \leq p \leq n - 1$). We have to give the elementary dual simplex $\tau^{(n-p)} = [c(\sigma^p) \dots c(\sigma^n)]$ an orientation s for each p , then we can decide the orientations of all $(n - p)$ - dual cells by using relative orientation. Note that the orientations of $\eta^p = [c(\sigma^0), \dots, c(\sigma^p)]$ and σ^p can be compared since they are on the same plane, and it is the same for τ^n and σ^n . Then we define

$$s(\tau^{(n-p)}) = \text{sgn}(\eta^p, \sigma^p) \times \text{sgn}(\tau^n, \sigma^n),$$

where sgn is the relative orientation. For $p = n$, the dual is of dimension 0, so that has no orientation. For $p = 0$, we define $s(\tau^n) = \text{sgn}(\tau^n, \sigma^n)$.

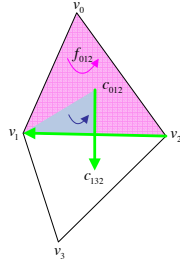


Figure 2.6: Example of orienting a dual cell in two dimensions.

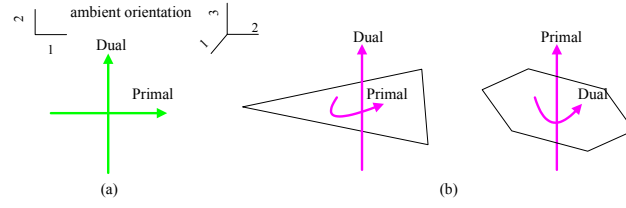


Figure 2.7: Induced orientation of dual cells in (a) two dimensions and (b) three dimensions.

Let's start with a relatively simple example to understand the algorithm of orienting dual cell. When $n = 2$, $p = 1$ (Figure 2.6), we have:

$$\text{primal 1-simplex: } \sigma^1 = [v_2 v_1];$$

$$\sigma^0 < \sigma^1 < \sigma^2: \text{ for instance, } v_1 < [v_2 v_1] < [v_0 v_1 v_2];$$

$$\text{elementary dual simplex: } \tau^1 = [c(\sigma^1) c(\sigma^2)] = [c_{12} c_{012}];$$

$$\text{subdivision simplex: } \eta^1 = [c(\sigma^0) c(\sigma^1)] = [v_1 c_{12}].$$

$$\begin{aligned} s(\tau^1) &= \text{sgn}(\eta^1, \sigma^1) \times \text{sgn}(\tau^2, \sigma^2) \\ &= \text{sgn}([v_1 c_{12}], [v_2 v_1]) \times \text{sgn}([v_1 c_{12} c_{012}], [v_0 v_1 v_2]) \\ &= (-1)(+1) = -1, \end{aligned}$$

which means $D(\sigma^1)$ should be oriented in the opposite orientation of $[c_{12} c_{012}]$, so $D(\sigma^1) = [c_{012} c_{132}]$.

Note that $\eta^1 = [v_1 c_{12}]$ and $\sigma^1 = [v_2 v_1]$ are on the same plane (here the line containing both), similarly for $\tau^2 = [v_1 c_{12} c_{012}]$ and $\sigma^2 = [v_0 v_1 v_2]$. We have another direct way to see this algorithm for the case in n dimensions ($n = 2, 3$). We orient all dual n -cells in the same orientation as all primal n -simplices, counter-clockwise ($n = 2$) or right-handed orientation ($n = 3$), and the ambient orientation obeys right hand rule. Once the orientation of the primal p -simplex is given, then positive induced orientation of its corresponding dual $(n - p)$ -cell can be decided by right hand rule, as shown in Figure 2.7. In the following text, if σ^p is an oriented primal p -simplex, $\star\sigma^p$ means its dual $(n - p)$ -cell with the positive induced orientation from σ^p , and its $(n - p)$ -volume is denoted $|\star\sigma^p|$.

2.2.3 Discretization of the Space

This section discusses how we discretize the space, and involves choosing a primal mesh K and its corresponding dual mesh $D(K)$ to describe the space, comparing barycentric and circumcentric dualities, and generating the meshes by Delaunay triangulation scheme.

The reason why we prefer simplicial complex to regular grid is that regular grid always lose more details in describing irregular boundaries, as it is the case in most medical applications. In order to fix the boundary problem of regular grid, octree method has been applied to generate smaller elements near the boundary. However, it raises other difficulties in the simulation caused by T-junctions at the interface of two elements in different sizes. Firstly, it always requires supplemental process to consider the interaction between elements at T-junctions. Secondly, the line connecting the centers of two neighbor elements at a T-junction, loses the orthogonality to the interface. The advantages of orthogonal property are presented in the next paragraph. By definition (Definition 2.2), simplicial complexes avoid T-junctions. Besides, the introduction of orientation is also useful when defining variables. In DEC, variables are scalars attached to simplices of different dimensions. Although we use scalar, vector can be represented by the scalar plus the geometrical position and orientation of the associated simplex. On the other hand, the use of a dual mesh is very common in many computational fields and in physics to define operators and describe theories. There are lots of properties of symmetry and duality between the primal and the dual. Such as, in n dimensions, a dual $(n - p)$ -cell is associated to a corresponding p -simplex. As a result, the total number of dual $(n - p)$ -cell is equal to that of primal p -simplex.

We have defined two different centers of a primal simplex (Definition 2.7), leading to two types of dual meshes, barycentric or circumcentric dual. Both types have their own advantages and disadvantages. Barycentric dual has a very appealing property that barycentric subdivision (similar to circumcentric subdivision in Definition 2.9), always produces a simplicial complex, since barycenter always lies inside its simplex, which guarantees the convexity of dual simplices. But this is not the case in circumcentric subdivision, and that is why well-centered primal mesh is required in the definition of circumcentric subdivision; otherwise, the dual cell may not be convex and consequently $\text{csd}K$ may not be a simplicial complex. Moreover, if the mesh is deformed during the simulation, barycentric dual will still remain well-defined, while circumcentric dual may soon become invalid if some circumcenters escape from the interior of their simplices. Once the dual is invalid, remeshing is usually applied to solve this problem, certainly causing extra computational cost. In spite of such restrictions, circumcentric dual provides convenience in building some operators of the DEC theory, such as Hodge star. Furthermore, a primal 1-simplex is perpendicular to its dual $(n - 1)$ -cell, similarly, a dual 1-cell is perpendicular to its primal $(n - 1)$ -simplex. This orthogonality offers simpler expressions for some variables and theories. Take fluid dynamics for example, the line through neighboring pressure locations (circumcenters) is perpendicular to the shared face of their tetrahedra, and thus parallel to the flux stored at the face.

Nevertheless, the construction of a well-centered primal mesh is computationally challenging, especially in high dimensions. Delaunay triangulation in n dimensions only produces a simplicial complex in which no 0-simplex lies inside the circumsphere of any n -simplex, and guarantees non-self-intersection of the circumcentric dual mesh. The well-centered requirement is much stronger and more difficult to satisfy when dimension $n \geq 3$. Some efforts have been made in this direction, see [Vanderzee et al. (2008)] as an example. In this chapter we temporarily ignore all these computational difficulties and assume that we are given a primal mesh satisfying the required conditions. We will proceed to build exterior calculus objects and operators on such a mesh. The effort we made to get a mesh as qualified as possible and the influence of non well-centered mesh on simulation will be discussed in Chapter 3.

2.3 Discrete Forms

In the theory of the continuous domain, a differential form is informally explained as an integrand, and p -form can be integrated on a p -manifold. In other words, it is a linear mapping from a p -manifold to \mathbb{R} . In the discrete theory, the counterpart of p -manifold is p -chain, roughly speaking a linear sum of all p -simplices. As a result, the discrete p -form should be a linear mapping from a p -chain to \mathbb{R} , which is an evaluation operation on the p -chain. In this section, we give the informal but intuitive definitions of primal chains and primal cochains (i.e., discrete primal forms). Dual chains and dual cochains are similar.

Definition 2.11. K is a primal mesh, and we define $C_p(K; \mathbb{Z})$ to be the group generated by a basis consisting of all the oriented p -simplices in K . Elements of $C_p(K; \mathbb{Z})$ are called **primal p -chains**, denoted $c_p \in C_p(K; \mathbb{Z})$, and we have

$$c_p = \sum_{\sigma^p \in K} c(\sigma^p) \cdot \sigma^p,$$

where $c(\sigma^p) \in \mathbb{Z}$. ◇

Actually, p -chain can be seen as a series of integers, and each value corresponds to a p -simplex. We define the notation K^p as the subset consisting of all primal p -simplices in K . Then c_p can be simply thought as a column vector with the size of $|K^p|$: $c_p = [c(\sigma_0^p), \dots, c(\sigma_{|K^p|-1}^p)]^T$.

Definition 2.12. A **primal p -cochain** α^p is a homomorphism from the chain group $C_p(K; \mathbb{Z})$ to \mathbb{R} , which can be explained as a linear mapping from a primal p -chain c_p to a real number, $\alpha^p(c_p)$. The space of primal p -cochains denotes $C^p(K; \mathbb{R})$. Actually, p -cochain operating on a p -chain and resulting in a scalar, is the discrete analogue to differential p -form, that is, a **discrete primal p -form**. ◇

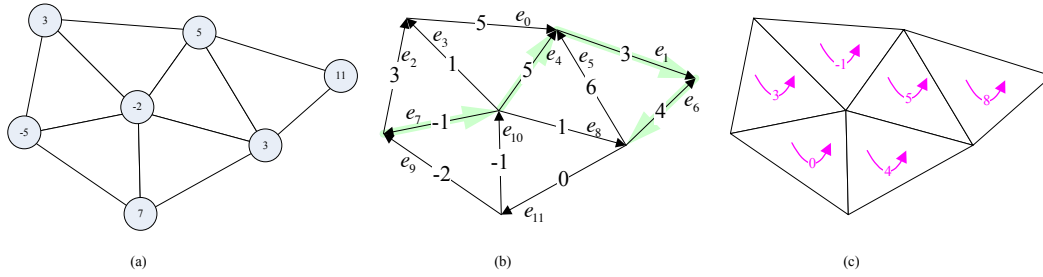


Figure 2.8: Examples of discrete primal forms: (a) 0-form, (b) 1-form, and (c) 2-form. The value marked on p -simplex σ^p is the discrete p -form $\alpha^p(\sigma^p)$, a real number associated to each p -simplex. Consider an example of 1-chain, the green curve in (b), $c_1 = -e_7 + e_4 + e_1 - e_6$, then we have $\alpha^1(c_1) = -(-1) + 5 + 3 - 4 = 5$.

All the p -simplices form a basis for vector space $C_p(K; \mathbb{Z})$, and mappings of the basis is sufficient to determine a linear mapping. So α^p can be represented as a column vector, $\alpha^p = [\alpha^p(\sigma_0^p), \dots, \alpha^p(\sigma_{|K^p|-1}^p)]^T$. Thus $\alpha^p(c_p)$ becomes simply the vector multiplication of $(\alpha^p)^T c_p$. Examples of a discrete p -form ($p = 0, 1, 2$ in two dimensions) are given in Figure 2.8. In this example, each triangle of the mesh is counter-clockwise oriented, and each edge has its own independent orientation represented by the arrows. The primal p -form can be simply considered as a set of values, each of which corresponds to a p -simplex, so the p -form is able to be evaluated at any point ($p = 0$), or on any curve ($p = 1$), or on any surface ($p = 2$) by summing the values of these elements with the sign ± 1 .

Similarly, **dual chains** are linear combination of dual cells, and **dual cochains** (**dual forms**) are defined in the same way. Either primal or dual p -form can be considered as integrals of a physical quantity over all primal p -simplices or dual p -cells.

2.4 Operators

There are two basic types of operators, Hodge stars \star and discrete exterior derivatives d , from which we build discrete codifferential operator δ . Hodge stars make the transitions between primal and dual forms, while the transitions through the other two operators, d and δ , remain in the same set of either primal or dual forms. Furthermore, in the next chapter, we will see that all the vector calculus operators involved in our application can be derived from \star and d .

2.4.1 Hodge Star

Hodge star \star_p maps a p -form to a $(n-p)$ -form, and the subscript which specifies its dimension can be ignored since it is context-dependent. (Many operators defined afterward have the same property, so the subscript is sometimes ignored.)

The discrete counterpart is easier to construct if we choose the diagonal Hodge stars, as we only need to define transition from a primal p -form α^p to a dual $(n-p)$ -form $\star\alpha^p$, satisfying the equality of averages between the two:

$$\frac{1}{|\sigma^p|} \int_{\sigma^p} \alpha^p = \frac{1}{|\star\sigma^p|} \int_{\star\sigma^p} \star\alpha^p.$$

A diagonal matrix of dimension $|K^p| \times |K^p|$ can be used to describe \star_p , and the i^{th} diagonal element is:

$$\star_p[i][i] = \frac{|\star\sigma_i^p|}{|\sigma_i^p|}.$$

Vice-versa, the transition from dual $(n-p)$ -forms to primal p -forms $\star_{dual(n-p)}$ can be represented as

$$\star_{dual(n-p)} = \star_{primal(p)}^{-1}.$$

In the following text, the notation \star always means the primal one, since the dual one can be expressed simply by the inverse.

Based on hodge operators, we can define the inner product of p -forms α and β as follow:

$$(\alpha, \beta) = \alpha^T \star \beta.$$

2.4.2 Discrete Exterior Derivative

We first define boundary operator on chains and coboundary operator on cochains. Then we will show that discrete exterior derivative is exactly the definition of coboundary operator, which is the conclusion of the Stokes' theorem. Finally, we introduce discrete codifferential operators.

Definition 2.13. The **boundary operator** ∂_p is a linear mapping from p -chain $\in C_p(K; \mathbb{Z})$ to $(p-1)$ -chain $\in C_{p-1}(K; \mathbb{Z})$. The mapping on the basis of $C_p(K; \mathbb{Z})$, $\{\sigma^p\}$ is defined as:

$$\partial\sigma^p = \partial([v_0 \dots v_p]) = \sum_{i=0}^p (-1)^i [v_0 \dots \hat{v}_i \dots v_p].$$

Note that $\partial_p \circ \partial_{p+1} = 0$. ◇

In other words, the boundary of a p -simplex is the combination of all the $(p-1)$ faces with positive induce orientation.

Definition 2.14. The **natural pairing** of a p -form α^p and a p -chain c_p is defined as

$$\langle \alpha^p, c_p \rangle = \alpha^p(c_p).$$

◇

Definition 2.15. The **coboundary operator** θ_p is a linear mapping from p -cochain $\in C^p(K; \mathbb{R})$ to $(p+1)$ -cochain $\in C^{p+1}(K; \mathbb{R})$, defined by duality to ∂_{p+1} through natural pairing. Specifically, for a p -cochain $\alpha^p \in C^p(K; \mathbb{R})$ and a $(p+1)$ -chain $c_{p+1} \in C_{p+1}(K; \mathbb{Z})$, the coboundary operator is:

$$\langle \theta \alpha^p, c_{p+1} \rangle = \langle \alpha^p, \partial c_{p+1} \rangle,$$

that is,

$$\theta_p \alpha^p = \alpha^p \circ \partial_{p+1}.$$

Note that $\theta_{p+1} \circ \theta_p = 0$. ◇

We can use the Stokes' theorem to prove that the discrete exterior derivative is exactly the coboundary operator. Written in terms of form, the Stokes' theorem states that the integral of a $(p+1)$ -form over a $(p+1)$ -chain can be evaluated the integral on the boundary of the $(p+1)$ -chain:

$$\int_{c_{p+1}} d\alpha^p = \int_{\partial c_{p+1}} \alpha^p,$$

if written in terms of natural paring:

$$\langle d\alpha^p, c_{p+1} \rangle = \langle \alpha^p, \partial c_{p+1} \rangle. \quad (2.3)$$

By comparing Equation 2.3 to the Definition 2.15, we know the **discrete exterior derivative** d_p equals to the coboundary operator θ_p .

To represent ∂_p we use a matrix of dimension $|K^{p-1}| \times |K^p|$, which is sparse and contains only the non-zero values of ± 1 . Similarly, d_p is represented by a matrix of dimension $|K^{p+1}| \times |K^p|$, $d_p = (\partial_{p+1})^T$, which describes the incident relationship between $(p+1)$ -simplices and p -simplices. Since the dual complex inherits the incident property from the primal complex, we can easily derive the discrete exterior derivatives on the dual mesh as the transpose of primal ones, represented as:

$$d_{dual(n-p)} = d_{primal(p)}^T.$$

So the notation d only refers to the primal discrete exterior derivative in the following text, and the dual one is represented by the transpose.

Based on \star and d operators, we can now create an **adjoint** operator δ of d , called discrete codifferential operator, to map a $(p-1)$ -form to a p -form. Here adjoint means that

$$(d\alpha^{p-1}, \beta) = (\alpha, \delta\beta^p).$$

So we have

$$\delta_p = (\star_{p-1})^{-1} d_{p-1}^T \star_p.$$

The transitions between forms in three-dimensional space are illustrated in Figure 2.9.

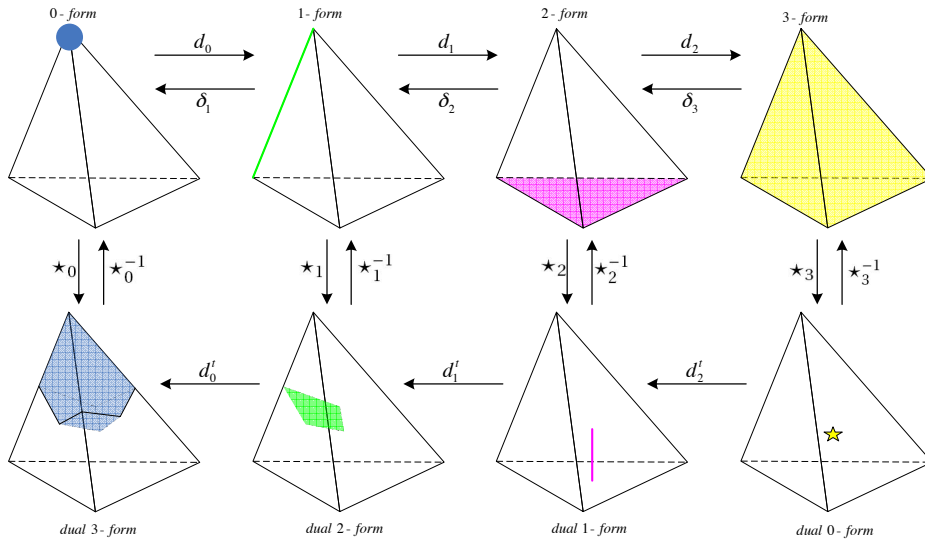


Figure 2.9: Transition between forms through Hodge stars \star and exterior derivatives d in three dimensions.

Till now, we have developed the discretized space (primal and dual mesh), variables (discrete forms), and fundamental operators (hodge stars and discrete exterior derivatives). From now on, we will work within the discrete objects, and the terms mentioned below are of discrete version by default.

2.5 Implementation

Although the mathematical definitions and algorithms seem complicated and confusing, implementation of the objects in DEC is simple and straightforward. First of all, we need to construct an appropriate data structure for primal mesh, and derive its corresponding dual mesh. Then with the column vector representation of discrete forms, the two basic operators are described as matrices computed from topological and geometrical information of these meshes, respectively.

2.5.1 Representation of Meshes

Most publicly available mesh formats only support unoriented elements and limited incident information between elements (e.g., only triangle/tetrahedron-vertex incidence). However, in order to represent an oriented manifold-like simplicial complex, we require a data structure supporting orientation, local traversal of elements and incident information for simplices of all dimensions.

We load the two-dimensional (three-dimensional) mesh in a common format with a list of positions of all vertices and a list of triangles (tetrahedra), each

of which is represented by a set of the indices of its vertices. First of all, we use a list V to store positions of all vertices, and this list provides a unique index for each vertex. Then a p -simplex ($p \geq 1$) is represented by a $(p+1)$ -tuple composed by indices of all vertices that bound the simplex. All the permutations of a given tuple represent the same simplex. For example, (i, j) and (j, i) are just different expressions of the same edge. We create other lists E, F (and T) to store only a representative of different expressions for each edge, each triangle (and each tetrahedron), respectively. Although different permutations of a tuple give the same simplex, but perhaps oriented oppositely. From Definition 2.3, we know that the permutations in the same equivalent class represent the same oriented simplex, while permutations in different equivalent classes give two converse orientations. For example, $(i, j, k) = (j, k, i) = (k, i, j) = -(j, i, k) = -(i, k, j) = -(k, j, i)$. Each tuple stored in E, F (and T) defines an intrinsic orientation for each simplex by the order of vertex indices.

The combination of these lists V, E, F (and T) is a representation of n -dimensional ($n = 2$ or 3) simplicial complex. We orient all the n -simplices in the same orientation, counter-clockwise (or right-handed). This is done before storing an n -simplex in the list. Given any expression of the same n -simplex, (i_0, \dots, i_n) , we first compute its volume as

$$\begin{aligned} n = 2: \quad \text{Vol}(i_0, i_1, i_2) &= \frac{1}{2} \overrightarrow{v_{i_0} v_{i_1}} \times \overrightarrow{v_{i_0} v_{i_2}}; \\ n = 3: \quad \text{Vol}(i_0, i_1, i_2, i_3) &= \frac{1}{6} (\overrightarrow{v_{i_0} v_{i_1}} \times \overrightarrow{v_{i_0} v_{i_2}}) \cdot \overrightarrow{v_{i_0} v_{i_3}}. \end{aligned}$$

If it is positive, then we keep this orientation and store (i_0, \dots, i_n) in the list; otherwise, we reverse the orientation by swapping i_0 and i_1 in the $(n+1)$ -tuple, then $(i_1, i_0, i_2, \dots, i_n)$ is stored in the list. For p -simplex ($1 \leq p \leq n-1$), the intrinsic orientation is chosen arbitrarily.

Dual mesh is more like a concept in the computation, consequently we seldom actually create a data structure to store it. Once we need information of dual meshes, we can easily generate from primal meshes. In the following subsection, implementation of operators is introduced, and we will also see how to construct dual mesh when computing Hodge star operators.

2.5.2 Discrete Forms and Operators

A discrete form, either primal or dual, is simply represented as a column vector stored in arrays of dimension of $|V|, |E|, |F|$ or $|T|$ ($|\cdot|$ means the length of the list). The i^{th} value in the array relates to the i^{th} primal simplex or its dual cell. We also use the notation of K^p , where $p = 0, 1, 2, 3$, corresponding to V, E, F and T , respectively.

We first construct d operators of all dimensions, which is the transpose of boundary operators, involving only topological information of the primal mesh,

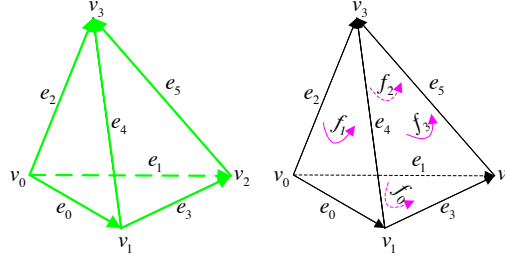


Figure 2.10: Example of a single tetrahedron. Edges and faces have their intrinsic orientations as displayed by arrows.

see Algorithm 2.1. Using similar algorithms, we can also construct other incident information of the mesh, such as edge-tetrahedron stored in the list ET , the i^{th} element of which contains indices of all tetrahedra incident on the i^{th} edge in E .

Algorithm 2.1 Implementation of d_p operator

```

set  $d_p = \mathbf{0}$ 
for  $j = 0 : |K^p| - 1$  do
  get the  $j^{th}$   $p$ -simplex in  $K^p$ ,  $(i_0, \dots, i_p)$ 
  for  $k = 0 : p$  do
    determine the index  $m$  of the representative of  $(i_0, \dots, \hat{i}_k, \dots, i_p)$  in  $K^{p-1}$ 
    if  $K^{p-1}[m] = -(i_0, \dots, \hat{i}_k, \dots, i_p)$  then
      sign  $\leftarrow (-1)^{(k+1)}$ 
    else
      sign  $\leftarrow (-1)^k$ 
    end if
     $d_p[j][m] \leftarrow$  sign
  end for
end for

```

As an example, simplex lists and d operators are illustrated in a simple case of a single tetrahedron, shown in Figure 2.10. Three coordinates (x, y, z) of v_i ($0 \leq i < 4$) is stored at $V[i]$, and E, F, T are constructed as follows:

$$\begin{aligned}
 E &= \{e_0 = (0, 1), e_1 = (0, 2), e_2 = (0, 3), e_3 = (1, 2), e_4 = (1, 3), e_5 = (2, 3)\}, \\
 F &= \{f_0 = (0, 1, 2), f_1 = (0, 1, 3), f_2 = (0, 2, 3), f_3 = (1, 2, 3)\}, \\
 T &= \{t_0 = (0, 1, 2, 3)\}.
 \end{aligned}$$

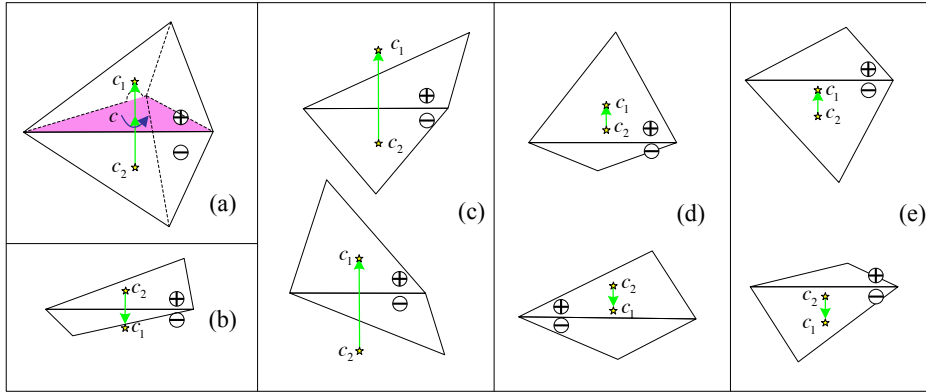


Figure 2.11: Different possibilities of dual edges in non well-centered meshes. (a) Both t_1 and t_2 are WWC, the dual edge and its volume falls into the identical description as in Algorithm 2.2. (b) Both t_1 and t_2 locate the opposite side of f to their own circumcenters, leading to the negative dual volume $-||c_2c|| - ||cc_1||$. (c) Though being non-well centered, either t_1 or t_2 is at the same side of f as its own circumcenter, which makes no difference with (a). (d)(e) Either c_2 or c_1 leaves its tetrahedron beyond f plane, and the dual volume is $\mp||c_2c|| \pm ||cc_1||$.

Then the three d operators can be described by matrices as follows:

$$d_0 = \begin{pmatrix} -1 & 1 & & & & \\ -1 & & 1 & & & \\ -1 & & & 1 & & \\ & -1 & & & 1 & \\ & -1 & & & & 1 \\ & & -1 & & & & 1 \end{pmatrix} \quad d_1 = \begin{pmatrix} 1 & -1 & & 1 & & & \\ 1 & & -1 & & 1 & & \\ & 1 & -1 & & & 1 & \\ & & & 1 & -1 & & 1 \end{pmatrix}$$

$$d_2 = (1 \quad -1 \quad 1 \quad -1).$$

With incident information plus geometry of the mesh, we fill the diagonal of Hodge star matrix by volume ratio of corresponding dual cell and primal simplex. The computation of dual volume takes advantage of the orthogonality of circumcentric dual, see Algorithm 2.2, which also gives an implementation of constructing the dual mesh from the primal mesh.

Note that we have assumed the primal mesh to be CWC to develop all the objects above. However, when the primal mesh is non well-centered, the implementation only differs in handling dual edge. All the possibilities of a dual edge are displayed in Figure 2.11. Consider the dual edge of triangle f that is incident on two tetrahedra, t_1 (at the upper side of f) and t_2 (at the bottom side of f), and denote circumcenters as $c = c(f)$, $c_1 = c(t_1)$ and $c_2 = c(t_2)$. The intrinsic orientation of f is shown in Figure 2.11(a), thus the induced orientations of f are $\text{sgn}(f, t_1) = +1$, $\text{sgn}(f, t_2) = -1$. To be clear and simple, the projection on a plane is shown in other sub-figures. The dual edge is uniformly defined as $\overrightarrow{c_2c} + \overrightarrow{cc_1} = \overrightarrow{c_2c_1}$ (remember that the three circumcenters are collinear), and its volume is calculated by $(-1)^{k_2}||c - c_2|| + (-1)^{k_1}||c_1 - c||$, where k_1 (k_2) is odd

Algorithm 2.2 Construction of the dual mesh

```

set all dual volumes to be zero
set all dual cells to be empty sets

//Dual vertices
for each primal tetrahedron  $t$  do
  compute  $c(t)$  //circumcenter of  $t$ 
   $t.dualVolume \leftarrow 1$ 
   $t.dual \leftarrow sp(c(t))$  //space spanned by  $c(t)$ 
end for

//Dual edges
for each primal triangle  $f$  do
  compute  $c(f)$ 
  for each primal tetrahedron  $t_f$  incident on  $f$  do
     $b \leftarrow t_f.dualVolume$ 
     $h \leftarrow \|c(f) - c(t_f)\|$  //the distance between  $c(f)$  and  $c(t_f)$ 
     $f.dualVolume \leftarrow f.dualVolume + bh$ 
     $f.dual \leftarrow f.dual \cup sp(c(f), sp(c(t_f)))$ 
  end for
end for

//Dual faces
for each primal edge  $e$  do
  compute  $c(e)$ 
  for each primal triangle  $f_e$  incident on  $e$  do
     $b \leftarrow f_e.dualVolume$ 
     $h \leftarrow \|c(e) - c(f_e)\|$ 
     $e.dualVolume \leftarrow e.dualVolume + \frac{1}{2}bh$ 
     $e.dual \leftarrow e.dual \cup sp(c(e), sp(c(f_e)))$ 
  end for
end for

//Dual 3-cells
for each primal vertex  $v$  do
   $c(v) = v$ 
  for each primal edge  $e_v$  incident on  $v$  do
     $b \leftarrow e_v.dualVolume$ 
     $h \leftarrow \|c(v) - c(e_v)\|$ 
     $v.dualVolume \leftarrow v.dualVolume + \frac{1}{3}bh$ 
     $v.dual \leftarrow v.dual \cup sp(c(v), sp(c(e_v)))$ 
  end for
end for

```

when c_1 (c_2) and t_1 (t_2) is at different sides of the plane spanned by f ; otherwise, it is even. If f only belongs to one tetrahedron, the items corresponding to the other tetrahedron is omitted in the formulation. The dual volume is negative, if the dual edge is not in the positive induced orientation from f (from bottom to top in this case). As a consequence, some elements of Hodge stars may be negative in a non well-centered primal mesh, and the negative sign can be seen as a correction of orientation for transition between primal and dual forms.

BLOOD FLOW SIMULATION

In the beginning of this chapter, we provide a selective review of recent studies concerning blood flow simulation in vascular system (Section 3.1). Then we present our method for fast simulating. Firstly, we describe the process of generating the geometry model of aneurysm and adjacent vessels from patient-specific data. The completely well-centered meshing techniques are also discussed (Section 3.2). Secondly, we describe the DEC approach for blood flow simulation in and around aneurysm by solving the vorticity-based Navier-Stokes equations (Section 3.3). Thirdly, advanced topics on acceleration of the simulation are presented (Section 3.4). Finally, through a series of experiments, we demonstrate the stability, accuracy and computational efficiency of the DEC method compared to a widely used commercial software (Section 3.5), and discuss the limitation of the DEC method on mesh quality and the approaches to further improvement of mesh quality and computational time (Section 3.6).

3.1 Physiological Fluid Dynamics

It is difficult to quantify physiological status by in vivo techniques. As a consequence, computational models based on CFD methodologies play an important role in many physiological phenomena throughout the human body, including the cardiovascular system (e.g., global or local pulsatile blood flow [Paul et al. (2009)], wave propagation [Ning et al. (2010)], the dynamics of natural and artificial heart valves [Weinberg et al. (2010)]), the respiratory system (e.g., phonation [Larsson and Müller (2011)], the closure and reopening of airways [Wall and Rabczuk (2008)]), and elsewhere in the body (e.g., transport driven by blood flow or fluid-muscle interaction [Rappitsch and Perktold (1996)]). Especially when combined with medical imaging techniques, the possibility of constructing anatomical geometry models provides a new insight to airflow and blood flow velocity and pressure fields in each individual patient.

3.1.1 Geometry Model

Generally speaking, the mesh quality is essential to numerically solving the governing equations. Firstly, the surface mesh should be smooth; otherwise, the boundary irregularities cause significant numerical problems, resulting in poor convergence and non-smooth solution. Secondly, the quality and topology of the volumetric mesh, which is the discretization of continuum domain, has an important impact on stability and computational efficiency of the simulation. One critical property is the mesh resolution and how the resolution distributes throughout the mesh. Mesh resolution directly relates to two issues in the simulation: one is the total number of elements in the mesh, which plays a decisive role in computational cost; the other is the size of each element, which limits the size of time step because of the requirement of convergence (for example, when solving hyperbolic partial differential equations, the Courant-Friedrichs-Lewy condition is a necessary condition). Other quality measurements involve geometrical regularity of the mesh elements; the extremely irregularity, such as short edges, sharp angles, and flat cells, should be avoided.

Nowadays, it is possible to reconstruct three-dimensional geometrical representations from computed tomography (CT), magnetic resonance imaging (MRI), or ultrasonography. However, noises and resolution of the image slices are two main limitations in medical imaging and image processing techniques. Thus reconstruction of accurate and smooth geometry is still difficult, particularly for the complex and small anatomical structures, which is the usual case for cerebral aneurysm. Generally, there are two main approaches to reconstruction of a patient-specific model. The first one is to segment the image, to identify the aneurysm and surrounding vessels, then to generate and optimize the surface mesh. Each step is non-trivial, and user interaction to some degree is often required. So recent improvements aimed at minimizing manual intervention [Auer and Gasser (2010)] [Shum et al. (2011)]. The other approach is to deform the model already based on a mesh to fit the subject of interest. Barber et al. started from an idealized template mesh, produced the patient-specific mesh by using volumetric registration of pseudo-image [Barber et al. (2007)]. An advantage of this method was that segmentation was achieved automatically as part of the image registration process.

Figure 3.1 presents our process of generating patient-specific mesh. We start from a volumetric medical dataset where the brain vessels are visible (such as three-dimensional rotational angiography), which is then segmented. From the segmented image, we reconstruct a surface model. In our case, we rely on a combination of several techniques, such as the Marching Cubes algorithm followed by small deformation of the resulting mesh, i.e., relaxation, to smooth the surface while adjusting the surface point location using the original image

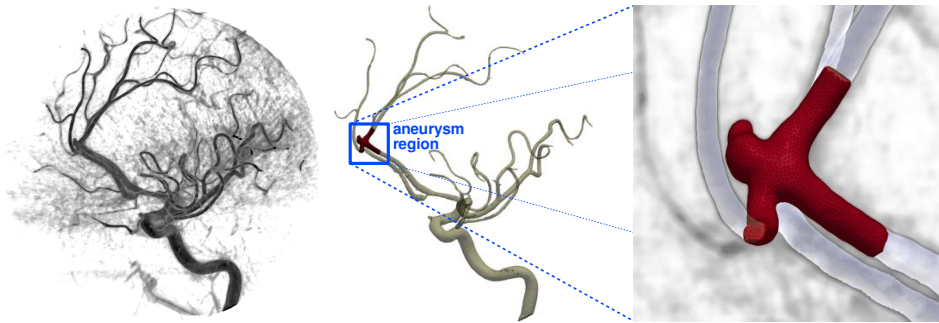


Figure 3.1: Mesh generation from patient-specific data. (Left) patient-specific data; (middle) reconstructed vessel surface model; (right) tetrahedral mesh generated in the region of the aneurysm.

data and its gradient. As we are only interested in creating a mesh for the region near aneurysm, but not for the whole vascular network, sometimes only an iso-surface from the measured raw density is sufficient to obtain the surface mesh. Yet it highly depends on the quality of data; in some instances, more robust algorithms are required, see [Hernandez and Frangi (2007)] for example. Finally, planes or spheres are manually positioned to cut the vessels and define inlet(s) and outlet(s).

The meshes generated by the approaches illustrated above are surface models. But volume meshes are required by numerical simulation. Structured meshes are easy to obtain for some simple geometries [Long et al. (1998a)]. While unstructured meshes are more popular for anatomical structures in complex shape. Arbitrary distributions of tetrahedral, hexahedral or prismatic elements can be generated by using a variety of sophisticated algorithms [Thompson et al. (1999)]. Typically, tetrahedral mesh is produced through Delaunay triangulation with diverse refinement and optimization schemes (e.g., [Si (2008)]).

3.1.2 Hemodynamic Simulation

Hemodynamics was studied in numerous experimental models and clinical studies to investigate the relationship between hemodynamics and cardiovascular diseases [Gonzalez et al. (1992)]. However, these methodologies were restricted to idealized aneurysm geometries or surgically created anatomical structures in animals, with a limited practical value in studying clinical events. In vitro studies using idealized geometries allowed detailed measurement of hemodynamics [Liou and Liou (1999)], but had little direct use to understand hemodynamic information in a patient-specific clinical case.

In recent decades, CFD becomes an attractive tool because of its ability of simulating on all possible geometries. Most CFD modeling approaches approximated blood flow as a continuous incompressible Newtonian fluid, described

by a corresponding mathematical model, that is, the unsteady incompressible Navier-Stokes equations [Mazumdar (1992)]. A majority of these studies assumed the blood to be a Newtonian fluid with constant viscosity, but this hypothesis might not be justified under certain situations [Fisher and Rossmann (2009)]. Wang and Bernsdorf used a Lattice Boltzmann solver with a Carreau-Yasuda model to capture non-Newtonian rheology of blood flow in cerebral aneurysms, which was much more complicated [Wang and Bernsdorf (2009)].

Until the late 1990s, a successful effort in the researches of combining image processing and CFD made it possible to compute patient-specific hemodynamic information in this community [Long et al. (1998b)] [Milner et al. (1998)] [Antiga et al. (2008)].

The spread of CFD method is motivated not only by the improvements in the computing ability of personal computers and parallel clusters, but also by the increasing need in clinical applications. Qiao and Liu reviewed several medical application related to blood flow simulations, such as hemodynamic simulation of bypass graft for stenosed arteries, stented aneurysm at the aortic arch and so on [Qiao and Liu (2008)]. Groden et al. constructed a simple geometrical model by only straight cylinders and spheres to approximate an actual aneurysm, and simulated the flow by solving the Navier-Stokes equations [Groden et al. (2001)]. The geometry model they used could not accurately describe the real patient's case, therefore, had little use in surgery planning for a specific case. Kakalis et al. employed patient-specific data to get more realistic flow patterns [Kakalis et al. (2008)]. However, both of their methods, as well as most similar studies, relied on the CFD commercial software to simulate the flow, and the computational times (dozens of hours in general) were incompatible with interactive simulation or even clinical practice. In order to reach fast computation, several template-based methods were designed [McGregor et al. (2009)] [McLeod et al. (2010)]. These methods pre-computed hemodynamics on a set of similar template geometries, and then interpolated on a patient-specific geometry instead of fluid simulation. However, they required to set up a pre-computed database, and were only tested on simple artery structures. But for the brain vessels around intracranial aneurysm, the network and shape are much more complicated, so the high accuracy cannot be expected.

The CFD can be a powerful tool for the computer-assisted intervention in the future, but before it being widely used, the obstacles are multifold. Two of these obstacles are accuracy of the computed results and efficiency of the computing process, which are two significant pursuits in numerical calculation, but unfortunately often contradictory. Lots of computationally efficient techniques were developed in the field of computer graphics, which essentially required the results to be visually convincing, but not physically accurate. The stable fluids approach [Stam (1999)] was a significant milestone, as it introduced fluid ad-

vection and the Helmholtz-Hodge decomposition, in order to ensure the mass conservation law. However, this approach relied on a discretization of Eulerian space by regular grid, thus making it inappropriate for simulations requiring irregular boundaries. Recently, the DEC method based on unstructured mesh for incompressible fluid simulation, was proposed in [Elcott et al. (2007)]. The DEC method presented several benefits in terms of stability and computational efficiency. However, the context, in which this method was applied, was not aimed at the practical use in medical simulation. We further assess stability, accuracy and computational time of this method, more importantly, improve the method for medical applications in real-time or at least at an interactive rate.

3.2 Mesh Generation

The patient-specific geometry model reconstructed from medical images is a surface model, from which tetrahedral mesh is then created. Meshing the domain is quite tricky, especially because the DEC approach is very sensitive to mesh quality. An ideal mesh in our case is a completely well-centered (CWC) Delaunay triangular/tetrahedral mesh and its circumcentric (Voronoi) dual mesh with non-uniform distribution of resolution. Additionally, each primal or dual element in the mesh is supposed to be as regular as possible (each angle or each edge in the element tends to be equal). Such a mesh possesses several favorable properties. First of all, the orthogonality of primal and dual elements is useful to describe physical quantities. For instance, the direction of flux through a triangle is parallel to the triangle's dual edge. Secondly, the CWC Delaunay triangular/tetrahedral mesh avoids dual elements with conceptually negative volumes, and guarantees the convexity and non self-intersection of the dual mesh, thus allows generalized barycentric interpolation of velocities. Thirdly, multiple-resolution mesh allows to decrease the total number of mesh elements but have lower numerical errors caused by space discretization, by reducing resolution only in some regions but keeping higher resolution in more interesting regions, such as strips near boundary, the interior of aneurysms, small-vortex or high-speed region. Finally, the regularity of each primal/dual element maintains the system stable. The irregular elements, such as flat triangle/tetrahedron, usually result in tiny or negative dual edge. Note that dual edge of zero length is not allowed by the DEC method; otherwise, the star operator \star_2 (a diagonal matrix) contains zero diagonal element, and is not invertible. In practice, either negative or tiny dual edge should be avoided, because they both increase the condition number of the system, and might result in solutions that are not converged or even unstable.

Practically, we are not always able to get a perfect mesh for all geometries, and we measure mesh quality in terms of the percentage of CWC trian-

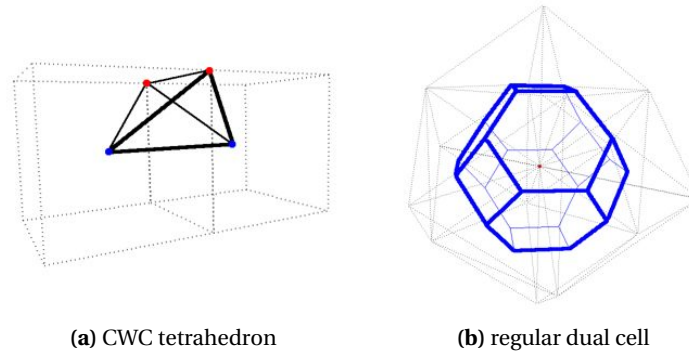


Figure 3.2: BCC-based tiling strategy. (a) The CWC tetrahedron sample, used for tiling, consists of the edge linking the centers of two incident cubes and one shared edge of these two cubes. (b) The dual cell in the tiling mesh are regular; all the dual edges are equal in length.

gles/tetrahedra, the percentage of convex dual faces/3-cells, the length ratio of dual edge to primal edge, and the number of tiny dual edges (i.e., the edges whose length is below 1% or even lower percentage of the average length of primal edge). Generally speaking, a certain mesh resolution is necessary for a high CWC percentage in n dimensions ($n = 2, 3$), and 100% CWC primal mesh is a sufficient (but not necessary) condition for the convexity of all interior dual n -cells (all incident primal n -simplices form a topological sphere for interior vertex, but only a hemisphere for boundary vertex, so the convexity of boundary Voronoi cells also depends on the local boundary shape).

It is relatively easy to obtain a nearly ideal mesh in two dimensions, as an acute triangle is CWC. But it is a much more challenging problem in three dimensions. Since a CWC tetrahedron requires not only its circumcenter to locate inside the tetrahedron, but also all of its triangle faces to be acute; otherwise, it is only weakly well-centered (WWC). For some simple geometries, CWC tetrahedral meshes are available. For instance, the BCC-based spatial tiling strategy [VanderZee et al. (2008)] can create an entire family of triangulations of space using copies of a CWC tetrahedron sample. In the infinite three-dimensional tiling space by unit cubes, the tetrahedron, shown in Figure 3.2(a), consists of the edge linking the centers of two incident cubes and one shared edge of these two cubes. Such a tetrahedron is CWC, and the length of four shorter edges is 0.8660, while the other two longer edges have unit length. The tiling mesh have all the tetrahedra in the same shape and size, and all the dual edges are of the same length 0.3536, so all the dual cells are regular and in the same shape and size as shown in Figure 3.2(b).

Using the tiling strategy described above, an infinite slab, $[-a, a] \times \mathbb{R}^2$ ($a \in \mathbb{R}^+$), can be tiled with this CWC tetrahedron sample. Then we remove the tetrahedra with no intersection with the domain $D = \{(x, y, z) \mid |x| + |y| < a, z \in \mathbb{R}\}$ (Fig-

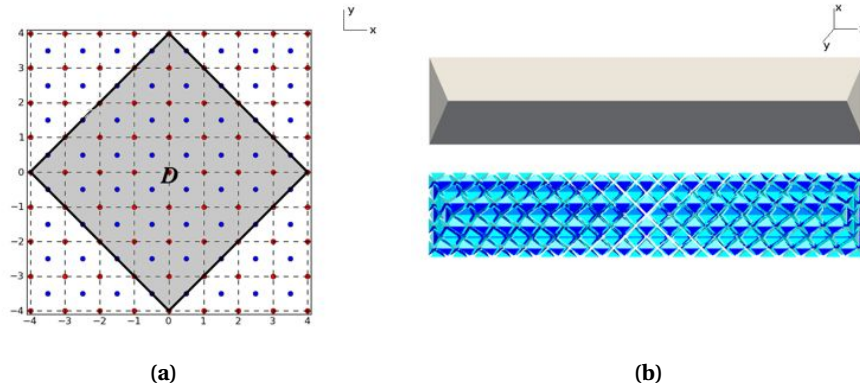


Figure 3.3: Meshing a cuboid using the BCC-based tiling strategy. (a) Remove the tetrahedra outside the domain D . (b) Truncate the infinite domain to get a tiling mesh of the cuboid with two wedge-shaped ends.

Figure 3.3(a) shows the projection of this domain on xy -plane). Since the boundary $B = \{(x, y, z) \mid |x| + |y| = a, z \in \mathbb{R}\}$ only intersects with the tiled tetrahedra on tetrahedron boundaries (i.e., it does not split any tetrahedron), the combination of all the remaining tetrahedra forms a squared tube of infinite length, that is, $\overline{D} = D \cup B$. Then we want to truncate the domain \overline{D} to get a finite segment with convex boundary; otherwise, some dual cells on the boundary are not convex, and have an impact on the interpolation method based on convex vertex set, which we use in the following simulation. Therefore, we design a cuboid geometry with two wedge-shaped ends, $\overline{E} = \{(x, y, z) \mid |x| + |y| + |z| \leq a + b, |z| \geq b\}$ (see in Figure 3.3(b)).

In order to describe a relatively complex boundary, deformation can be performed after removing certain tetrahedra. This process will maintain the majority of tetrahedra to be CWC, and is useful to generate some relatively simple geometries for our validation tests, such as cylinder. First, we start from a cube-tiling space, $S = [-a, a]^2 \times [-b, b]$, and create the tetrahedra based on the BCC-based tiling strategy. In the boundary cubes, centers of boundary faces are added as well to create tetrahedra (see Figure 3.4(a)). Note that boundary tetrahedron is not WWC, as the circumcenter lies outside the tetrahedron. Thus, adding these boundary tetrahedra leads to negative dual edge and self-intersected dual 3-cells, because the triangulation does not meet the Delaunay conditions any more. Second, we remove the tetrahedra which have empty intersection with the cylinder domain, $D_c = \{(x, y, z) \mid x^2 + y^2 < a^2, |z| \leq b\}$, and we obtain an octagonal prism, $\overline{D}_o = \{(x, y, z) \mid |x| \leq a, |y| \leq a, |x| + |y| \leq 2 \cdot \lceil \frac{\sqrt{2}}{2} a \rceil, |z| \leq b\}$. The boundaries of D_c and D_o are displayed in blue and red respectively on the xy projection plane in Figure 3.4(b). Third, we deform \overline{D}_o to \overline{D}_c by moving all the vertices towards the central axis (i.e, multiplying the scaling factors), and finally

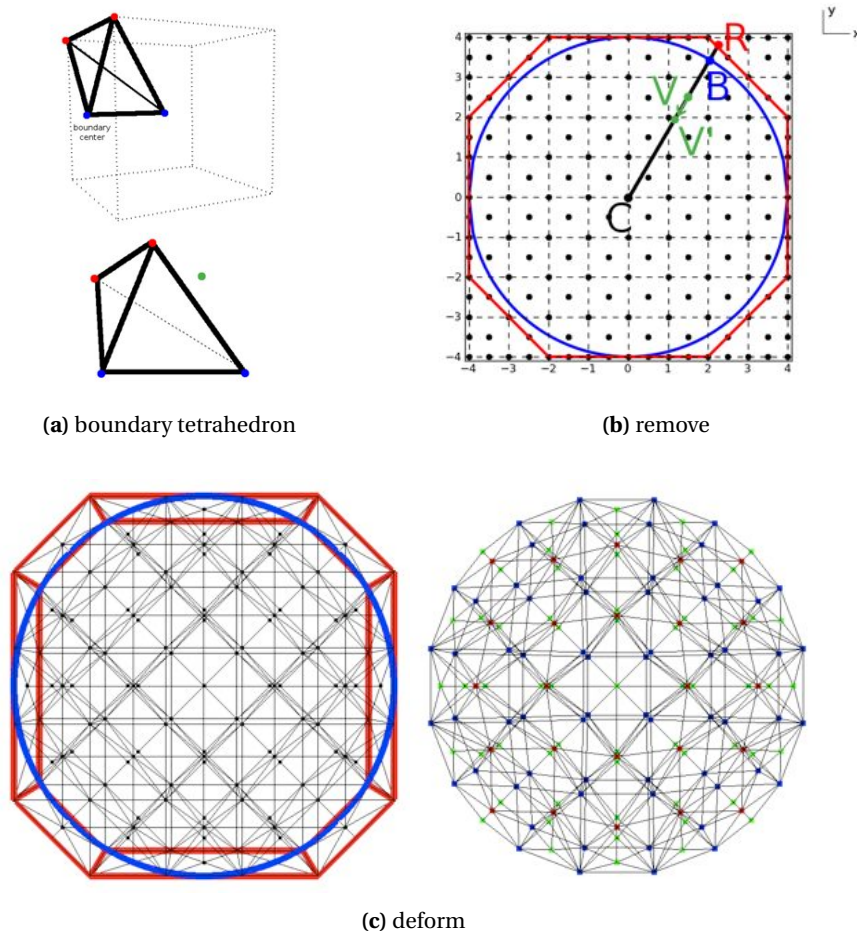


Figure 3.4: Meshing a cylinder by the CWC tiling strategy. (a) On the boundary of the cube-tiling space S , extra centers of boundary faces are added to generate tetrahedron. Note that the boundary tetrahedron is not WWC, as the circumcenter (green point) is outside the tetrahedron. (b) All tetrahedra without intersection with the cylinder domain D_c (inside the blue boundary) are removed, and the rest form an octagonal prism $\overline{D_o}$ (inside the red boundary). Then each vertex $V = (x, y, z)$ in $\overline{D_o}$ is moved to a new position $V' = (x', y', z')$, which is closer to the center $C = (0, 0, z)$. The new position is computed as $|CV'| = \frac{|CB|}{|CR|}|CV|$. (c) The deformation results in the final cylinder mesh.

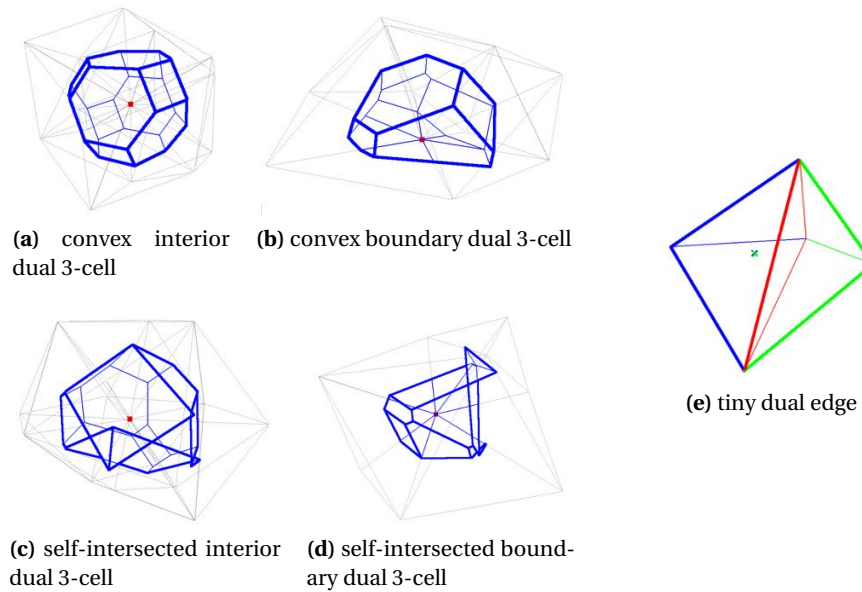


Figure 3.5: Examples of dual elements in the cylinder model. (a)-(d) The incident tetrahedra (in black dotted lines) of a vertex form a topological sphere in the interior, or only hemisphere on the boundary. (e) The dual edge of the red primal face, defined as the line segment between the tetrahedron circumcenters displayed by the crosses, is hardly visualizable in this scale.

we get a cylinder mesh as shown in Figure 3.4(c).

The deformed boundary tetrahedra and the scaled tetrahedra result in non CWC tetrahedra, self-intersected dual 3-cells, as well as tiny and negative dual edges. Some examples of dual elements in the mesh are shown in Figure 3.5. However, the percentage of CWC tetrahedra can reach 90% (it also depends on the mesh resolution), and such a mesh is relatively regular, as most of the tetrahedra in such a mesh are roughly the same.

Nevertheless, these are only solutions to a limited amount of simple geometries. For the complex patient-specific geometries, we use the interleaved optimization algorithm based on Delaunay refinement and Lloyd optimization [Tournois et al. (2009)], implemented using the CGAL library [CGAL]. Each refinement step acts on the size of elements, while each optimization step acts on the shape of elements. Using this method, we can also define a size field to obtain anisotropic and non-uniform mesh. We control the fidelity of the generated mesh to the previously obtained surface model, by specifying the distance tolerance between the two surfaces. After several iterations, we are able to generate two-dimensional meshes with over 99% CWC triangles and 100% convex dual faces in most cases, and three-dimensional meshes with over 90% CWC tetrahedra but only about 70% convex dual 3-cells. Additionally, in the tetrahedral mesh, the ratio of the minimum length of dual edge to the average length of pri-

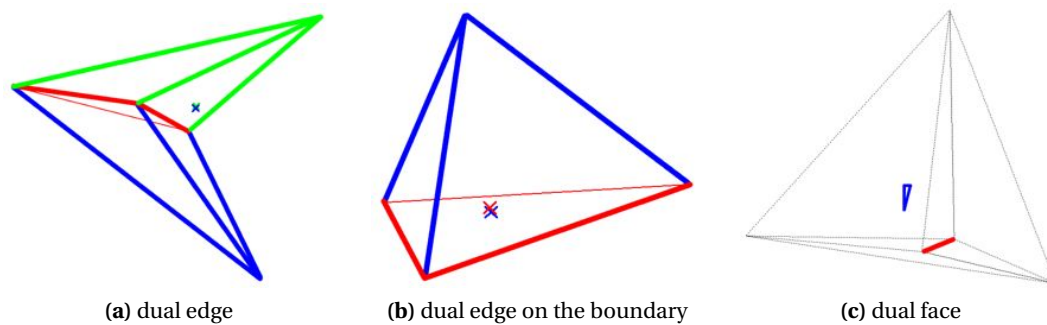


Figure 3.6: Examples of low-quality dual elements in the aneurysm model. (a) (b) We can hardly see the length of the dual edges, linking the circumcenters (displayed by crosses) of two incident tetrahedra (in green and in blue), or the circumcenters of the unique incident tetrahedron (in blue) and the primal face (in red) on the boundary. (c) The dual face (in blue), constructed by the circumcenters of the non WWC tetrahedra (in black), does not intersect with its primal edge (in red).

mal edges is less than 10^{-4} (100 times lower compared to the triangular mesh). There are some extreme flat tetrahedra in the generated tetrahedral mesh, leading to the irregularity and abnormality of dual elements. Examples of low-quality elements are illustrated in Figure 3.6.

3.3 Numerical Solution

To simplify the simulation, we model blood as an incompressible Newtonian fluid of constant density, $\rho = 1.069 \times 10^3 \text{ kg/m}^3$, and constant viscosity, $\mu = 3.5 \times 10^{-3} \text{ kg/(m} \cdot \text{s)}$. According to Dr. Penney's report [Penney (2002)], the Reynolds number of blood flow varies with a wide range, from far smaller than 1.0 in capillary to larger than 3,000 in aorta. In this work, however, we just consider the blood flow near intracranial aneurysms with relatively small Reynolds number ranging from 100 to 1,000, which satisfies the laminar assumption. Thus it is reasonable to describe the behavior of blood flow using the unsteady incompressible Navier-Stokes equations (Equation 2.1). In this chapter, we focus on fluid simulation, and ignore vessel deformation and its influence on the fluid. Hence vessel walls are assumed to be rigid.

The DEC method for fluid simulation is a vortex method, first introduced in the field of computer graphics [Elcott et al. (2007)]. It is based on unstructured mesh which is more suitable to describe irregular boundary of anatomical geometries than regular grids. As a matter of fact, vorticity plays an important role in fluid dynamics analysis, as in many cases it is beneficial to describe flow dynamics in terms of the evolution of vorticity field. This is particularly true in the case of aneurysm flow, where the bulge along the artery creates vortices, im-

pecting both the expansion of aneurysm and coil embolization procedure. The DEC approach is such a vortex method, using vorticity-based formulations of the Navier-Stokes equations (Equation 2.2). We recall the equations here:

$$\begin{aligned}\frac{\partial \boldsymbol{\omega}}{\partial t} + \mathcal{L}_v \boldsymbol{\omega} &= \frac{\mu}{\rho} \Delta \boldsymbol{\omega} + \frac{1}{\rho} \nabla \times \boldsymbol{f}, \\ \nabla \boldsymbol{v} &= 0, \quad \boldsymbol{\omega} = \nabla \times \boldsymbol{v},\end{aligned}$$

where the second term $\mathcal{L}_v \boldsymbol{\omega}$ is the advection term, translating the idea that vorticity elements are pushed forward by the fluid velocity. The DEC approach handles this term in a novel and particular way by the backtracking step, which enforces conservation of circulation at a discrete level, as well as computational stability. Hence it reduces numerical diffusion because of the circulation-preserving strategy, and makes it possible to use larger time steps and thus results in faster simulations.

In this section, we provide a numerical framework for solving the fluid equations based on the work of [Elcott et al. (2007)]. The fluid domain, state variables and several vector calculus operators are explained in the language of DEC. At last, we illustrate how to combine all of these objects in DEC to solve the vorticity-based Navier-Stokes equations.

3.3.1 Discretization

Although only three-dimensional fluid flows exist in reality, we also simulate conceptual two-dimensional fluid for testing and validating our approach. In this section, the DEC algorithm is illustrated in three dimensions, while the two-dimensional framework can be built similarly. The fluid domain \mathcal{D} is discretized as a primal mesh, from which its dual mesh can be defined. These meshes are established as presented in Section 2.5.

3.3.1.1 State Variables

State variables of fluid flow, such as pressure, velocity and vorticity, are converted into discrete forms (i.e., integral values over either primal or dual elements) in accordance with their physical meanings.

- Pressure, in continuum fluid dynamics, is defined as the amount of force acting on unit area, but unlike stress, it is a pointwise scalar quantity. Usually, absolute pressure at a point makes no sense; what plays an important role in physics is pressure gradient, a vector field which reflects the value and direction of the greatest rate of pressure change in space. Pressure gradient is integrable along a line, and this line integral gives the pressure difference between its starting and ending point. Accordingly, in the discrete

setting, we define the pointwise pressure as a dual 0-form P , represented as a vector of size $|T|$, denoted \mathbf{P} , the i^{th} element of which is the pressure on the dual vertex $\star t_i$ of the i^{th} tetrahedron t_i , written as $\mathbf{P}[i] = P(\star t_i)$. And discrete pressure gradient is defined as a dual 1-form G_P , represented as a vector of size $|F|$, denoted \mathbf{G}_P . $\mathbf{G}_P[i] (= G_P(\star f_i))$ equals to the pressure difference between two ends of the dual edge $\star f_i$ (Equation 3.1). Although pressure gradient is described in the format of scalar, its direction is given by the orientation of its corresponding dual edge.

$$\mathbf{G}_P[i] = G_P(\star f_i) = P(\star t_f[1]) - P(\star t_f[0]), \quad (3.1)$$

where $t_f[0]$ and $t_f[1]$ are two incident tetrahedra on f_i , and $\overrightarrow{t_f[0]t_f[1]}$ is in the same orientation as $\star f_i$, and also defines the direction of $\mathbf{G}_P[i]$. One of the terms on the right should be replaced by the $P(c(f_i))$, if f_i is on the boundary.

- Flux is originally defined as the amount of fluid passing through unit area per unit time, thus is an area density integrable on any surface. Consequently, discrete flux is a primal 2-form U , represented as a vector of size $|F|$, written as \mathbf{U} . $\mathbf{U}[i] (= U(f_i))$ is the integral value over triangle f_i , whose orientation indicates whether the flux flows backward or forward, since the direction of the dual edge $\star f_i$ defines the flux direction. In the algorithm, U is used to describe the velocity field, we will see how to convert flux to velocity vector field in Section 3.3.2.
- Vorticity is the physical term to describe the tendency of fluid element spinning. More formally, it measures the local angular rate of rotation, and is defined as the circulation per unit area at a point. Therefore, vorticity is discretized by a dual 2-form, Ω , represented as a vector of size $|E|$, denoted $\mathbf{\Omega}$. $\mathbf{\Omega}[i] (= \Omega(\star e_i))$ is the integral over the dual face $\star e_i$, whose orientation gives the circulating direction.

3.3.1.2 Operators

Two types of operators, Hodge stars \star and discrete exterior derivatives d , are defined in the previous chapter. Here, we will explain how they operate on state variables in fluid dynamics. Variables are transferred from primal p -simplex to dual $(n - p)$ -cell or vice-versa through Hodge stars. Take the case of $\star_2 U$ for example, if triangle f is small enough, $U(f)/|f|$, the averaged flux through f , is an approximation of velocity perpendicular to f . If dual edge $\star f$ is also small enough, $(U(f)/|f|) \cdot \star f$ is an approximation of the integral value of velocity field along $\star f$. So \star_2 transfers the primal 2-form U to the dual 1-form $\star_2 U$, and $(\star_2 U)[i] = \frac{|\star f_i|}{|f_i|} U[i]$. On the other hand, d maps p -forms to $(p + 1)$ -forms on

the primal mesh, while d_p^T maps forms on the dual mesh similarly. Take d_2U for example, if $d_2[i][j] = +1$ or -1 , f_j is a triangle face of tetrahedron t_i , and the normal of f_i points inside or outside of t_i ; otherwise, $d_2[i][j] = 0$, which means f_j and t_i are not incident. As a consequence, $d_2[i]U$ accumulates signed values of discrete flux on all triangle faces of t_i (the directions are considered by the signs in the meantime). For instance, the tetrahedron example in Figure 2.10, $d_2U = U(f_0) - U(f_1) + U(f_2) - U(f_3)$. So d_2U gives a primal 3-form, and $(d_2U)[i]$ equals to the amount of fluid flowing into t_i .

All the vector calculus operators involved in our computation can be expressed by \star and d , such as gradient of pressure (∇P), divergence of velocity ($\nabla \cdot U$), curl of velocity ($\nabla \times U$), and Laplace operators (Δ).

- **Gradient** of pressure is already given by Equation 3.1, which we can rewrite as

$$G_p = \nabla P = d_2^T P.$$

- **Divergence** of velocity, in continuum theories, is the volume density of the outward flux from an infinitesimal volume around a given point, while the discrete counterpart $\nabla \cdot U$ is a dual 0-form. Remember that $(d_2U)[i]$ equals to the amount of fluid flowing into the tetrahedron t_i , therefore, $\nabla \cdot U$ can be represented as

$$\nabla \cdot U = -\star_3 d_2U.$$

- **Curl** of velocity is the mathematical definition of vorticity. In DEC, we can easily get Ω from U as follows: \star_2U gives an integral value of velocity field along every dual edge, and then d_1^T makes a sum on each dual face $\star e$ by accumulating the signed \star_2U on all dual edges incident on $\star e$, which gives the circulation around the boundary of $\star e$. Hence we have

$$\Omega = \nabla \times U = d_1^T \star_2 U.$$

- **Laplace** is defined as $\delta d + d\delta$ in [Elcott et al. (2007)], mapping p -forms to p -forms on the primal mesh. In detail,

$$\Delta_0 = \delta_1 d_0 = \star_0^{-1} d_0^T \star_1 d_0,$$

$$\Delta_1 = \delta_2 d_1 + d_0 \delta_1 = \star_1^{-1} d_1^T \star_2 d_1 + d_0 \star_0^{-1} d_0^T \star_1,$$

$$\Delta_2 = \delta_3 d_2 + d_1 \delta_2 = \star_2^{-1} d_2^T \star_3 d_2 + d_1 \star_1^{-1} d_1^T \star_2,$$

$$\Delta_3 = d_2 \delta_3 = d_2 \star_2^{-1} d_2^T \star_3.$$

3.3.2 Solving Fluid Equations

In order to update vorticity for each time step h , derivative in Equation 2.2 is approximated by finite difference, resulting in

$$\omega' = \omega - h\mathcal{L}_v\omega + \frac{\mu h}{\rho}\Delta\omega + \frac{h}{\rho}\nabla \times \mathbf{f},$$

the right side of which consists of the advection term, the viscous term and the external force term:

- Simply speaking, the **advection term** describes the idea that the local spin is pushed forward along the direction of the velocity. This is consistent with Kelvin's circulation theorem: the circulation around a closed curve moving with the fluid remains constant with time. In the DEC approach, the discrete vorticity is conserved by extending Kelvin's theorem to the discrete version: the circulation around the loop of each dual face's boundary keeps constant as the loop is advected by fluid flow. So we run the backtracking step to find out where the current dual face comes from, and accumulate the circulation around the backtracked dual face, and then assign this value to the current one (see Figure 3.7). This step makes the computation circulation-preserving at a discrete level, as well as stable, because the maximum of the new field is never larger than that of the previous field. Backtracking a point \mathbf{p} at time t through velocity field over a time step h can be implemented simply as $\mathbf{p}' = \mathbf{p} - \mathbf{v}_{\mathbf{p}} \times h$ ($\mathbf{v}_{\mathbf{p}}$ is velocity at \mathbf{p}), or using more advanced schemes, such as Runge-Kutta methods. Velocity at the backtracked point \mathbf{p}' is interpolated from the velocity samples at tetrahedron circumcenters by computing the barycentric coordinates over the dual 3-cells which contains \mathbf{p}' based on the method of [Warren et al. (2007)]. However, this method is only for convex sets. So if some of the dual 3-cells are not convex, there might be negative barycentric coordinates. We modify the weight function by using a small positive value instead of negative value of $\mathbf{n}_j \cdot (\mathbf{v} - \mathbf{x})$. Anyway, the modification only assigns reasonable values for all barycentric coordinates, but does not really fix the problem caused by non convex dual 3-cells.
- The **viscous term** can be translated into $\frac{\mu h}{\rho} (\Delta_1 \star_1^{-1}) \Omega$, and added directly. But an implicit scheme could be chosen for the purpose of stability, which is implemented by solving Ω' in the following linear system:

$$\Omega' - \Omega = \frac{\mu h}{\rho} (\Delta_1 \star_1^{-1}) \Omega'. \quad (3.2)$$

- When the external force is expressed through the vector \mathbf{F} of their resulting fluxes on each triangle, the **external force term** is simply $\frac{h}{\rho} d_1^T \star_2 \mathbf{F}$.

After updating the vorticity, the recovery of velocity field \mathbf{v} from vorticity Ω is needed for backtracking in the next iteration. Since U is divergence-free, it can be expressed by a primal 1-form as $U = d_1 \Phi$ (note that $d_2 d_1 = 0$). Thus we have the linear system $(d_1^T \star_2 d_1) \Phi = \Omega$, yet which has infinitely many solutions. In

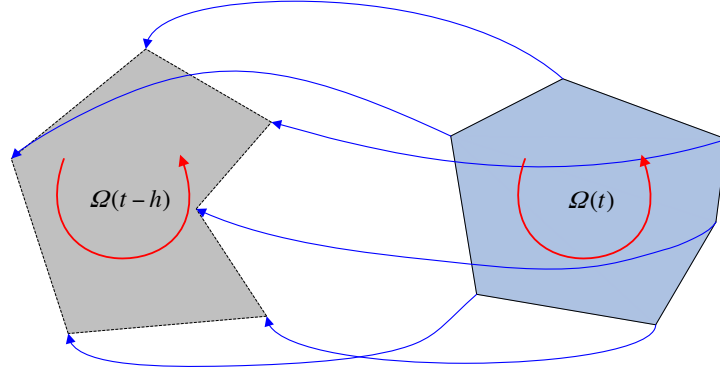


Figure 3.7: Backtracking. At the current time step $t_n = t$, given the velocity field, each dual vertex (on the right) are backtracked to its position at the previous time step $t_{n-1} = t - h$ (on the left). The circulation around the loop of dual face boundary at time t_n is forced to equal the circulation of the backtracked loop at time t_{n-1} , i.e., $\Omega(t) = \Omega(t - h)$.

order to determine a certain solution of Φ , an extra requirement, $d_0^T \star_1 \Phi = 0$, which means that Φ is divergence-free, gives a Poisson equation as follow:

$$\Delta_1 \Phi = (\star_1^{-1} d_1^T \star_2 d_1 + d_0 \star_0^{-1} d_0^T \star_1) \Phi = \star_1^{-1} \Omega.$$

In addition, boundary constraints are added into the equation by the Lagrange multiplier method, leading to

$$\left(\begin{array}{c|c} \star_1 \Delta_1 & d_1^T \\ \hline d_1' & 0 \end{array} \right) \begin{pmatrix} \Phi \\ \lambda \end{pmatrix} = \begin{pmatrix} \Omega \\ U_{bd} \end{pmatrix}, \quad (3.3)$$

where U_{bd} stores the flux on the boundary triangles, and d_1' is a sub-matrix of d_1 only with the lines corresponding to the boundary triangles. Once the flux U is obtained from $U = d_1 \Phi$, there exists a unique velocity vector v_t at each dual vertex $\star t$, whose projection along any incident dual edge $\star f_t$ is consistent with the integral value of velocity along the dual edge $\star f_t$, that is $(\star_2 U)(\star f_t)$. Let i be the index of f_t in the list F , then we have

$$\frac{1}{\star_2[i][i]} \overrightarrow{\star f_t} \cdot v_t = U[i].$$

For each dual vertex, by combining this equation of four incident dual edges, we get a linear system:

$$A_t v_t = U_t,$$

where A_t is a 4×3 matrix. When the flux U is strictly divergence-free, this equation has a single unique solution of v_t . But for numerical computation, we solve the equation below instead:

$$(A_t^T A_t) v_t = A_t^T U_t.$$

Last but not the least, we illustrate how to set boundary conditions. We perform iterations of evolving vorticity in time with given fluxes through all the boundary triangles at time t . As we assume vessel wall to be rigid in this chapter, thus no-slip and no-penetration conditions are applied at vessel walls; fluxes and velocity are set zero at vessel walls. At the inlet(s) and outlet(s), we choose two conditions for different experiments, i.e., a sinusoidally pulsatile flow and non-varying flow (the mean value of the pulsatile flow). For the flow at inlet, we use the mean and maximum velocities based on the measurements from MRI [Marshall et al. (2004)]. As the blood is assumed to be incompressible, the total flux at the outlet(s) should be equal to the inflow. If there are more than one outlet, the distribution of the blood flow is estimated by Bernoulli's principle in the assumption that the pressure is identical at every outlet.

See Algorithm 3.1 for the overview of our computation process.

3.4 Accelerating Techniques

In order to achieve real-time simulation or at least at an interactive rate, often required by practical use in medical training or surgery planning, we apply various techniques to accelerate the simulating process. It should be noted that most of the computational time comes from the backtracking step. Because the backtracked points should be located in the mesh, i.e., find which dual face/dual 3-cells contains this point. Then the neighboring triangle/tetrahedron centers are used as sample points for interpolation. The computational time relates to the number of triangles/tetrahedra in the mesh and the backtracking scheme as well. The second most time-consuming steps are solving diffusion and Laplacian linear sparse systems (Equation 3.2 and Equation 3.3) in each iteration. As other numerical approaches such as FEM, matrix size of the system directly relates to the number of elements in the mesh. Obviously, in order to reduce computational time for each iteration, we need to limit mesh resolution, and rely on optimized linear solvers as well as efficient backtracking algorithms. Additionally, improvement of the system stability allows larger time step, which reduces the number of iterations to simulate unit real time.

3.4.1 Limit Mesh Resolution

Generally speaking, a higher mesh resolution permits to achieve a higher level of accuracy in the solution. However, when the error induced by a lower-resolution mesh is acceptable, the objective is then to reach the best trade-off between accuracy and computational time. We create a series of meshes describing the same geometry but in different resolution, and simulate the blood flow by providing the same inflow and outflow for all the meshes. Afterwards, we compare

Algorithm 3.1 Main steps of the fluid simulation using the DEC method

```

//Initialize
Load mesh and compute  $d$  and  $\star$  operators
 $C \leftarrow d_1^T \star_2$ 
 $L \leftarrow \star_1^{-1} d_1^T \star_2 d_1 + d_0 \star_0^{-1} d_0^T \star_1$ 
 $L' \leftarrow \text{LagrangeMultiplier}(L, \star_1, d_1)$ 

//Time stepping  $t \leftarrow t + h$ 
loop
  //Advection term
  for each tetrahedron  $t_i$  do
     $\hat{c}_i \leftarrow \text{backtrack}(c(t_i))$ 
     $\hat{v}_i \leftarrow \text{interpolateVelocity}(\hat{c}_i)$ 
  end for
  for each dual face  $\star e$  do
     $\Omega(\star e) \leftarrow 0$ 
    for each dual edge  $(c_i, c_j)$  incident on  $\star e$  do
       $\Omega(\star e) \leftarrow \Omega(\star e) + \frac{1}{2}(\hat{v}_i + \hat{v}_j) \cdot (\hat{c}_i - \hat{c}_j)$ 
    end for
  end for

  //External force term
   $\Omega \leftarrow \Omega + \frac{h}{\rho} C F$ 

  //Viscous term
   $\Omega \leftarrow \Omega' = \text{linearSolver}((1 - \frac{\mu h}{\rho} L \star_1^{-1}) \Omega' = \Omega)$ 

  //Recovery of velocity
   $U_{bd} \leftarrow \text{setBoundaryConditions}(t)$ 
   $\Phi \leftarrow \text{linearSolver}(L'(\Phi | \lambda) = (\Omega | U_{bd}))$ 
   $U = d_1 \Phi$ 
  for each tetrahedron  $t$  do
     $v_t \leftarrow \text{linearSolver}((A_t^T A_t) v_t = A_t^T U_t)$ 
  end for
end loop

```

the results obtained on these meshes, and suggest a proper mesh resolution for the blood flow simulation considering both accuracy of the result and computational time. Moreover, a multi-resolution mesh is also a feasible option to reduce the total number of elements while maintaining high resolution in interesting regions, such as strips near boundary and the interior of aneurysms where more details of the flow are supposed to be preserved.

3.4.2 Optimize Linear Solvers

Many numerical techniques can be used to improve the computational efficiency of solving linear equations, especially sparse linear system, which is the case in our computation. If vessel wall is assumed to be rigid, the mesh is static (Eulerian approach). As a result, operators as well as diffusion and Laplacian matrices are constant over time, and can be efficiently pre-computed due to their sparsity. When dealing with relatively small systems, direct inversion of the matrices is often the best approach, which can be performed offline and stored for online computation. This ensures real-time or near real-time computation, which is typically the case when dealing with two-dimensional problems. For larger systems, therefore, we rely on solvers which factorize the matrices only once during initialization. Within each iteration, the solution to the equations is computed by efficient sparse triangular solve operations using the pre-computed factorized matrices. In our experiments we use the multi-threaded sparse symmetric indefinite solver in the Pardiso library [Schenk and Gärtner (2006)] to factorize and solve the diffusion and Laplacian matrices.

3.4.3 Improve Backtracking Algorithms

In the backtracking step, given the coordinates of a point in n -dimensional space ($n = 2, 3$), we need to locate this point in the mesh (whether it is in the interior of the mesh, and in which dual n -cell it lies). When $n = 2$ ($n = 3$), we use a quadtree (an octree) structure to partition the bounding box of the mesh by recursively subdividing it into four quadrants (eight octants), and each leaf, geometrically being a square (cube), only intersects with a small number of dual faces (dual 3-cells). The construction of the quadtree (octree) is done only once during the initialization.

3.4.4 Improve Stability

Besides reducing the computational time for each iteration, the ability to support large time steps while keeping the system stable is an advantage provided by the DEC method, as a result of the backtracking strategy for computing the advection term. Moreover, we use high-order Runge-Kutta methods to backtrace points, and further improve the stability. However, the higher order we apply, the more computational time we need. Therefore, we test different backtracking schemes and make a better compromise between the simulated results and the computational time.

3.5 Experiments and Results

We have made a series of experiments both in two and three dimensions, involving different geometry models to assess the DEC approach applied in the field of blood flow simulation. Assuming that the blood is a Newtonian fluid, the density and viscosity are set as constants, $1.069 \times 10^3 \text{ kg/m}^3$ and $3.5 \times 10^{-3} \text{ kg/(m} \cdot \text{s)}$, respectively. The viscosity is so strong, and a typical value of velocity is at the level of 100 mm/s , thus the corresponding Reynolds number is less than 1.0×10^3 , small enough for the laminar assumption. As a result, laminar flow with flux boundary conditions at both inlet and outlet sections is considered in our following experiments.

First of all, we have performed three groups of comparative tests against FLUENT software¹ in two-dimensional and three-dimensional space. In this case, we mostly aim at validating numerical accuracy of the DEC method rather than the actual ability to precisely describe the actual blood flow features near aneurysm, because such an analysis is very complex to achieve due to the present difficulties in acquiring real velocity data in vivo, particularly in very small vessels such as the ones in the brain. Each group of the comparison between DEC and FLUENT consists of blood flow simulation on several identical meshes with the same geometry but different resolution. Secondly, we have tested the convergence of the DEC method in these simulations. We calculate the relative difference of velocity field between two iterations. If the relative difference is less than a given criterion, we believe the result is converged. If the solution is not converged, but only oscillates in a certain range, we believe it is stable. Thirdly, through the experiments on different sizes of one time step and different backtracking schemes, we conclude a rough rule to set time step as large as possible while the simulation remains converged (or at least stable) and the error of the result remains in an acceptable tolerance. Finally, we have counted the computational time of each iteration and each step in one iteration.

3.5.1 Experiments of Two-Dimensional Simulation

In two-dimensional experiments, we pick up three interesting geometries imitating the profiles of a T-junction vessel without any pathological abnormality (Figure 3.8(a)), an aneurysm of large neck (Figure 3.12(a)), and an aneurysm of small neck (Figure 3.13(a)). We start with depicting the outline of vessels and aneurysms, then truncate the vessels manually and define inlet(s) and outlet(s) of a local region for the simulation. The boundary of this region is described by a series of line segments, which is the input for generating triangular meshes by interleaving Delaunay triangulation and Lloyd optimization.

¹FLUENT is a commercial product of ANSYS (<http://ansys.com>), widely used in industries.

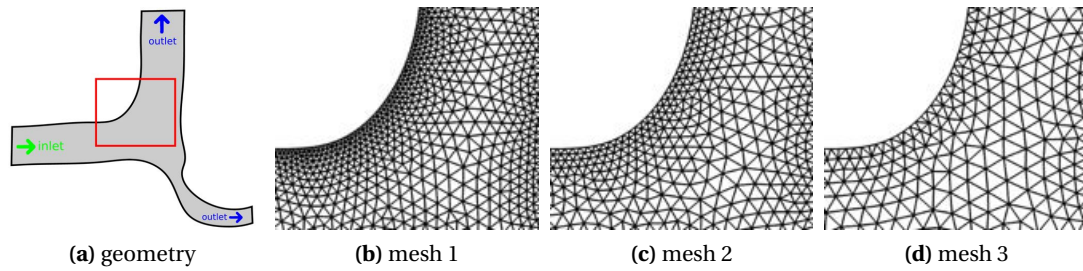


Figure 3.8: Geometry model of the T-junction vessel. (a) The wall, inlet and outlets are defined by the boundary curve. (b)-(d) Three meshes (zoom-ins in the red rectangle) are generated in different resolution.

mesh	number of triangles	average edge length (mm)	CWC triangles (%)	convex dual faces (%)
mesh 1	7258	0.1957	97.88	100.00
mesh 2	3908	0.2755	99.67	100.00
mesh 3	1952	0.3893	93.85	100.00

Table 3.1: Mesh quality of the vessel model.

The first group of simulations using the vessel model is performed on twenty meshes composed of different numbers of triangles, ranging from 1,952 to 7,258. Here we display a local region of three meshes in Figure 3.8, the finest (mesh 1), the medium (mesh 2), and the coarsest (mesh 3) in the twenty meshes. A varying size field is specified over the region to generate smaller triangles near the boundary. The mesh resolution (described as the average length of all edges in the mesh) and mesh quality of the three meshes are summarized in Table 3.1. In each mesh, the percentage of completely well-centered (CWC) triangles is over 93%, and the dual faces are all convex. Generally speaking, a certain resolution of the mesh is necessary for a high CWC percentage. In the twenty meshes we generated for the vessel geometry, when the number of the triangles goes above 2,500, we can always obtain a mesh of over 97% CWC triangles after several interleaved iterations. Moreover, most triangles in the mesh are nearly regular; the edges of each triangle are almost equal in length. As a result, the local length ratio of dual edge and primal edge is around 0.577. A few short dual edges (compare to the local primal edge) appear only near the boundary at the sharp corners. For all the two-dimensional geometries, it is usually possible to generate such a high-quality mesh with high CWC and convex percentage, as well as regular triangles.

We first compare the contours of velocity magnitude and the streamlines computed by DEC and FLUENT in Figure 3.9. The unit of velocity displayed in all

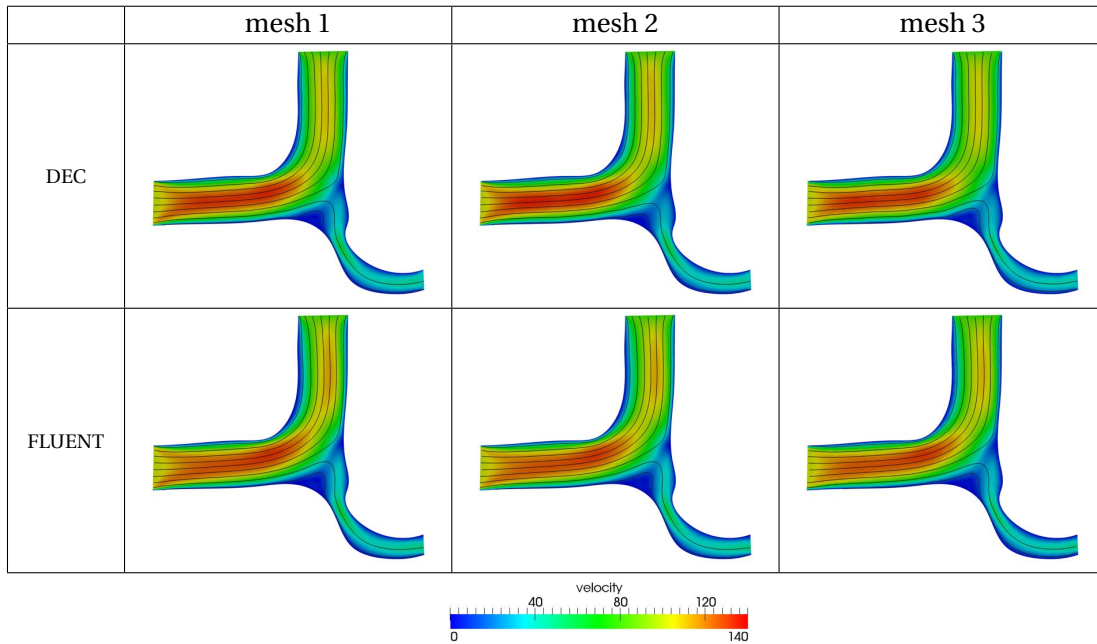


Figure 3.9: Comparison of velocity field on the vessel model. The contours of velocity magnitude and streamlines are computed by DEC and FLUENT on the identical meshes, which are mesh 1 of 7,258 triangles, mesh 2 of 3,908 triangles, and mesh 3 of only 1,952 triangles.

the figures is mm/s by default. Secondly, we pick up three lines across the inlet and the two outlets respectively (see Figure 3.10(a)), and plot the profiles of the velocity magnitude over these three lines in Figure 3.10(b)-(d). Here we compare the result computed by DEC on the three meshes (the curves in different colors) to the result computed by FLUENT on mesh 1, the finest mesh (the dotted curve in black). These comparisons show the similarity in the results of both methods. When using the coarsest mesh of 1,952 triangles, a small reduction of the velocity magnitude can be found in both methods. But the main features of the velocity field still remain the same, such as the flow pattern (characterized by the streamlines) and the variation of the velocity field in space (characterized by the profiles).

In order to further understand the numerical dissipation caused by the reduction of mesh resolution, we compare the kinetic energy computed by both methods. If we approximately consider that the kinetic energy computed on the finest mesh corresponds to zero numerical dissipation, the numerical dissipation can be measured by the loss of kinetic energy on coarser meshes compared to the finest one. We list average edge length and kinetic energy of the twenty meshes, and draw the energy variation as the reduction of mesh resolution in Figure 3.11. As the mesh resolution decreases (i.e., the average edge length increases), the energy computed by DEC (the blue curve) and by FLUENT (the

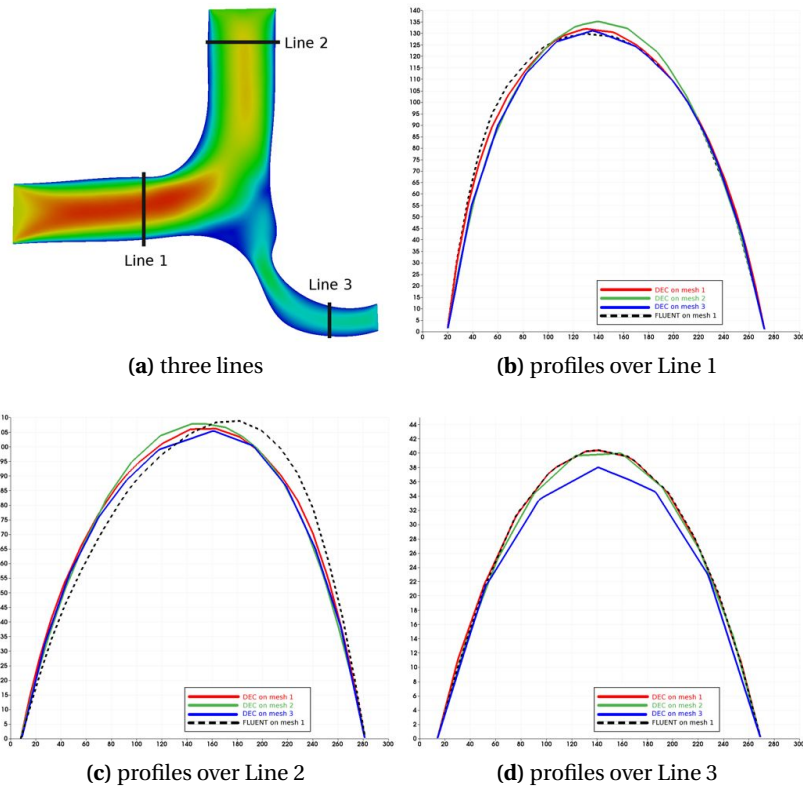
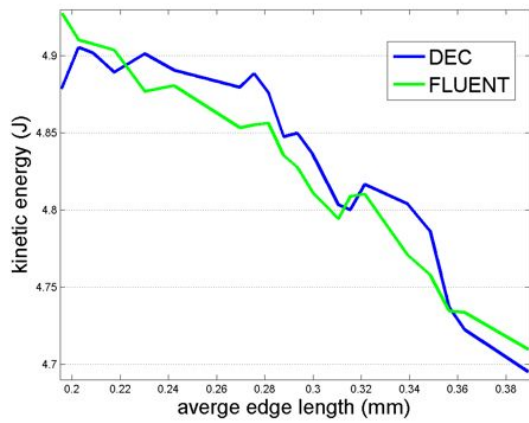


Figure 3.10: Comparison of velocity profiles on the vessel model.



mesh	number of triangles	average edge length (mm)	kinetic energy by DEC (J)	kinetic energy by FLUENT (J)
1	7258	0.1957	4.879	4.928
2	6786	0.2027	4.905	4.910
3	6432	0.2085	4.902	4.908
4	5923	0.2175	4.889	4.904
5	5405	0.2302	4.901	4.877
6	4952	0.2423	4.891	4.881
7	4086	0.2697	4.880	4.853
8	3908	0.2755	4.888	4.855
9	3746	0.2814	4.876	4.856
10	3585	0.2878	4.848	4.835
11	3445	0.2934	4.850	4.828
12	3304	0.2998	4.836	4.811
13	3086	0.3105	4.803	4.794
14	2992	0.3154	4.800	4.809
15	2884	0.3214	4.817	4.810
16	2592	0.3391	4.804	4.771
17	2452	0.3485	4.786	4.758
18	2342	0.3564	4.737	4.735
19	2258	0.3627	4.723	4.734
20	1952	0.3893	4.695	4.710

Figure 3.11: Mesh resolution and kinetic energy of the vessel model. The kinetic energy variation as the reduction of mesh resolution is drawn on the left for both DEC (in blue) and FLUENT (in green), while the figures are given in the table on the right.

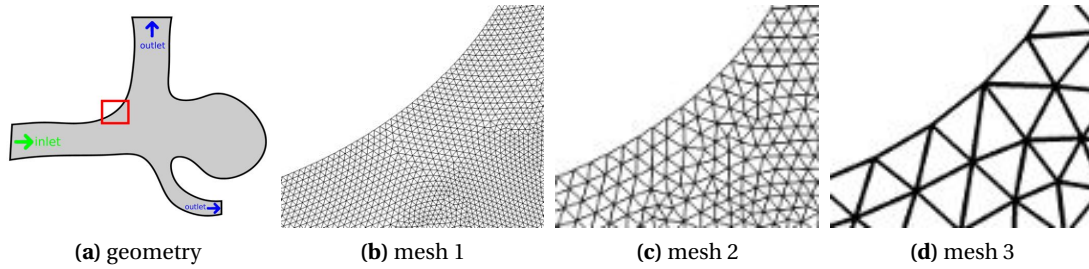


Figure 3.12: Geometry model of the large-neck aneurysm. (a) The wall, inlet and outlets are defined by the boundary curve. (b)-(d) Three meshes (zoom-ins in the red rectangle) are generated in different resolution.

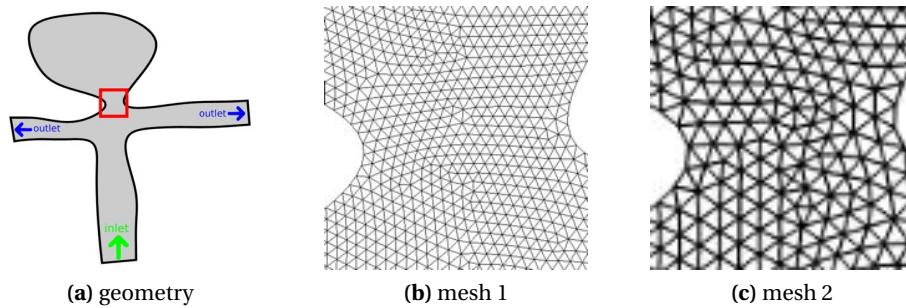


Figure 3.13: Geometry model of the small-neck aneurysm. (a) The wall, inlet and outlets are defined by the boundary curve. (b) (c) Two meshes (zoom-ins in the red rectangle) are generated in different resolution.

green curve) both diminishes, and almost in the same rate. Although the DEC method does not have higher order accuracy compared to FLUENT, we do not find any additional numerical dissipation in this experiment.

Similarly, the other two groups of two-dimensional comparative tests are performed on two or three meshes of different resolution for each geometry model. The meshes of the large-neck and the small-neck aneurysm model are displayed in Figure 3.12 and Figure 3.13, while mesh quality is summarized in Table 3.2 and Table 3.3 respectively. Triangles are nearly regular and uniform in each mesh, which guarantees high quality in terms of CWC triangles and convex dual faces.

Figure 3.14 and Figure 3.16 display the velocity results not only over the whole region, but also in the local region of aneurysm sac using a logarithmic scale for velocity magnitude, since the flow is much slower there. Two lines, one across the inlet and the other across the aneurysm sac, are chosen to plot the profiles for each geometry model (see Figure 3.15 and Figure 3.17). Even when the mesh resolution decreases by 10 times for the large-neck model and 4 times for the small-neck model, the contours and profiles are almost the same, and

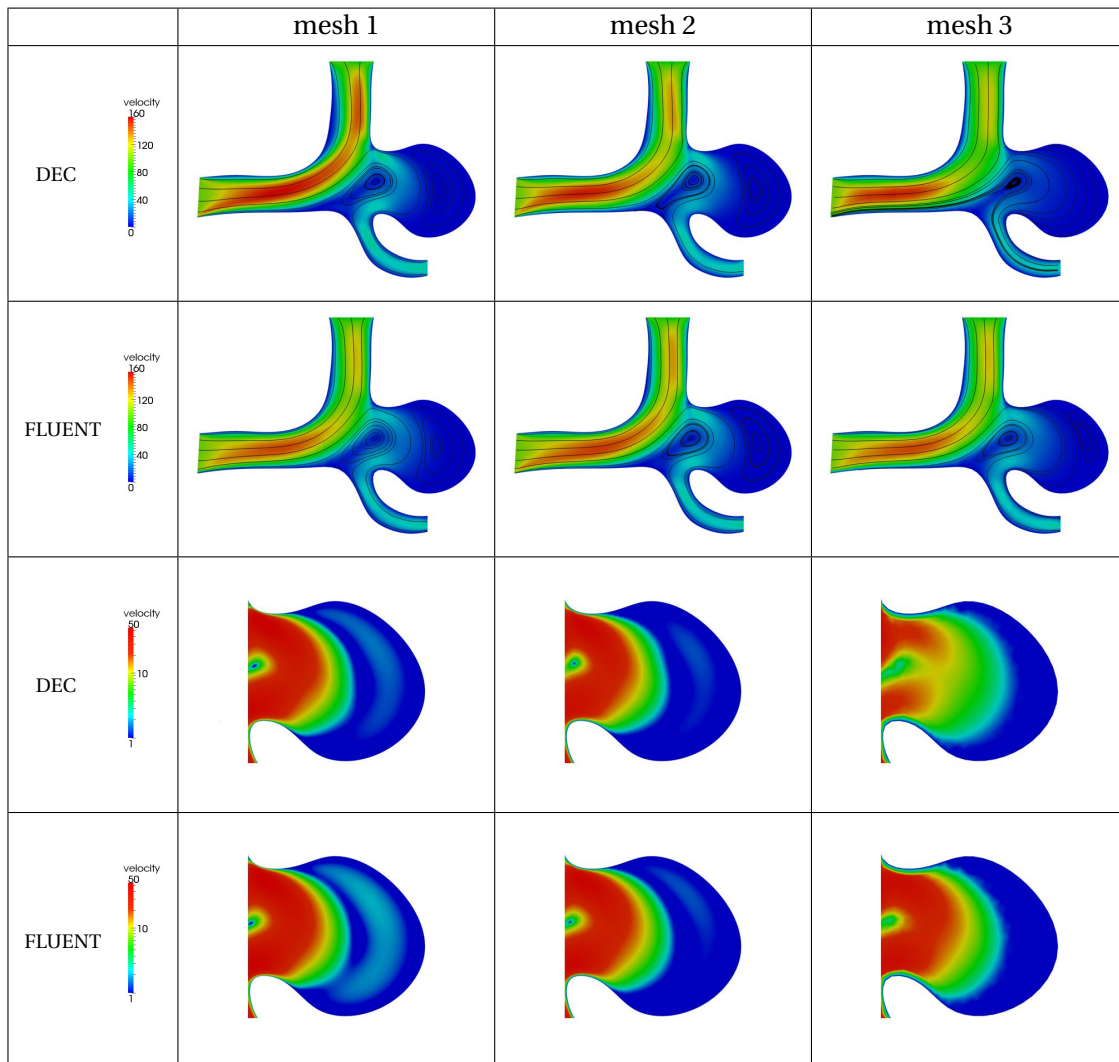


Figure 3.14: Comparison of velocity field on the large-neck aneurysm model. The contours of velocity magnitude and streamlines in the whole region and in the sac are computed by DEC and FLUENT on the identical meshes, which are mesh 1 of 210,177 triangles, mesh 2 of 19,753 triangles, and mesh 3 of only 2,160 triangles.

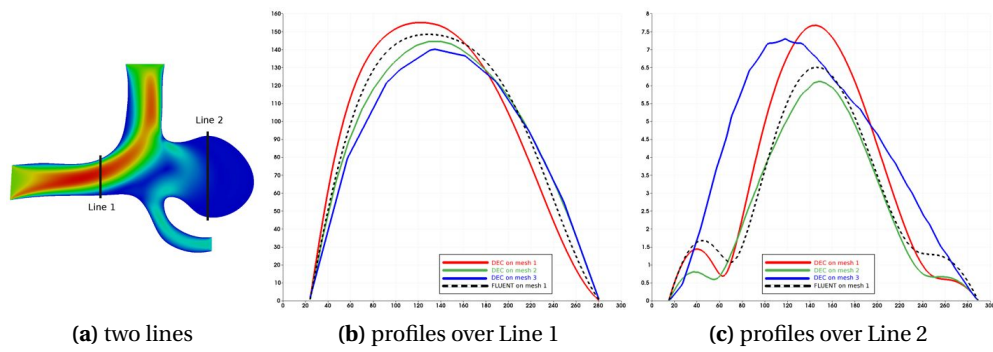


Figure 3.15: Comparison of velocity profiles on the large-neck aneurysm model.

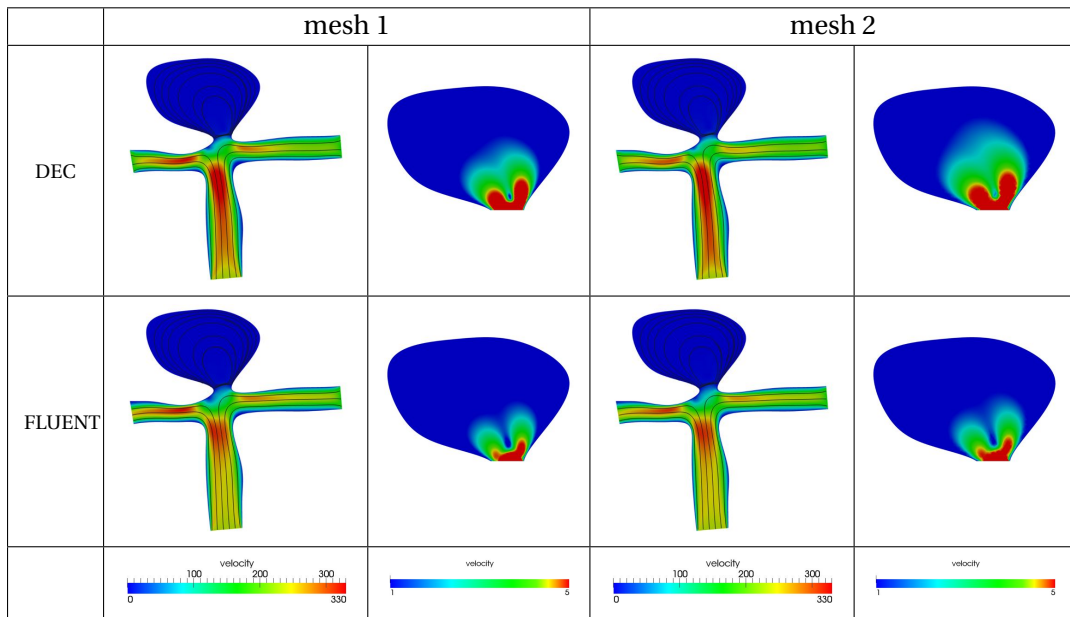


Figure 3.16: Comparison of velocity field on the small-neck aneurysm model. The contours of velocity magnitude and streamlines in the whole region and in the sac are computed by DEC and FLUENT on the identical meshes, which are mesh 1 of 35,688 triangles and mesh 2 of 8,944 triangles.

mesh	number of triangles	average edge length (mm)	CWC triangles (%)	convex dual faces (%)
mesh 1	210177	0.04682	99.95	100.00
mesh 2	19753	0.1544	99.84	100.00
mesh 3	2160	0.4626	99.58	99.83

Table 3.2: Mesh quality of the large-neck aneurysm model.

mesh	number of triangles	average edge length (mm)	CWC triangles (%)	convex dual faces (%)
mesh 1	35688	0.1522	99.97	100.00
mesh 2	8944	0.3041	99.92	100.00

Table 3.3: Mesh quality of the small-neck aneurysm model.

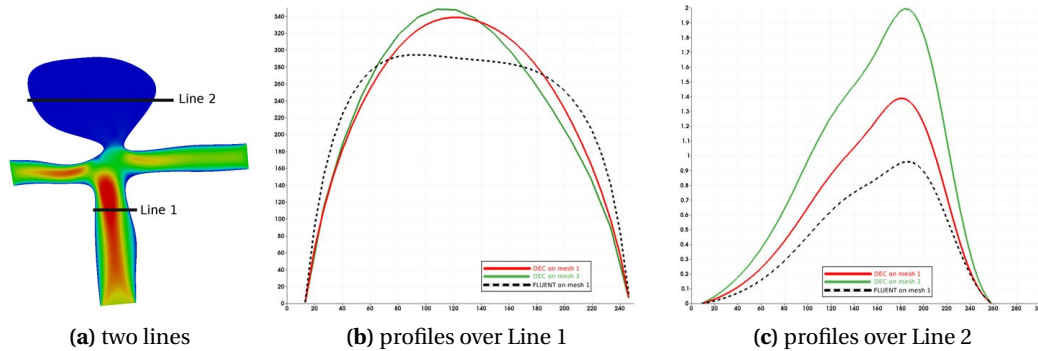


Figure 3.17: Comparison of velocity profiles on the small-neck aneurysm model.

show the similarity between the two methods. In addition, the streamlines show a strong agreement for flow patterns and vortex structures in terms of the positions of vortex centers. Only when we reduce the mesh resolution by 100 times (in the experiment of the large-neck model), the result computed by DEC loses some detail information inside the sac; less fluid flows into the sac, and the vortex inside the sac is missing.

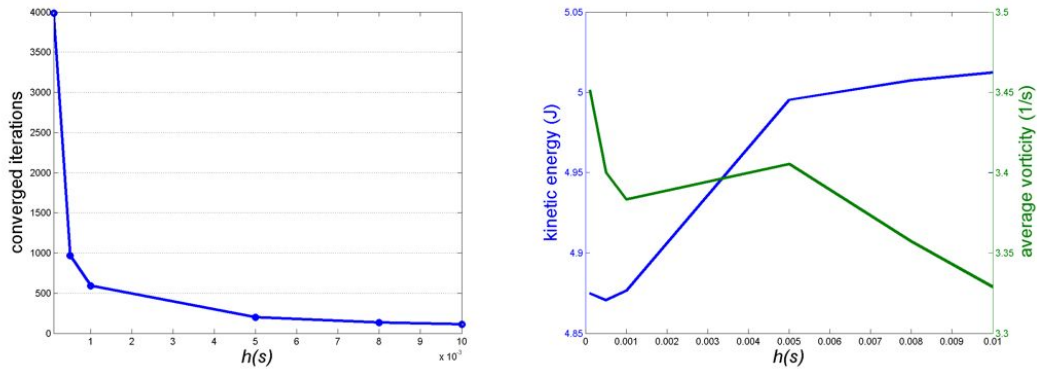
From the results of these three comparative experiments, the mesh resolution is suggested to be chosen as the average edge length is around 0.3mm , in view of the blood flow velocity near cerebral aneurysm (at the level of 100mm/s) and the diameter of intracranial vessel ($4 - 7\text{mm}$) in our experiments. For an acceptable tolerance, the simulation on such a mesh provides adequately accurate results, and can achieve faster computational time as well, since the number of the triangles in the mesh can be less than 10,000.

We use the explicit Euler scheme in the backtracking step and the identical time step (0.1ms) in all the simulations mentioned above. All of them get con-

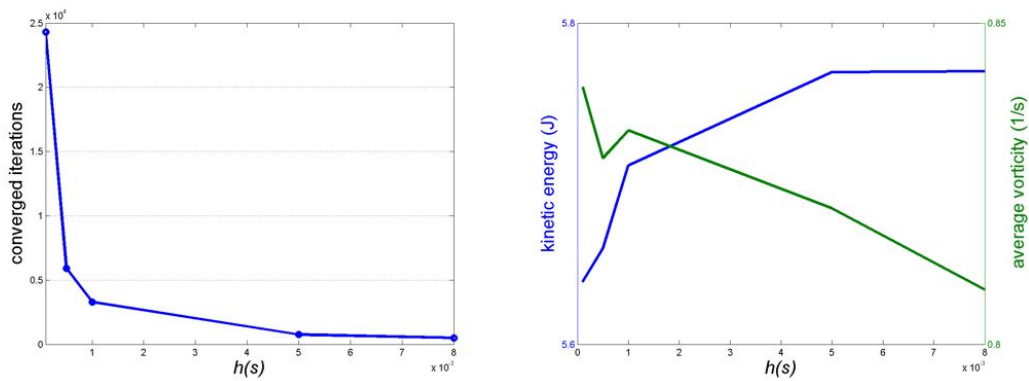
verged after a certain number of iterations using a criterion of 1×10^{-6} (which means that the relative difference of the velocity between two consequent iterations is less than 0.0001%). In the following experiment, we intend to test the impact of different backtracking schemes and different sizes of time step on the convergence of the result. For the backtracking step, we use four different schemes, the Euler scheme, the second order to the fourth order Runge-Kutta schemes (denoted EUL, RK2, RK3 and RK4 in the following). We enlarge the time step for each backtracking scheme until the simulation does not get converged any more. We pick up mesh 2 of the three geometry models to do this experiment.

In this experiment, we find out that the larger time step is used, the less iterations are needed to get a converged result. The overall trend of the average vorticity magnitude is going downward, as the time step size is inclining. This is because larger time step brings in larger numerical diffusion, The kinetic energy either gains (in the vessel model and the large-neck aneurysm model) or loses (in the small-neck aneurysm model) due to larger numerical errors caused by larger time step. The variation of these three values as the time step size increases is displayed in Figure 3.18 for each geometry model (RK3 or RK4 backtracking scheme is applied).

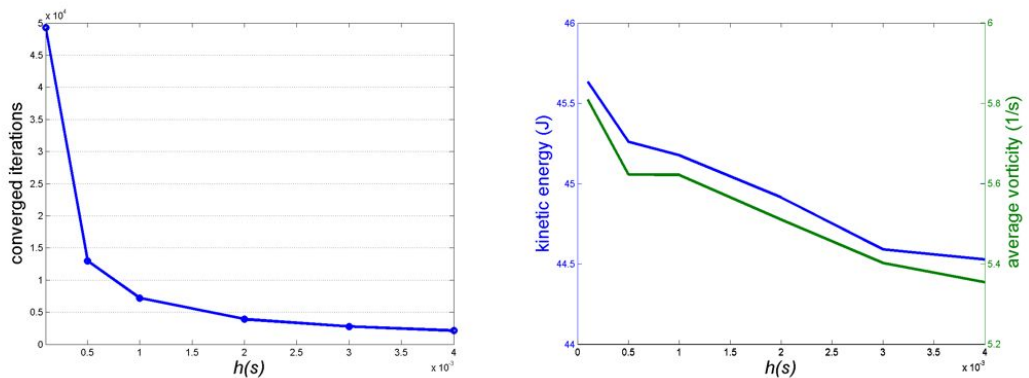
We compare the velocity contours of each model displayed in Figure 3.19, Figure 3.20 and Figure 3.21, respectively. The velocity is much slower within the aneurysm, the backtracking scheme and time step we test here have little impact on this region. As a result, we only draw the bifurcation area (and the neck area) where the relatively obvious difference is observed. From these results, we can conclude that larger time step causes more numerical diffusion. Take Figure 3.19 for example, when the time step size goes from $h = 0.1$ to $h = 5$, the gradient of velocity magnitude in space becomes smaller at the bifurcation to the bigger branch. Generally speaking, when the time step size h satisfies $v_{max} \cdot h < l$ (v_{max} is the maximum of the velocity magnitude over the whole region, l is the average edge length), the different backtracking schemes and different h values make only a little difference on the result. This means we can use EUL backtracking method to require less computational time if h is less than l/v_{max} . When the time step gets larger, more advanced backtracking schemes are required to reduce the numerical error and to make the simulation converged. Using RK3 or RK4 backtracking scheme, while the simulation is still converged, h can be increased to 5-10 times of l/v_{max} , which is 50 to 100 times larger than most of the traditional methods.



(a) the result of the vessel model (3,908 triangles)



(b) the result of the large-neck aneurysm model (19,753 triangles)



(c) the result of the small-neck aneurysm model (8,944 triangles)

Figure 3.18: The variation as the time step size increases. The number of converged iterations (the left column), kinetic energy (blue curve in the right column) and vorticity (green curve in the right column) are obtained on mesh 2 of (a) the vessel model, (b) the large-neck aneurysm model, and (c) the small-neck aneurysm model.

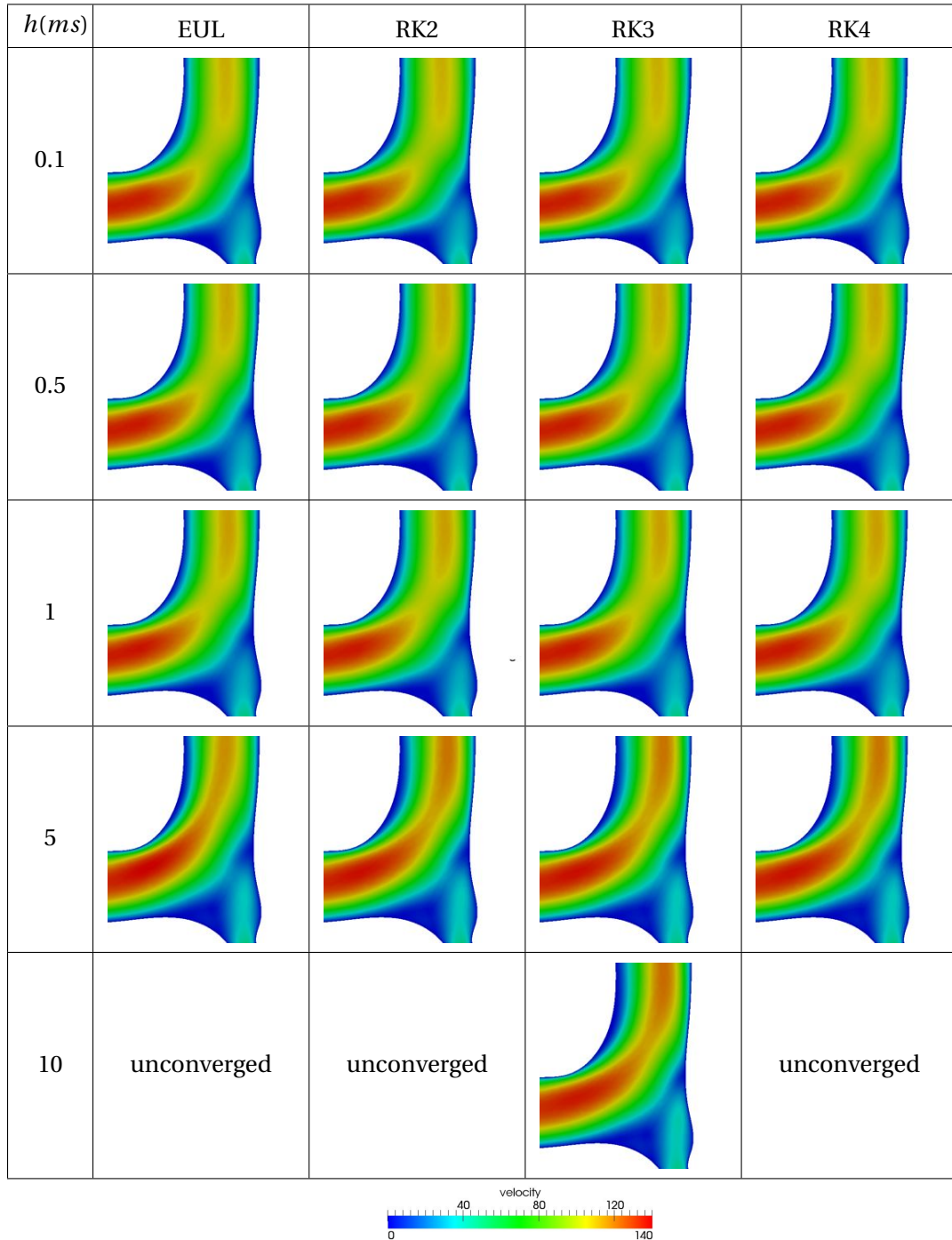


Figure 3.19: Comparison on the vessel model (the region at the bifurcation) between different backtracking schemes and different time step sizes(h).

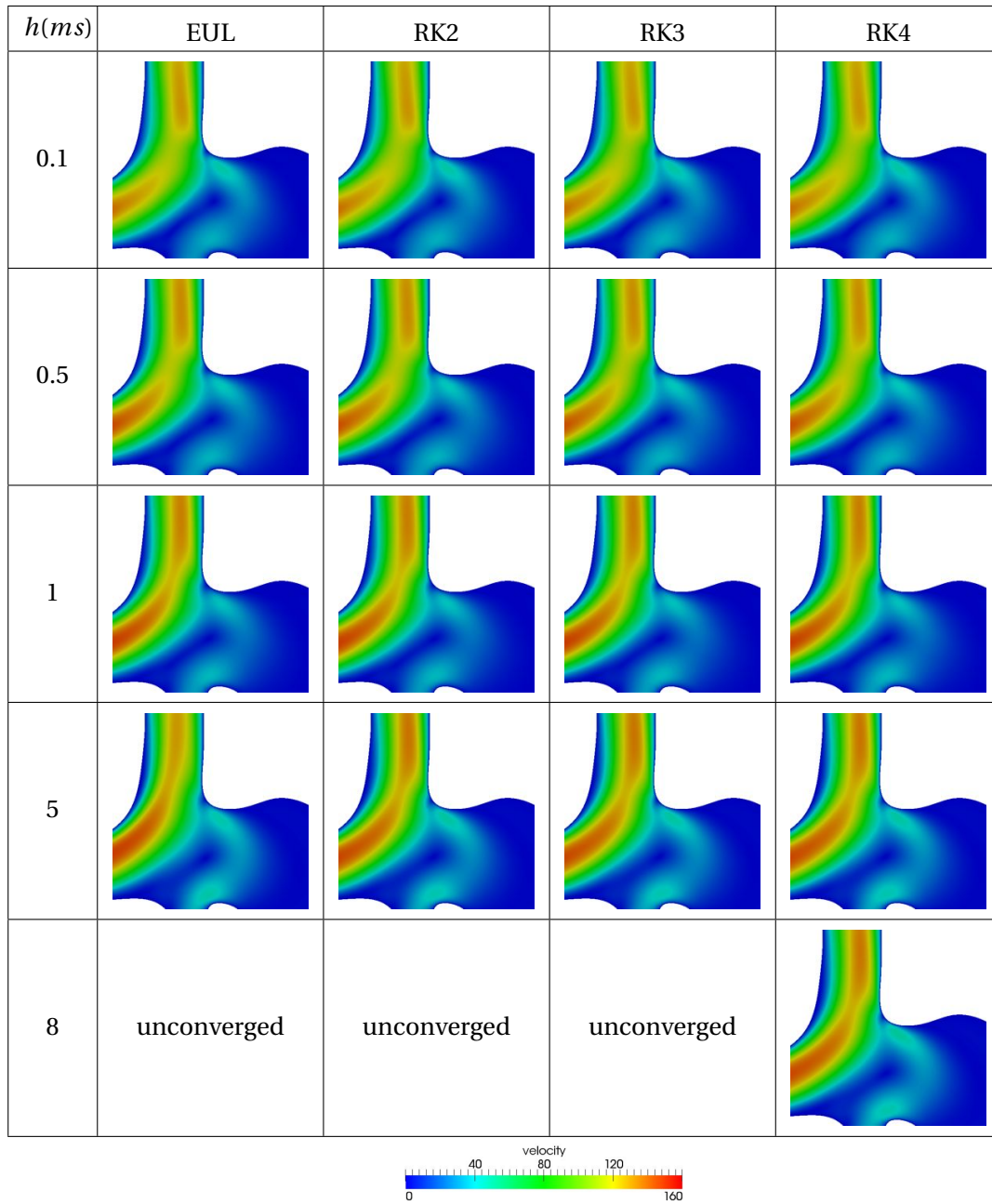


Figure 3.20: Comparison on the large-neck aneurysm model (the region at the bifurcation and the neck) between different backtracking schemes and different time step sizes(h).

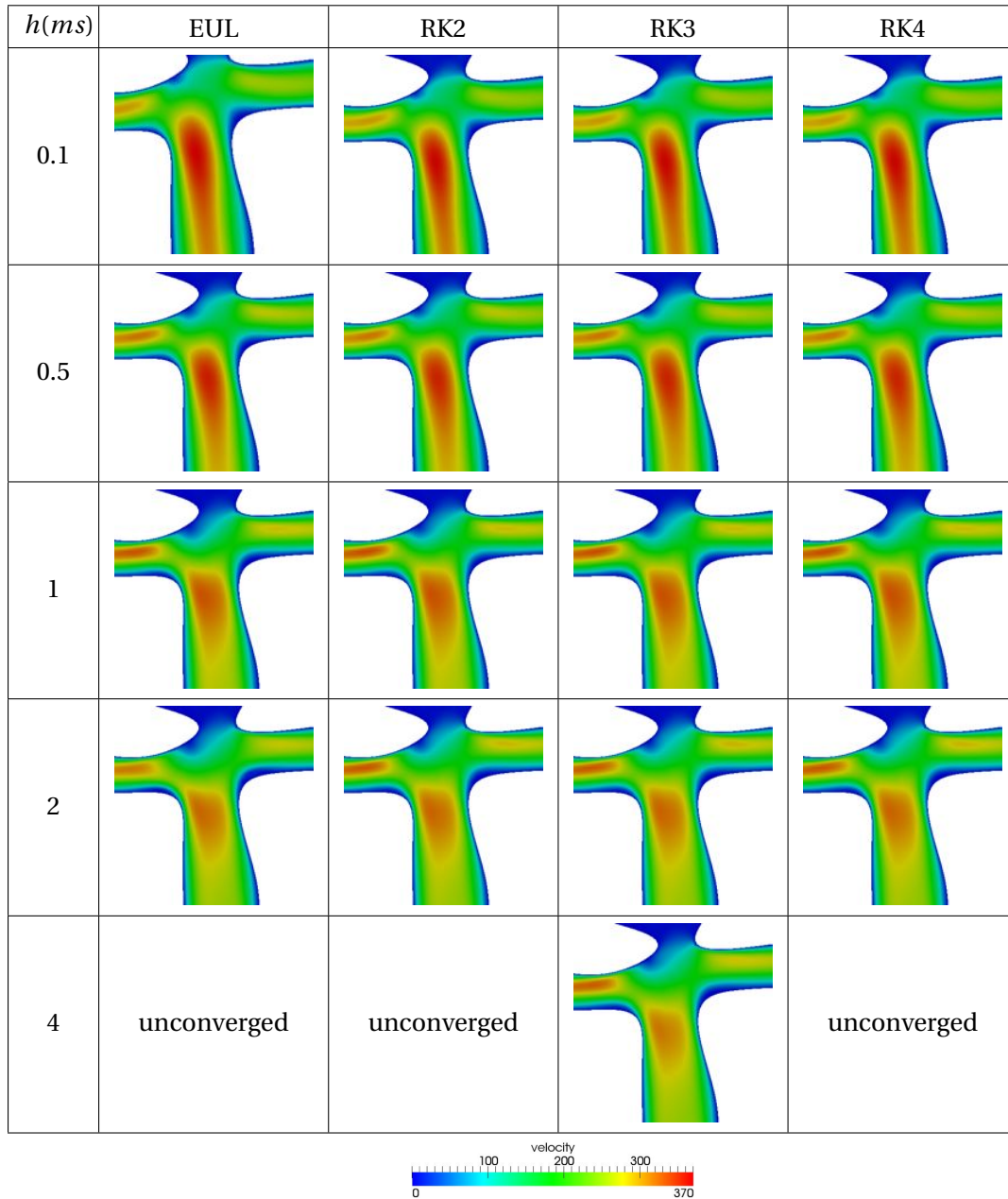


Figure 3.21: Comparison on the small-neck aneurysm model (the region at the bifurcation) between different backtracking schemes and different time step sizes(h).

mesh	number of tetrahedra	average edge length (mm)	CWC tetrahedra (%)	convex dual 3-cells (%)	negative dual edge (%)	minimum dual edge length (mm)	kinetic energy by DEC (J)	kinetic energy by FLUENT (J)
mesh 1	14612	0.5007	88.56	81.21	1.232	0.003051	1.699	1.682
mesh 2	6092	0.6680	78.73	62.79	3.158	0.02019	1.666	1.536

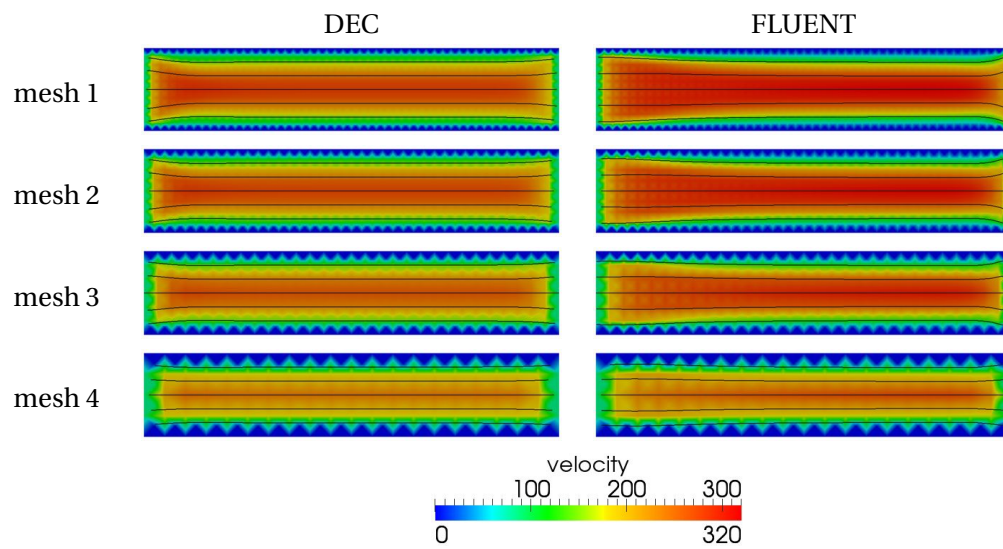
Table 3.4: Mesh quality and kinetic energy of the cylinder model.

3.5.2 Experiments of Three-Dimensional Simulation

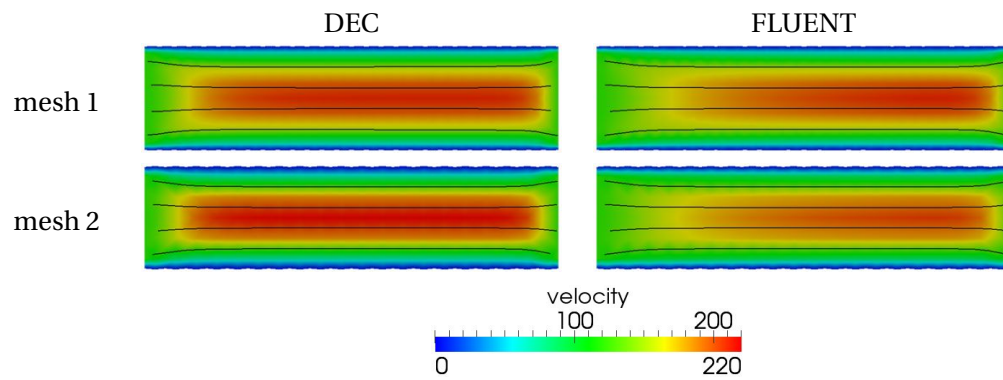
In three-dimensional experiments, we first used two simple geometries, cuboid and cylinder, to approximate straight vessel, since we can generate more regular meshes with relative high quality for such simple geometries as describe in Section 3.2. Then a patient-specific aneurysm model is considered.

We first test the method on the cuboid model displayed in Figure 3.3(b), which allows us to generate a family of absolutely high-quality meshes. In these meshes, all the tetrahedra are CWC, and dual 3-cells are convex not only for all interior primal vertices but also for all boundary primal vertices. Moreover, both tetrahedra and dual 3-cells are (nearly) regular, and the length ratio of dual edge to primal edge is over 0.3536 inside and over 0.1718 on the boundary (because of only half dual edge on the boundary face). All the tetrahedra in one mesh are exactly identical both in shape and in size, while the tetrahedra in different meshes are the same in shape but only differ in size. The resolution of four meshes we use in the experiment is presented in Figure 3.24. In the second group of three-dimensional experiments, we compromise mesh quality with a curved boundary surface. Two meshes in different resolution of a cylinder model are generated by the deformation process described in Section 3.2. However, the deformation process results in non well-centered tetrahedra, short and negative dual edges, as well as non Delaunay triangulation, which are unfavorable for DEC. Mesh quality of the two meshes we use in the experiment is summarized in the Table 3.4. There are roughly 10%~20% non CWC tetrahedra, and 20%~40% self-intersected dual 3-cells and 1%~3% negative dual edges. The ratio of minimum dual edge length to average edge length is only 0.61%~3.0%, which means some dual edges are nearly of zero length compared to primal edge. The two ends of the geometry are defined as inlet and outlet of the flow respectively.

The results computed by DEC and FLUENT on the meshes in different resolution with the same geometry are similar. Figure 3.22 displays the contours of velocity magnitude and streamlines on a slice which contains the central axis of the geometry model. Figure 3.23 shows the profiles over the line in the middle of the slice and perpendicular to the axis. Finally, we studied the relationship between mesh resolution and numerical dissipation caused by the two numerical solutions (see Figure 3.24 and Table 3.4). In Figure 3.24, the results on the cuboid



(a) the results of the cuboid model



(b) the results of the cylinder model

Figure 3.22: Comparison of velocity field on two simple geometries. The contours of the velocity magnitude and streamlines are compared on a slice, which contains the central axis of the geometry, between DEC and FLUENT on the identical meshes, whose resolution decreases from the top row to the bottom row in each sub-figure.

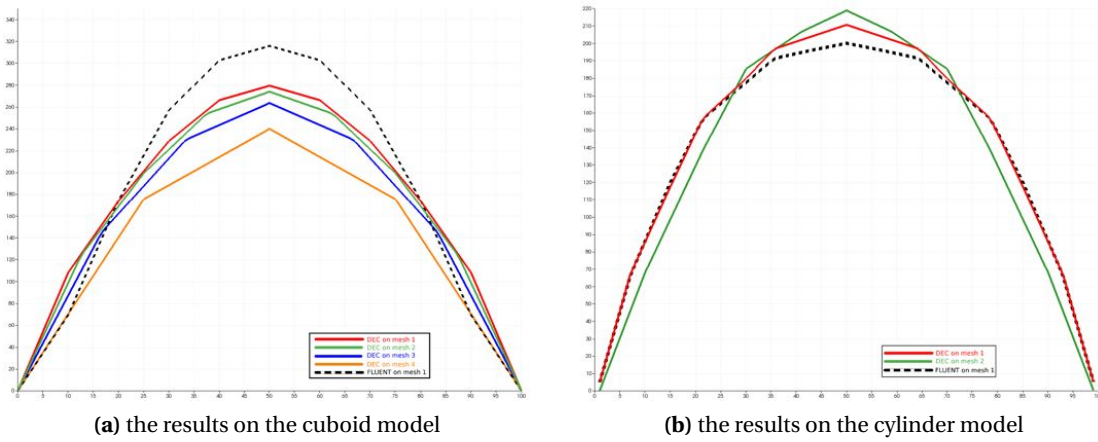
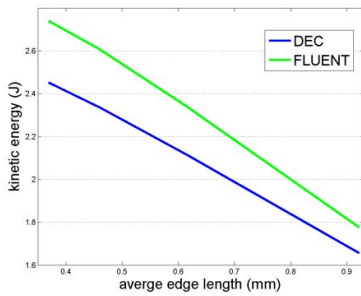


Figure 3.23: Comparison of velocity profiles on two simple geometries. The profiles of velocity magnitude are plotted over the central line which is perpendicular to the axis of the geometry. The results computed by DEC (color curves) on all the meshes are compared to the result computed by FLUENT (black dotted curve) on the finest mesh of each geometry model.

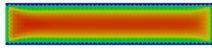
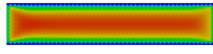
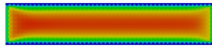
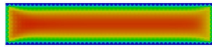
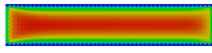
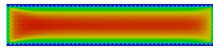
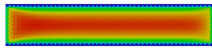
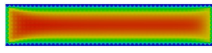
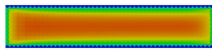


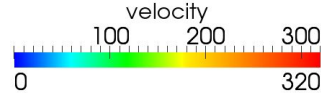
mesh	number of tetrahedra	average edge length (mm)	kinetic energy by DEC (J)	kinetic energy by FLUENT (J)
mesh 1	28000	0.3690	2.452	2.740
mesh 2	14336	0.4611	2.334	2.605
mesh 3	6048	0.6147	2.115	2.341
mesh 4	1792	0.9216	1.656	1.776

Figure 3.24: Mesh resolution and kinetic energy of the cuboid model. The kinetic energy variation as the reduction of mesh resolution is drawn on the left for both DEC (in blue) and FLUENT (in green), while the figures are given in the table on the right.

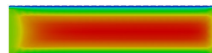
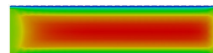
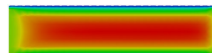
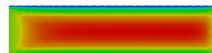
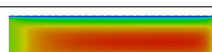
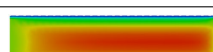
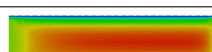
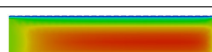
model show that kinetic energy declines nearly in a straight line as edge length increases for both DEC and FLUENT, and the declining rate of DEC is a slightly slower than FLUENT. From these two experiments on high-quality meshes, we have similar conclusion as in two dimensions: (1) the results of DEC and FLUENT are similar; (2) when the mesh resolution reduces, no more numerical dissipation is brought in by DEC compared to FLUENT; (3) all the results computed by DEC get converged after a certain number of iterations (using RK2 backtracking scheme and the time step of 0.1ms).

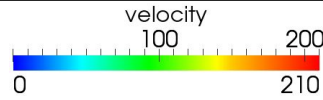
In the following experiment, we performed the simulation on mesh 1 of the two simple geometries using different backtracking schemes and larger time steps. When the time step size is less than 4ms , the velocity field get converged after a certain number of iterations, and different backtracking schemes only

$h(ms)$	EUL	RK2	RK3	RK4
0.1				
1				
4	unconverged	unconverged	unconverged	



(a) the results of the cuboid model

$h(ms)$	EUL	RK2	RK3	RK4
0.1				
1				
4	unconverged	unconverged		



(b) the results of the cylinder model

Figure 3.25: Comparison on two simple geometries between different backtracking schemes and different time step sizes (h).

have a limited impact on the converged velocity field as we compare the magnitude contours in Figure 3.25. The largest time step h we can use is 3.469 and 1.678 times l/v_{max} for the cuboid and cylinder mesh respectively. The ratio is about 50% less on the lower-quality mesh of the cylinder model compared to the absolutely high-quality mesh of the cuboid model, so we believe the DEC method is less stable on lower-quality meshes, and the instability is mainly caused by negative and tiny dual edges. As the time step gets larger, the number of necessary iterations to get a converged result declines, and the vorticity magnitude has a similar declining tendency as the two-dimensional conclusion.

In the third experiment, we use a patient-specific aneurysm model. For such a complex geometry (see Figure 3.26), it is quite challenging to generate a high-quality mesh. Using the algorithm in Section 3.2, we can obtain the meshes with over 90% CWC tetrahedra, but with only about 70% convex dual 3-cells. Additionally, the length ratio of the shortest dual edge to the average edge is less than 10^{-4} . Mesh quality of the two meshes we use for the simulation is summarized in Table 3.5.

The velocity field computed by DEC does not get converged (using the crite-

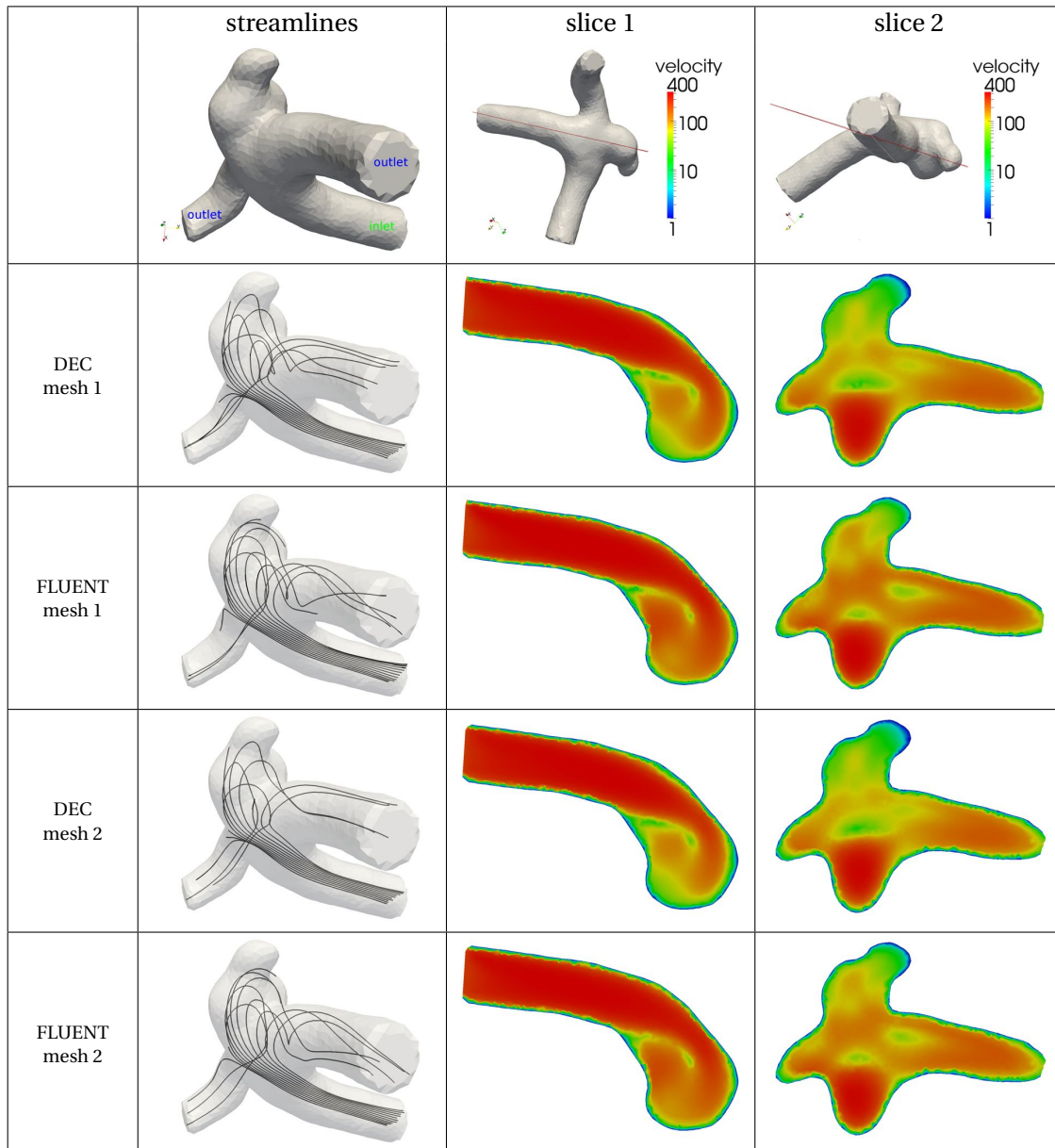


Figure 3.26: Comparison of velocity field on the patient-specific aneurysm model. The first row displays the geometry of the model and the position of two slices chosen for comparing velocity magnitude contours. In the following rows, streamlines and contours of velocity magnitude are computed by DEC and FLUENT on the identical meshes, which are mesh 1 of 55,711 tetrahedra and mesh 2 of 34,029 tetrahedra.

mesh	number of tetrahedra	average edge length (mm)	CWC tetrahedra (%)	convex dual 3-cells (%)	negative dual edge (%)	minimum dual edge length (10^{-5} mm)	kinetic energy by DEC (J)	kinetic energy by FLUENT (J)
mesh 1	55711	0.5098	91.08	70.12	0.04675	4.580	14.38	16.90
mesh 2	34029	0.5995	90.18	66.32	0.07767	5.640	14.05	15.63

Table 3.5: Mesh quality and kinetic energy of the patient-specific aneurysm model.

tion of 0.01%) even if we use much smaller time steps compared to the first two groups of three dimensional experiments. However, if the time step is smaller than $4ms$ ($3 \sim 4l/v_{max}$), the velocity magnitude only oscillate within 3%, so the result is still thought to be stable. We used this stable result to compare with the result of FLUENT. Although the mesh is very coarse compared with the two-dimensional case, similar flow structures are still captured. In Figure 3.26, the streamlines show similar blood movement. In both cases there is a low-speed region surrounded by high-speed flows observed on slice 1, which represents a local vortex in this region. There are two obvious vortices in the FLUENT result, reflected both by the low-speed regions observed on slice 2 and the swirls of streamlines, but in the DEC result on the coarser mesh, the smaller vortex is not that obvious. Moreover, in the DEC result we found less quantity of blood flows into the aneurysm sac per unit time, and the kinetic energy is lower (see Table 3.5). These results show that the DEC method can capture large-scale flow structures, while small-scale differences exist between the two approaches, which may principally stem from numerical dissipation and numerical errors caused by mesh quality.

3.5.3 Computational Time

number of the triangles	Advection term					compute vorticity	Viscous term solving diffusion equation	Recovery of velocity		
	backtrack				compute flux			compute velocity		
	EUL	RK2	RK3	RK4						
3908	3.4104	5.8749	8.1510	10.8281	0.2529	0.6887	0.7718	0.4455	0.2260	
8944	5.8894	11.1526	15.6978	21.2026	0.5178	1.5210	1.6603	0.9647	0.5013	
19753	14.1261	26.3627	37.5455	50.7205	1.3480	4.1402	4.3738	2.2069	1.1528	

(a) two dimensions

number of the tetrahedra	Advection term					compute vorticity	Viscous term solving diffusion equation	Recovery of velocity		
	backtrack				compute flux			compute velocity		
	EUL	RK2	RK3	RK4						
14612	21.7982	39.7624	57.3646	73.8814	1.5629	23.7546	25.5720	2.5636	2.5967	
28000	41.6165	74.5783	109.3307	142.3083	2.9704	46.9293	50.5692	4.8724	5.1542	
34029	99.9749	143.5345	190.2840	227.0987	5.4674	63.1981	66.5237	6.0910	6.9671	

(b) three dimensions

Table 3.6: The average computational time (ms) of each step in the DEC algorithm.

We measured the average computational time of each step in one iteration of the DEC algorithm for both two- and three-dimensional simulations on an

number of the triangles	FPS				
	EUL	RK2	RK3	RK4	FLUENT
3908	172.5385	121.0974	95.2859	75.8303	50.0
8944	87.7367	60.1842	47.9303	37.4054	5.0
19753	36.5648	25.1037	19.6370	15.6082	9.1

(a) two dimensions

number of the tetrahedra	FPS				
	EUL	RK2	RK3	RK4	FLUENT
14612	172.5385	121.0974	95.2859	75.8303	/
28000	87.7367	60.1842	47.9303	37.4054	/
34029	36.5648	25.1037	19.6370	15.6082	2.0

(b) three dimensions

Table 3.7: The average FPS of DEC using different backtracking schemes and FLUENT.

Intel 3.0GHz processor (see Table 3.6). The backtracking step is the most time-consuming, and obviously more advanced backtracking schemes require even more computational time. This step takes about half computational time while solving the two linear systems roughly takes the other half. Table 3.7 gives the frames computed per second (FPS) by DEC when using different backtracking schemes, and by FLUENT. The results of DEC and FLUENT are obtained on an Intel 3.00GHz processor and an Intel 2.40GHz processor, respectively. The processors are different, but still comparable; the big difference in FPS between DEC and FLUENT is not mainly attributed to the processors. When using DEC and the largest time step mentioned above, the simulation time of 1s requires 1.0495s, 5.2159s and 8.0086s on average to compute on a mesh of respectively 3,908, 8,944 and 19,753 triangles in two dimensions. And in three dimensions, we need 32.48s, 63.20s, 93.84s to simulate the real time of 1s by DEC on the meshes of 14,612, 28,000, and 34,029 tetrahedra respectively. On the other hand, the simulation process of FLUENT was observed between 40 and 250 times slower than DEC in our experiments. Not only because FLUENT takes longer time to compute each iteration, but also the time step FLUENT uses should be significantly smaller. FLUENT does not explicitly provide the time step size it uses in these experiments. Nevertheless, according to the Courant Friedrichs Lewy (CFL) condition, a necessary condition for convergence while solving hyperbolic partial differential equations, the time step h should be less than $C \cdot \Delta x / v$, where Δx is length interval, v is the velocity, and C is CFL constant (typically C equals to 0.1 for solving Navier-Stokes equations). If we use the average length and maximum velocity to approximately estimate h , then we have $h < 0.1 \cdot l / v_{max}$. Compared to DEC, h can be $3 \sim 10 \cdot l / v_{max}$, which is $30 \sim 100$ times larger. Take the aneurysm model with 34,029 tetrahedra for example, FLUENT

requires 4170s, nearly 44 times more than DEC, to simulate the real time of 1s.

Finally, It is also worth of mentioning that the processors used in these experiments are quite standard. When using recent high-end processor, the computational time can be reduced by as much as 50%. For example, the computational time of 93.84s on the patient-specific aneurysm in three dimensions can be reduced to 44s on an Intel i7 3.33GHz processor.

3.6 Discussion

From the results of the previous section, we have identified two main limitations of our current method: the impact of mesh quality and the computational time.

3.6.1 Mesh Quality

We notice that mesh quality has a significant impact on the DEC approach in the aspects of convergence and accuracy. These issues of mesh quality were either not mentioned or underestimated by Elcott [Elcott et al. (2007)], who initially employed the DEC theory for numerically solving the Navier-Stokes Equations. Since their objective was to simulate the fluid motion for appealing visual effects, convergence and accuracy of the solution were not their main concerns. Besides, although they aimed at fast computation, to generate a video of fluid flow in tens of minutes was still acceptable for them. (They reported the computational time of 0.47s per frame on a mesh of 32K tetrahedra using a Pentium 4.3GHz processor, compared to our result of 0.25s – 0.41s per frame on a mesh of 34K tetrahedra using an Intel 3.0GHz processor.) But in our case, interactive medical simulation highly depends on real-time computation, as well as more reliable results. So we have payed a great attention to what may affect the stability and accuracy of this new method, and find that low mesh quality is one of the most important factors when we simulate the fluid on three-dimensional meshes. Actually, the criterion of defining high or low mesh quality for the DEC method is not clear yet, and has not been stated in any literature as far as we know. Although we measure mesh quality by CWC percentage, tiny dual edge, etc., there is no quantitative relationship between these measurements and the stability or accuracy of simulated results. At present, defining and generating high-quality tetrahedral mesh for complex patient-specific geometry is the main restriction for us to further improve the results.

In some three-dimensional cases, Delaunay tetrahedral mesh cannot be achieved by the interleaved optimization algorithm, and it results in the self-intersected dual 3-cells. Additionally, the mesh contains some extremely irregular elements (e.g., flat tetrahedron, tiny dual edge, small dual face deviated from the primal edge's position in Figure 3.6). As a consequence, the results only re-

main in stable, but cannot get converged even when we use much smaller time steps. Moreover, the difference of velocity field computed by DEC and FLU-ENT shown in Figure 3.26 is more obvious than what we observe in the two-dimensional cases, for which high-quality meshes can be computed using state-of-the-art mesh optimization techniques (such as the centroidal voronoi tessellation, Lloyd in the CGAL library [CGAL]). Generally speaking, the low-quality mesh causes several problems for the DEC approach: (1) the flat tetrahedra may create a dual face which does not intersect with its primal edge, so the transfer of physical quantities between dual 2-form and primal 1-form has a deviation caused by the position offset; (2) tiny dual edges or faces make some diagonal elements of \star_2 or \star_1 matrix near zero, thus have an influence on the accuracy of the discretization and the stability of the linear system; (3) self-intersected dual 3-cells bring errors in the interpolation step. Even higher resolution of the mesh does not improve mesh quality any more by our meshing algorithm, and we do not observe any obvious improvement in the simulation results when we use the mesh with higher resolution but similar quality.

In our numerical method, the linear system is mainly based on the Laplace operators, which are expressed by the basic derivative operators d and Hodge operators \star . The d operators only rely on mesh topology, thus are exact expressions. The loss of accuracy and the cause of instability only rise from the discretization of the \star operators, which relates to mesh geometry. A controlled experiment can be designed to further quantify the impact of mesh quality on the DEC method. We need to create a series of meshes with the same boundary and topology, but different geometrical positions of the interior vertices. Thus the d operators are the same for these meshes, while the \star operators have different diagonal values. Then we solve a problem which has analytical solution, and measure the error of results obtained on these meshes compared to the analytical solution. Furthermore, the condition number of the Laplace operator can be used as a measurement of the stability of the system. At present, we have developed an interactive tool to manually move the interior vertices in two dimensions while maintaining the same topology and Delaunay triangulation, and will continue to work on this controlled experiment in the near future.

As to improve the precision of the \star operators, we can either use higher-order discretization of \star operators or optimize the primal mesh and/or dual mesh by minimizing the numerical error of discrete \star operators. The former solution not only increases the difficulty to compute the operators during the initialization step, but also decreases the sparsity of the \star operators and Laplace operators, thus make inversion of the matrices more difficult and decrease the computational efficiency. In order to keep in line with our objective of real-time simulation, we prefer the latter option. Generation of the primal and dual meshes should only be done once before the simulation, and adds no extra

cost to each iteration during the simulation, unless a great refinement of the mesh has been performed, and increases the system size. Most previous work usually chooses barycentric or circumcentric duals; barycentric duals are preferred due to the CWC property (the barycenter is always inside the simplex), while circumcentric duals guarantee the induced orthogonality between primal and dual elements. In the fluid simulation, the orthogonality is highly recommended for the purpose of describing physical quantities. As a result, Delaunay/Voronoi duality is commonly employed in lots of work, as well as our method. However, we found that circumcentric dual vertices can be moved to new positions in order to achieve more regular dual cells (e.g., make the relatively short dual edge longer) while keeping primal-dual orthogonality. The regular triangulation and power diagram (also called weighted Delaunay triangulation and weighted Voronoi diagram) [Glickenstein (2005)] provide such a duality we desire. The i^{th} weighted point is defined as a pair (\mathbf{x}_i, w_i) , where \mathbf{x}_i is the position of the point, and w_i is the weight. The weighted Voronoi region, $V_i = \{\mathbf{x} \in \mathbb{R}^n \mid \|\mathbf{x} - \mathbf{x}_i\| - w_i \leq \|\mathbf{x} - \mathbf{x}_j\| - w_j, \forall j\}$, is the dual of the i^{th} point. The dual vertices of the primal simplices are called weighted circumcenters. The dual edge linking incident dual vertices is perpendicular to its primal edge/triangle. When the weights on all points are equal, regular/power pairs degenerate to Delaunay/Voronoi pairs. Except for computing the \star operators using weighted circumcenters instead of circumcenters, other steps of our method can be directly applied. From the same primal triangular/tetrahedral mesh, we have a flexibility to choose different dual mesh by just tuning the weights. And the key problem is how to properly set the weights.

Only recently, a paper addressing the problem of optimizing triangular/tetrahedral mesh presented a similar idea and could improve the accuracy of the DEC method. Mullen proposed energy functions to estimate the error induced by diagonal Hodge stars, and concluded that the minimizers of these functions, called Hodge-Optimized Triangulation (HOT) meshes, provided increased accuracy and flexibility for a variety of computational purposes [Mullen et al. (2011)]. They updated the mesh in each iteration by optimizing both the positions and weights of vertices. We followed their idea to implement only the weight optimization, because the position optimization, involving recomputing the primal Delaunay triangulation, is more complicated to implement. Our preliminary two-dimensional result in Figure 3.27 shows that the optimization of weights $\{w_i\}$ (even with no optimization of the points $\{\mathbf{x}_i\}$) can improve mesh quality; as it makes the relatively short dual edge longer. The interleaved position optimization and weight optimization, as well as further investigation in three dimensions is our work in the next step. Besides, we are also considering to modify the HOT algorithm to deal with the mesh which (nearly) does not meet the Delaunay criteria. Take the mesh in Figure 3.27(a) for example, the short

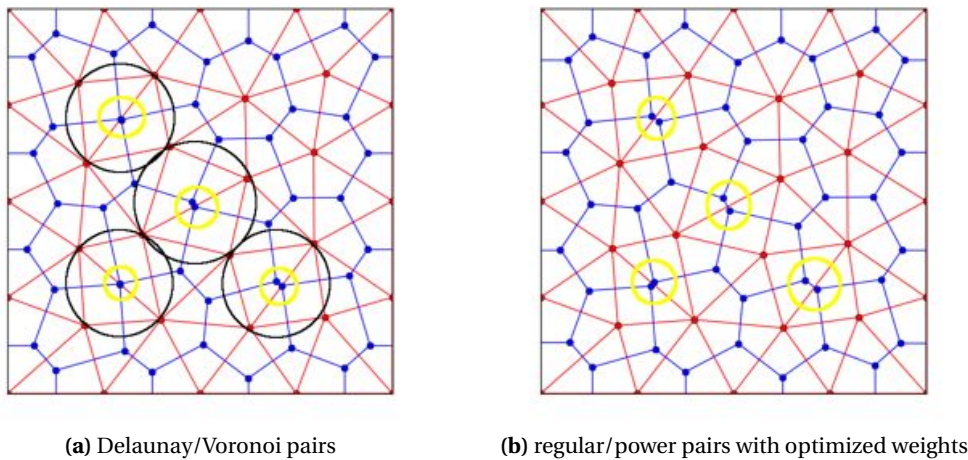


Figure 3.27: Hodge-Optimized Triangulation (HOT). (a) We create a primal mesh whose Voronoi dual mesh contains several artificial short dual edges, and use zero weights (Delaunay/Voronoi pairs) as the initial state. (b) After optimization of the weights by HOT algorithm, the optimized regular/power pairs are more favorable for the DEC approach, as the short dual edges get longer.

dual edges are associated to the fact that there are four points almost locate on the same circle. In the meantime of minimizing the energy function, extra constraints on the weights of these four points can be added, then the constrained optimization method is applied to compute the optimized weights under certain conditions.

Besides the improvement of mesh quality, the DEC method could be made more robust to complex geometries. For example, other interpolation applicable to the sets which are not convex should be investigated in the case of non convex dual cells. Furthermore, the immersed boundary method (IBM) can be considered to combined with the DEC method, so the absolutely high-quality regular mesh containing the fluid region but not conforming to the exact boundary can be used.

3.6.2 Computational Efficiency

For most of the three-dimensional cases in our experiments, the simulation is only near real-time. We want to more deeply investigate various computational strategies to obtain real-time computation by using more advanced numerical schemes.

Firstly, the backtracking step, accounting for nearly half of the total computational time, is the most time-consuming step. In this step, each dual vertex of the mesh is traced backwards using the velocity field defined on the dual vertices of the current time step. The reason why it is computationally expensive is that the

interpolation of the velocity at a backtracked point requires to locate this point in the mesh in order to find a set of neighbor samples (dual vertices). The higher-order backtracking scheme we use, the higher-frequency interpolation we need to trace one point. For instance, the EUL scheme interpolates once per point, while the RK2 scheme interpolates twice per point. Nevertheless, the computation of backtracking each dual vertex is independent of the others, thus can be performed at the same time. Moreover, it only depends on topological neighbors, which benefits the parallel implementation on GPU. Take the aneurysm mesh of 34,029 tetrahedra for example, the GPU implementation can possibly reduce the computational time by 35 to 45 times [Comas et al. (2008)].

Secondly, solving the two linear equations take nearly the other half computational time. The preconditioning technique coupled with a GPU-based conjugate gradient implementation [Courtecuisse et al. (2011)] can be used for this step to provide significant acceleration of the simulation process. For a system over the size of 30K, it can speed up by 6.7 times.

Finally, adaptive refinement techniques for generating multi-resolution mesh [Prakash and Ethier (2001)] are worth of considering. These techniques are able to automatically subdivide the mesh elements only where the predicted solution error is the greatest. A certain iterations of the subdivision result in a mesh that is highly resolved only where it is needed, thus maximizing the solution accuracy while minimizing the computational effort.

THE SIMULATION OF BLOOD-STRUCTURE INTERACTION

With the success in the area of hemodynamics, more and more physics-based methods have been introduced to the aneurysm related researches. In the previous chapter, we only simulate the fluid motion, but ignore the influence of other objects which interact with the fluid, such as surgical instruments and blood vessels. In this chapter, we consider the complicated physical and physiological processes encountered in the area of aneurysmal hemodynamics, involving the interactions between blood and coils during aneurysm embolization, and the interaction between blood and vessels during aneurysm development. In Section 4.1, we first provide a concise background of fluid-structure interaction modeling in the general context, then introduce two applications in medical simulation, aneurysm coil embolization and aneurysm growth. Our methods to simulate blood-coil interaction and blood-vessel interaction for these two medical applications are presented in Section 4.2 and Section 4.3 respectively. Finally, perspectives on clinical use of these simulation methods are discussed in Section 4.4.

4.1 Introduction

In this section, we provide the background for solving fluid-structure interaction problems, and review some applications in physiological phenomena, specifically during the procedure of aneurysm coil embolization and the process of aneurysm growth.

4.1.1 Fluid-Structure Interaction

The numerical solution to Fluid-Structure Interaction (FSI) problem poses great challenges since it involves computing fluid dynamics and structure mechanics, as well as modeling their interactions and handling the interface. A straight-

forward strategy is to separate the domain into fluid and solid subdomains. In each subdomain, solution is obtained independently, and the interaction between fluid and solid is considered as external boundary conditions. This strategy, named loosely coupled approach, has the advantage that many well developed numerical solutions can be used directly in each independent system. But the interface and interaction between two systems require to be treated carefully because of high stiffness and sensitivity. In contrast, fully coupled approach, treating the fluid and solid as a single continuum, is more proper for large deformations of fluid and solid domains. A comparison of the most important FSI coupling strategies in the context of biomechanical problems was made by Küttler [Küttler et al. (2010)].

Usually, the fluid or solid motion can be described in Eulerian formulation, or Lagrangian formulation, or their combination, i.e., Arbitrary Lagrangian-Eulerian (ALE) formulation. These three descriptions differ in reference mesh. Eulerian method, mainly used in fluid dynamics, uses a fixed reference mesh, where the object moves. This method usually does not need remeshing operations even when handling large distortions of the object, but generally at the expense of the definition of precise interface and the resolution of flow details along the moving boundary. Lagrangian method, widely used in structural mechanics, uses a moving reference mesh, each node of which is moving with the associated material during motion. This method allows easy tracking of free surfaces and boundaries of materials, but is unable to follow large deformations of the computational domain without frequently remeshing. ALE has been developed with the purpose of combining advantages of the two methods, while minimizing their respective drawbacks as far as possible. ALE method uses a reference mesh with freedom, the nodes of which may be moved with the material as Lagrangian manner, or be fixed as Eulerian fashion, or be moved in an arbitrarily specified way. Thus, it can handle with greater deformations of the object than purely Lagrangian method, and is more favorable for dealing with the moving interface than purely Eulerian method.

An important technique in FSI approach is to describe the moving interface. Using the Lagrangian formulation is a boundary fitting strategy; the boundary of the mesh is moving with the material, and always conforms to the updated material shape. It is one of the most widely used methods because of its simple implementation, low computational cost and accuracy to track the moving interface. However, frequent remeshing is necessary to get accurate solution on the mesh when large deformation happens, and this process could be very troublesome and time consuming. Once the remeshing process takes place, the transfer of variables from the old mesh to the new mesh is also required, which is also tricky, costs extra computational time, and may cause artificial effects, resulting in loss of the accuracy of variables.

On the other hand, another different strategy, non boundary fitting method, does not use such an exact and direct description to handle the interface. One of the most well-known methods in this category is Immersed Boundary Method (IBM), firstly proposed by Peskin [Peskin (1972)]. The original method carried out the entire simulation on the fixed finite difference grid which did not conform to the geometry of fluid domain. But a set of immersed points was used to define the interface. This immersed solid boundary interacted with the fluid by applying local body forces. Then lots of followers further developed this method by introducing these body forces differently for various problems. Another similar method, fictitious domain method [Glowinski et al. (1997)], based on the finite element framework, established fluid-solid coupling by constraining the fluid and rigid body at their interface using a (distributed) Lagrange multiplier and extending this constraint to the inner body. Generally speaking, while these non boundary fitting methods take the advantage of Eulerian manner, they sacrifice certain accuracy of the solution near the interface due to interpolation errors. A more deep comparison of these boundary handling methods for deformable bodies was made by Van Loon [Van Loon et al. (2007)]. These methods can be combined with each others to minimize their own drawbacks, see [Van Loon et al. (2004)] as an example.

The fluid simulation with rigid boundaries sometimes fails to predict essential characteristics of the physiological flow (such as pressure wave propagation on the vessel), and is unable to provide interactions with other structures. Therefore, FSI method is a useful tool for understanding the causes of diseases in human circulatory system and respiratory system, evaluating new surgery techniques, and providing surgical planning. For example, Immersed Boundary Method was originally introduced to study flow patterns around heart valves [Peskin (1972)]. Actually, the main propelling force to develop this field is the increasing demand from medical community for scientifically rigorous and quantitative investigations of cardiovascular and respiratory diseases. As a result, lots of physiological phenomena were studied, such as the function of cardiac and venous valves [Van Loon et al. (2004)], pulse wave propagation in the arteries [van de Vosse and Stergiopoulos (2011)], flow in the microcirculation [Popel and Johnson (2005)], pulmonary airway closure and reopening, phonation and snoring [Grotberg and Jensen (2004)]. In the following two sections, we will review two FSI problems related to the aneurysm disease.

4.1.2 Aneurysm Coil Embolization

Over the last decade, remarkable progress has been made in the field of endovascular treatment, which uses the vascular network to carry a micro-catheter to the diseased part in human body. Technological advances continue to make it

possible for a growing number of patients with cerebral aneurysms to be treated with a variety of endovascular strategies, essentially coiling. Detachable coil embolization is a recent interventional technique for treating aneurysms and other blood vessel malformations in the brain and other parts of the body. The coils are made of soft platinum wire in different diameters (smaller than a strand of hair) and lengths. The physician places several coils through the catheter into the aneurysm. The presence of coils reduces blood flow and wall pressure within the aneurysm, thus creating a favorable hemodynamic environment for thrombus embolization. The formation of blood clot around the coil blocks off the aneurysm, thus considerably reducing the risk of rupture. Although coil embolization is less invasive than open surgery, it remains a very complex medical procedure, which is very difficult to perform and requires careful planning and a long experience to minimize the risks for patient. Yet, even in the case of a successfully performed procedure, the choice of coil (shape, length, diameter) plays a key role in the long-term success of the procedure.

In this context, the development of training and planning systems can help decrease the risk of errors, in particular during the learning curve of the physician, or when dealing with complex, rare pathologies [Gould (2007)]. However, the computer aided system, allowing interventional radiologists to select different coils and test their behavior in a patient-specific environment, requires not only to model the behavior of a coil in patient-specific aneurysm model, but also to compute the interaction between coil(s) and the complex flow occurring within aneurysm.

Although the hemodynamics of aneurysms before the procedure of coil embolization have been extensively studied, a few studies have focused on aneurysm-related hemodynamics after endovascular coil embolization. Some follow-up studies were made by clinical review with angiographic performed post-treatment [Byrne et al. (1999)]. Boecher-Schwarz et al. investigated the physical effect of coils on pressure and flow dynamics in aneurysms by an ex-vivo study on aneurysms created in rabbits and then exposed to pulsatile flow before and after coil embolization [Boecher-Schwarz et al. (2000)]. By experimental approach, Canton et al. measured the changes in blood pressure of the aneurysm and flow characteristics of the parent vessel resulting from packing the aneurysm sac with hydrogel-coated coils [Canton et al. (2005)].

Besides these studies based on clinical review and experiments, Groden et al. evaluated the impact of different levels of coil packing on the flow and wall pressure in the aneurysm sac and parent vessels by solving the Navier-Stokes equations [Groden et al. (2001)]. The filling of the aneurysm with platinum coils was simulated by a set of randomly distributed blocked cells. They concluded that the inserted platinum coils occupying up to 20% volume of the aneurysm sac immediately and decisively relieved the influx of pulsating blood and al-

lowed for initial clotting. However, their conclusion was based on a simple and idealized geometrical model, but not an actual aneurysm model. Kakalis et al. employed patient-specific geometrical model to get more realistic flow patterns, and modeled the coiled part, from a static point of view, as a porous medium [Kakalis et al. (2008)]. They reported that inserted coils rapidly changed the flow patterns in aneurysm and caused reduction in mural pressure and blood velocity, providing favorable conditions for the thrombus formation and obliteration of aneurysm. But their simulation was relied on the commercial software, and was not aimed at real-time simulation for interactively surgery planning. Besides, Morales et al. carried out the CFD analyses in patient-specific aneurysm geometries both before and after treatment for evaluating the relative effect of coil configuration on local hemodynamics [Morales et al. (2011)]. Schirmer and Malek modeled hemodynamics in the aneurysm treated with helical coils to investigate the influence of framing coil orientation on the embolization outcome [Schirmer and Malek (2010)]. In order to evaluate the long-term aneurysm occlusion outcome after coil embolization, Cha et al. used a semiheuristic porous medium set of equations to describe the aneurysm flow, plus the Navier-Stokes equations to govern the dynamics of the flow around the aneurysm [Cha et al. (2007)]. They estimated the total force on the overall mass of coils to predict coil compaction in long term. All of these studies based on computational approach relied on commercial software or traditional numerical techniques, and the computational times (dozens of hours in general) were incompatible with interactive simulation or even clinical practice. Besides, most of them (except [Cha et al. (2007)]) only considered the influence of coil(s) on the blood flow after coil(s) being placed into the aneurysm, but the reverse influence of blood flow on coil has not been studied yet. Cha et al. studied the reverse effect but only computed the total force applied on the coils in the global view to predict long-term outcome [Cha et al. (2007)].

As for simulating coil motion, Dequidt et al. proposed an original model to obtain interactive and accurate simulations of coil deployment [Dequidt et al. (2008)]. The model took geometric nonlinearities into account and used a shape memory formulation to describe its complex geometry. But they did not include the influence of the blood flow onto the coil. We followed this work to compute the coil behavior in the blood flow within and around the aneurysm [Wei et al. (2009)]. Finally, previous work in the area of real-time simulation of interventional radiology procedures has mainly focused on training rather planning (besides the work of [Dequidt et al. (2008)]), and has been limited to the simulation of flexible devices (see [Alderliesten et al. (2004)], or [Duriez et al. (2006)] for instance).

In our work, we add extra terms to the Navier-Stokes equations to describe the impact of inserted coil(s) on the blood flow, requiring little additional com-

putational cost compared to the pure fluid simulation in the previous chapter. On the other hand, we also considered the reciprocal effect, i.e., the impact of the flow onto the coil, during the procedure of coil embolization. Our simulated results demonstrated that the reverse effect ignored by previous works is essential in the context of planning the coil embolization surgery. More importantly, the results showed that our approach permits real-time simulation of the interaction between coils and blood flow during coil embolization.

4.1.3 Aneurysm Growth

Several theories were proposed regarding the causes of aneurysm formation, growth and rupture, but with few clear results. There are two relatively separate processes in aneurysm development. The first relates to the initial stage of aneurysm formation. Current researches believed that aneurysm initially resulted from congenital diseases, together with some possible additional factors such as injuries to the arterial walls which effect blood circulation, or deficiency in collagen or elastin which alters the elastic properties of arterial wall. While the exact causes for the creation of aneurysm remain unclear, the second process of the expansion and possible rupture of aneurysm has received more focus and remains a somewhat easier problem to address.

Blood flow dynamics is thought to be one of the primary causes of aneurysm development, along with arterial wall elasticity and stress. In addition, it is also the influence of time that leads to the development and rupture of aneurysm. Actually, it is particularly complicated to incorporate wall compliance into the vascular CFD models, because it requires knowledge about the distribution of wall thickness and elasticity, and intra-arterial pressure waveform. Moreover, the coupling between blood and vascular tissue is highly nonlinear due to the fact that the ratio between the densities of blood and tissue is roughly equal to one, which makes the structure is relatively sensitive to the small variations of interaction force, and therefore results in instabilities. Scientific and clinical researchers introduced several methods for characterizing the development of intracranial aneurysms, through artificial (phantom) models and animal experiments. It is only recently that detailed analysis of blood flow was considered as a mean to study aneurysm development or to assess aneurysm treatment procedures. For instance, Cebal et al. studied the local hemodynamics (flow and WSS) and the formation of blebs in cerebral aneurysm by CFD simulation of the aneurysm flow before and after bleb formation under pulsatile flows [Cebal et al. (2010)]. Their findings implied that locally elevated WSS could contribute to the focalized wall damage that formed the aneurysm. They revealed the importance of the hemodynamic impact on the aneurysm development, but did not studied the how this impact led to vessel deformation.

Regarding the biomechanical modeling of blood vessels, several models and approaches were proposed in the literature (for a comprehensive overview of constitutive models of blood vessels, the reader can refer to [Vito and Dixon (2003)]). The simplest one is linearly elastic wall model, possessing the greatest advantage of low computational cost. At present, this model is still successful in some applications (see [Figueroa et al. (2006)] for example). Hyper-elastic material model offers better incompressible and stiffening behavior of the arterial wall under high strain. This model is neither too complicated nor too computationally expensive in general, thus it is widely used in cardiovascular FSI simulations (e.g., [Tezduyar et al. (2008)]). More sophisticated characteristics are also added into the wall model, such as viscoelastic, anisotropic and inhomogeneous characteristics, owing to collagen fibre and other multiple compositions (e.g., [Humphrey and Na (2002)]). Nevertheless, there is few models based on patient-specific geometries and mechanical properties in practical applications due to the difficulty in fetching all these patient-specific datum in vivo.

To predict the aneurysm growth in long term, blood vessels were often described as viscoelastic soft tissues, which exhibited hysteresis for the stress-strain relationship, and crept under constant load and relaxation under constant strain. A popular framework was proposed by Fung to model materials with a viscoelastic behavior [Fung (1993)]. This framework, named Quasi-Linear Viscoelasticity (QLV), expressed stress at any time as a function of the instantaneous strain and a reduced relaxation function. This approach was applied to many soft tissues such as muscles, ligaments [Lakes and Vanderby (1999)] and brain tissue [Drapaca et al. (2006)]. However QLV suffered from several drawbacks, in particular it relied on extensive experiments to fit the model with acquired data [Provenzano et al. (2001)]. Dedicated vessel models were used to take into account the interaction between blood flow and arterial wall: both two-dimensional linear elastic FEM models [Bathe (1998)] and three-dimensional models [Ivankovic et al. (2002)] were proposed to estimate blood flow pressure, compressive stress and wall shear stress of the vessel wall. These works, however, did not model irreversible (plastic) deformations caused by the long exposure to stress which was probably the predominant phenomenon that led to aneurysm generation. To evaluate the long-term mechanical properties of a material, different approaches were applied. For example, Aklonis et al. relied on a modified version of the Boltzmann superposition principle to simulate the aging process of polymers [Alkonis et al. (1983)]. Other approaches modeled the creep phenomenon [Hadid et al. (2002)] to reproduce the long-term evolution of the deformation of certain materials.

Our objective is fast simulation of blood-structure interaction during the process of aneurysm development which usually lasts for hundreds of days. We propose a computationally efficient approach for solving both the problems of

fluid simulation and the soft tissue deformation, and consider the influence of soft tissues surrounding the vessels on the growth of aneurysm. Although this work is only preliminary, it will eventually permit to study the influence of different mechanical factors, and to evaluate the size of aneurysm after a certain period of time.

4.2 Blood-Coil Interaction

In this application, we aim at a planning system for the endovascular surgery of coil embolization, which allows to dynamically plan coil embolization for two key steps of the procedure: choice and placement of the first coil, and assessment of the number of coils necessary to reduce aneurysmal blood velocity. This computer aided system requires not only fast computation of the blood flow before and after implanting the coil(s), but also real-time simulation of the interaction between a coil and the complex flow during the surgery.

In Section 4.2.1, we first introduce the notion of porous media to model the impact of the inserted coil(s) onto the flow (as a change of flow pattern and a decrease of velocity), then we show how the reverse effect, i.e., the drag force applied onto the coil due to blood velocity, can be computed. In Section 4.2.2, we propose an approach to achieve real-time computation of coil-flow bilateral influence, necessary for interactive rehearsal of the procedure on computer. Finally, we provide the blood flow simulation results on the aneurysm models with interesting clinical characteristics both before and after placing the coil(s), and a simulation result of coil deployment without and with the influence of the blood flow respectively in Section 4.2.3.

4.2.1 Modeling Blood-Coil Interaction

4.2.1.1 Porous Media Model

Usually, the diameter of cerebral aneurysms treated by coil embolization ranges from 3.5mm to 10mm , while the typical diameter of coils chosen for cerebral aneurysms ranges from 0.2mm to 0.4mm , which is quite small compared to the aneurysm size (0.02 to 0.11 times of the cerebral aneurysm diameter). Most of the coils have a curly or spiral shape (the circular memory is between 2mm and 16mm), and after inserted into the sac of aneurysms, they are always randomly distributed, forming the shape of a twisted nest (Figure 4.1). Considering the relatively tiny dimension of coils and their random distribution in aneurysm, coils are modeled, from a statistical point of view, as porous media in the sac of aneurysm.

We divide the fluid domain \mathcal{D} into 3 sub-domains, a coil-free and a coil-filled sub-domain, as well as a transitory sub-domain between them which allows the



Figure 4.1: The shape of detachable coils before and after deployment. (a)-(b) Curly-shape and spiral-shape coils before deployment; (c) nest shape after deployment.

porous parameters to vary smoothly between the first two sub-domains. However, blood motion in all sub-domains is described uniformly by the Navier-Stokes equations (vorticity-based) of Brinkmann type:

$$\begin{aligned} \frac{\partial \boldsymbol{\omega}}{\partial t} + \mathcal{L}_v \boldsymbol{\omega} &= \frac{\mu}{\rho} \Delta \boldsymbol{\omega} - \frac{\mu \varphi}{\rho k} \boldsymbol{\omega} - \frac{\varphi^2 C_D}{\sqrt{k}} \nabla \times \mathbf{b}, \\ \nabla(\varphi \mathbf{v}) &= 0 \quad \boldsymbol{\omega} = \nabla \times \mathbf{v} \quad \mathbf{b} = \mathbf{v} |\mathbf{v}|, \end{aligned} \quad (4.1)$$

where $\boldsymbol{\omega}$ is vorticity, and \mathbf{b} equals to velocity \mathbf{v} multiplied by its magnitude. In addition to density ρ and viscosity μ , which are two parameters characterizing the fluid, three more parameters are used to describe the properties of porous media: porosity φ , permeability k and drag factor C_D . Porosity φ describes the volume ratio of pores to the total coil-filled sub-domain, $\varphi = 1 - V_{coil}/V_{sac}$, where V_{coil} is the accumulated volume of all coils, and V_{sac} is the volume of the aneurysm sac. The permeability k measures the fluid conductivity through porous media, $k = \varphi^3 / cS^2$, where c is the Kozeny coefficient related to the micro-shape of the porous media (for coils, the value for cylinders is chosen, $c = 2$), and S is the ratio of the surface area of all coils to the volume of porous region V_{sac} . The drag factor C_D can be derived from the computation of the local Reynolds number. In Equation 4.1, the advection term $\mathcal{L}_v \boldsymbol{\omega}$ and the viscous term $\Delta \boldsymbol{\omega}$ are exactly the same as the standard Navier-Stokes Equations (Equation 2.2). The only difference is the last two porous terms being added to consider the influence of the porous media. Note that when $\varphi \rightarrow 1$ and $k \rightarrow \infty$, these porous terms disappear, therefore, Equation 4.1 is identical to the standard Navier-Stokes equations, within the coil-free region.

By solving this equation of the uniform presentation for the whole domain, we can simulate the blood flow without coils or with different coil packing density (expressed as the volume ratio of V_{coil}/V_{sac}). Still using the DEC framework, we only need to add the computation of two porous terms to the numerical im-

plementation presented in Section 3.3. The curl of \mathbf{b} ($\nabla \times \mathbf{v} |\mathbf{v}|$) is discretized as a dual 2-form B , represented as a vector of size $|E|$. The calculation of B is similar to that of the circulation around the loop of each dual face's boundary in the backtracking step. The discrete version of the last two terms in Equation 4.1,

$$-\frac{\mu\varphi}{\rho k}\Omega - \frac{\varphi^2 C_D}{\sqrt{k}}B,$$

is added to the vorticity Ω at each time step.

4.2.1.2 Coil Model and Drag Force

The mechanical model of coil is based on the work of Dequidt et al. [Dequidt et al. (2008)] where coil was modeled as serially linked beam elements. The following equilibrium equation governs the movement and deformation of these beam elements:

$$\mathbf{M}\ddot{\mathbf{x}} + \mathbf{D}\dot{\mathbf{x}} + \mathbf{K}\mathbf{x} = \mathbf{f},$$

where $\ddot{\mathbf{x}}$, $\dot{\mathbf{x}}$, and \mathbf{x} represent respectively the vector of acceleration, velocity and node position of the beam element, and \mathbf{f} is the external force applied to the coil (such as interaction force generated by blood flow). In this equation, \mathbf{M} is a diagonal matrix describing the lumped masses at nodes. \mathbf{D} is the damping matrix. The global stiffness matrix \mathbf{K} is a band matrix due to the serial structure of the model. The coil motion is obtained by solving the governing equation using the finite element approach, which can be optimized for real-time computation by taking advantage of the structure (tri-diagonal band) of its stiffness matrix.

In the existing simulations of aneurysm embolization, the interaction force between blood and coil was only studied for the blood from a global view, while the local reacting force on coils during the implanting process was ignored. In fact, the last term of equation 4.1 is a description of the interaction force, but treated as an averaged quantity. When computing the reaction on the coil, we apply its local version, which is the drag force of flow over cylinder (the coil is considered to consist of serially linked cylinder segments):

$$\mathbf{F}_D = \frac{1}{2}C_D\rho\mathbf{v}_\perp|\mathbf{v}_\perp|Al,$$

where \mathbf{v}_\perp is the velocity orthogonal to the coil, A is the cross-sectional area of the coil, l is the length of one short cylinder segment, and \mathbf{F}_D is the drag force applied on this segment. The velocity parallel to the coil is neglected, since it only produces shear force on the coil, which is insignificant compared to the drag force, and have little impact on the movement of the coil in the blood. Hence, the reacting force on the coil only depends on local fluid velocity.

4.2.2 Real-Time Simulation of Coil Embolization

In this section, we show how the two models described above can be combined in one single framework, and used for real-time simulation of coil embolization. Given periodically time-varying boundary conditions at the inlet and outlet vessels around aneurysm, we solve the Navier-Stokes equations of Brinkmann type with a constant coil packing density by the DEC approach, and obtain the velocity at each tetrahedron center of the mesh at each time step. Then these velocity values are used to interpolate the velocity at the positions of coil segments and apply appropriate drag forces on the coil. The coil can provide real-time feedback inside the aneurysm at any time step during embolization. After a certain amount of coil(s) being deployed in the aneurysm, the velocity of blood flow is recomputed at the new level of coil packing density. We choose this loosely coupled approach and update the porous parameters (porosity φ and permeability k) only after coil packing density increasing notably, because a small segment of coil is quite tiny compared to aneurysm, and has little significant influence on the blood flow, in particular on the main flow structures. In fact, the loosely coupled approach we propose allows to relatively independently compute the blood and coil motion. As a consequence, it is easier to develop accelerating strategies for both systems separately. Moreover, computation of blood flow and coil can be parallelized. Because the impact of the flow onto a coil is local, while the reverse impact of the coil(s) onto the flow is global. In our case, blood flow simulation requires smaller time steps and more computational time. Thanks to the loosely coupled approach, the coil motion does not need to be updated as frequently as the blood simulation, and the velocity field of blood can be pre-computed if necessary.

The extra time induced by computing porous terms is less than 1% of the computational time to simulate the pure blood flow. As a result, the analysis of computational time and the accelerating techniques discussed in Chapter 3 are also applicable here. For the purpose of real-time refresh rate, we consider using relatively coarse mesh to reduce the size of the linear systems to be solved, and using large time steps to lessen the iterations necessary to simulate one second. As in other applications where real-time computation is sought, the objective is then to reach the best trade-off between accuracy and computational time. From the results of Section 3.5, we can see that the error induced by a lower resolution of the mesh and a large time step is limited and acceptable for the simulation of coil embolization. It is possible to achieve real-time simulation when relying on relatively coarse meshes (i.e., meshes with less than 8,000 elements). But this is not always sufficient for three-dimensional simulation when high accuracy is needed.

In order to achieve interactivity in three-dimensional simulation, we set up

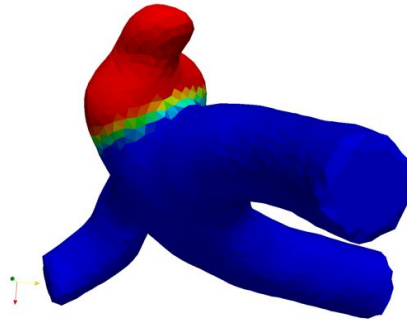


Figure 4.2: Partition of the aneurysm volume. A transitory stripe (in green) of 1mm is defined between the porous region (in red) and the pure fluid region (in blue).

a database of velocity filed for one cardiac period as we assume the simulation is performed over a series of identical cardiac cycles. Periodically time-varying boundary conditions are set for a duration covering a complete cardiac cycle (usually one cardiac cycle lasts about 1s), and the velocity field is computed and stored for multiple time steps (20 to 30 steps in our application). This process is repeated for different coil packing density in the aneurysm, and the database of velocity fields (typically 100 sets) of the blood flow with several levels of coil packing density and at multiple time steps covering one cardiac period is built, and then is used in the simulation of coil motion to compute the drag force on coils.

4.2.3 Results

We choose two patient-specific models of aneurysms with large necks, which are of interesting clinical characteristics, because successfully placing the first coil in such aneurysms is more tricky as the coil may be pushed out of the sac by the blood flow. We provide the blood flow simulation results both before and after placing the coil(s), and a simulation result of coil deployment respectively without and with the influence of the blood flow.

We performed simulations on the cerebral aneurysm with a small sac of volume 132.1mm^3 (usually the sac volume of a cerebral aneurysm varies from 100 to 1000mm^3) and a wide neck of dimension 7.0mm . The typical Guglielmi detachable coils (GDCs) used for embolization of cerebral aneurysms are GDC18 (0.385mm), GDC18-soft (0.346mm), GDC10 (0.254mm) and GDC10-soft (0.244mm). The mean velocity inside the aneurysm sac is about 50mm/s , and the corresponding local Reynolds number is around 4. It can be derived that the drag factor C_D is between 2 and 4 both from the experimental and theoretical study on the flow past a cylinder (see [Tritton (1959)] for example), and in our simulation, we use the value $C_D = 2.2$. A transitory strip of 1mm is defined between the coil-filled and the coil-free sub-domain (Figure 4.2). The coil

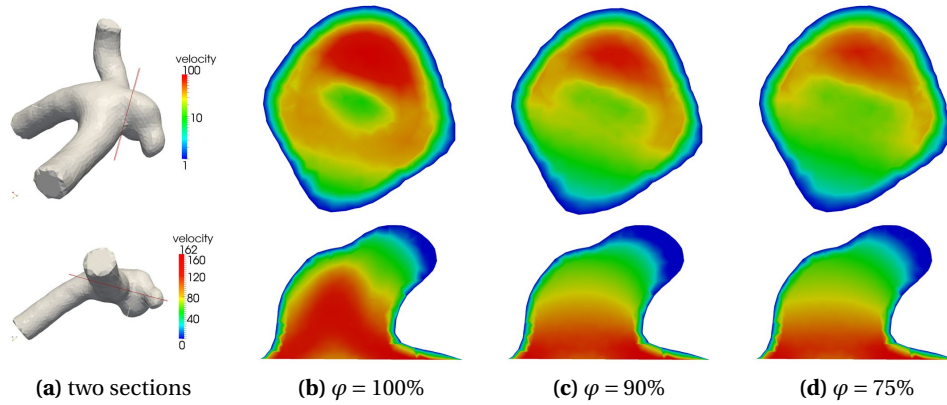


Figure 4.3: Coil embolization of a small aneurysm. The velocity magnitude on two sections (displayed in (a)) (b) before the embolization, (c) after the first coil deployed, and (d) after the final coil deployed.

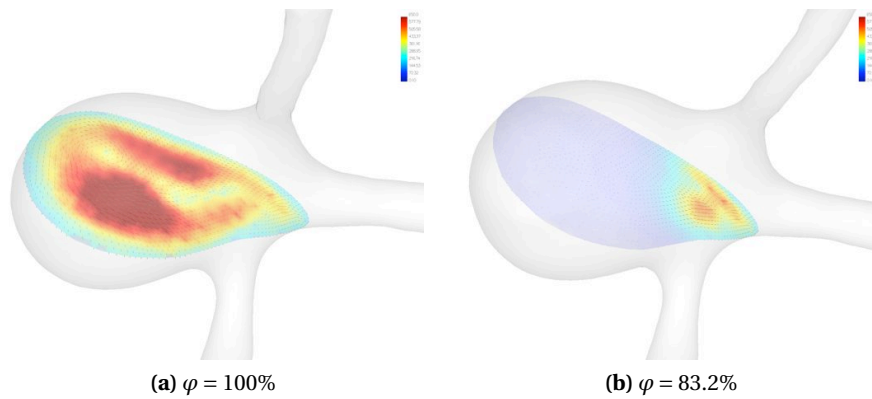


Figure 4.4: Coil embolization of a large aneurysm. The contour of velocity magnitude (a) with no coil, (b) with 16.8% volume filled with coils.

of length between 40 to 300mm can be chosen. From the clinical experience, the final coil packing density is around 25% (i.e., the porosity φ is around 75%). In Figure 4.3, we show the blood flow without coils, with 10% and 25% volume filled with coil(s) of type GDC10, which are approximately the cases after the first and the final coil deployed respectively. The velocity magnitude contours are compared on two sections, crossing the neck and the sac respectively. From the comparison on the neck section, we can see that every incremental increase in coil packing density is accompanied by a decrease in cross-neck flow rate. Additionally on the sac section, after inserting the first coil, the velocity magnitude over the whole sac region has been reduced, which creates a favorable hemodynamic environment for the deployment of the following coils.

The simulation is also performed on another aneurysm with a large sac of

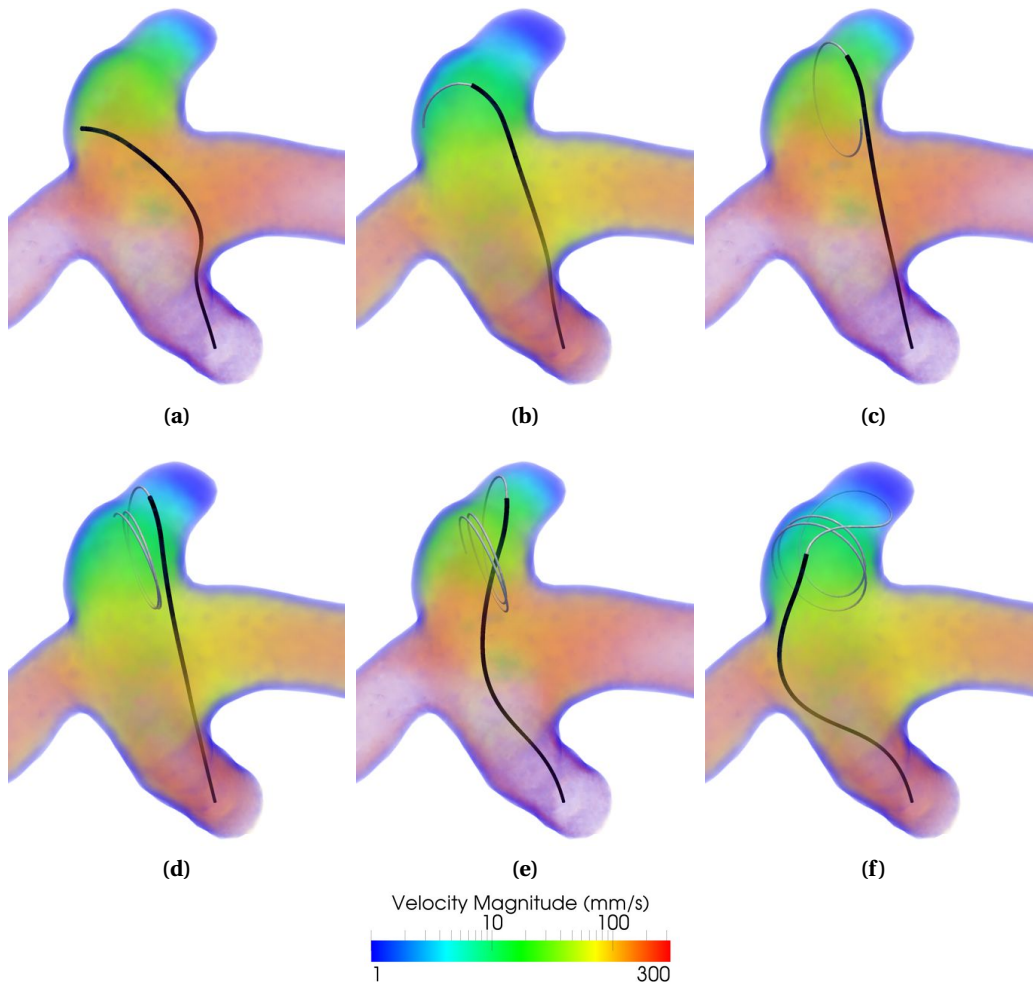


Figure 4.5: Simulation of coil embolization: (a) The catheter (black) reaches at the aneurysm neck through vessels. (b)-(f) The first coil (silver) is delivered by the catheter and inserted into the aneurysm. The colorful volume displays the periodically varying velocity field.

volume 897.6mm^3 and a wide neck of dimension 8.2mm . Figure 4.4 shows the velocity magnitude contours before and after placement of a GDC18 of length 30mm ($\varphi = 83.2\%$). Our results are in accordance with recent studies based on in vitro experiments and on CFD simulations (see [Kakalis et al. (2008)] for instance). Such aneurysms are difficult to treat, as the velocity in the large sac is much higher than small ones, and the coil might be pushed out of the wide neck by the blood flow during deployment.

Figure 4.5 displays the simulated process of placing the first coil into the small aneurysm. After the catheter is advanced in the vascular network to reach the position of the aneurysm, the coil is delivered through the catheter and inserted into the aneurysm. The contact among the catheter, the coil and the ves-

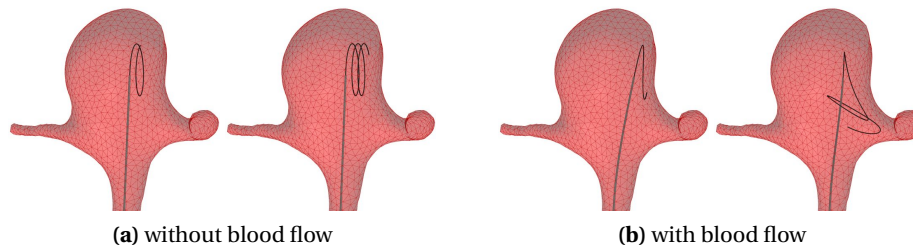


Figure 4.6: The influence the blood flow on coil deployment: Simulation of coil deployment (a) without and (b) with the influence of blood flow.

sel wall, as well as the interaction with the blood flow are all included in this simulation. Figure 4.6 presents the simulation of coil deployment on the large aneurysm without and with the influence of the blood flow. The difference between the two cases is quite obvious, and suggests that the impact of the blood flow on the coil cannot be ignored during the embolization procedure, especially when placing the first coil into an aneurysm with large neck. While the simulation without flow is unrealistic, the supplement of blood flow influence provides a simulation and overall behavior much closer to what takes place in an actual procedure (e.g., if the diameter of circular memory is too small compared to the aneurysm size, it gets pushed out of the aneurysm by the flow). By combining patient-specific aneurysm geometry with accurate coil and flow models, we believe such coupled simulation has the potential to become accurate enough to support medical planning applications.

4.3 Blood-Vessel Interaction

In this section, we explore the complex problem of the development of cerebral aneurysms with an emphasis on the interaction between arterial flow and soft tissue deformations. To simulate the interaction in this physiological process, the method is based on three models, all of which must be compatible with fast computation requirements. We provide overview of the method (Section 4.3.1) and then describe our choices of these models and our motivations. Firstly, blood pressure in the vascular structures around the diseased vessel should be derived from the blood flow simulation. We rely on the DEC method to simulate the flow and then compute the pressure along the interface between fluid and structure (Section 4.3.2). Secondly, a constitutive model needs to be chosen to describe soft tissue deformation. We also take into account the surrounding tissues (such as brain tissues and other anatomical structures), not only the arterial wall, in the computation of the interaction (Section 4.3.3). Thirdly, a method for computing the long-term effect of blood pressure onto the arterial wall is re-

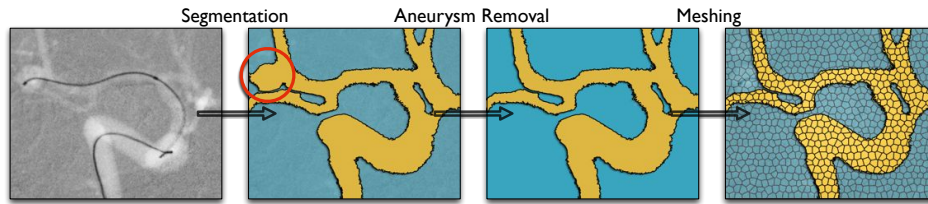


Figure 4.7: Mesh acquisition process. The medical image is segmented, then the existing aneurysm is manually removed, and meshes are generated using CGAL library.

quired. In our method, the very different time scales that exist between the flow evolution and soft tissue deformation process are handled using creep formulation (Section 4.3.4). Our preliminary results based on patient-specific data sets show a good correlation between our simulations and the actual data. They also highlight the relationship between the shape of aneurysm and the heterogeneity in the brain tissues surrounding the aneurysm (Section 4.3.5).

4.3.1 Overview of the Method

Our approach focuses on the coupling between fluid simulation and soft tissue deformation that leads to the occurrence of aneurysm in a damaged vessel. However, it is a complex, computationally expensive problem when including flow computation and soft tissue deformation in a single simulation using FSI methods, and it would typically fail to provide results in a reasonable time for clinical use. We choose an alternative strategy, based on the concepts of interleaved simulation and creep modeling. Interleaved simulation was proposed by Baraff and Witkin to solve a coupled systems successively assuming the coupling constraints were constant over the resolution step [Baraff and Witkin (1997)]. To simulate the influence of blood flow onto aneurysm and surrounding soft tissues, we also need to model the long term exposure of soft tissues to the pressure exerted by the fluid. This is achieved by using a creep model for blood pressure. Starting from a segmented vascular network, the aneurysm is manually removed (Figure 4.7), while the remaining vessels are supposed to define the region around the diseased vessel before vessel expanding to form an aneurysm, and serve as an input to generate a triangulated mesh using the CGAL library [CGAL].

Figure 4.8 illustrates the two stages in the interleaved iteration of our method. Firstly, the blood flow simulation is performed on the current mesh using boundary conditions defined by the vessel geometry and time-averaged velocities found in the literature [Marshall et al. (2004)]. The simulation runs for a certain number of time steps in order to reach a stable flow (to simplify the problem, we ignore the pulsation of blood pressure and simulate the flow based

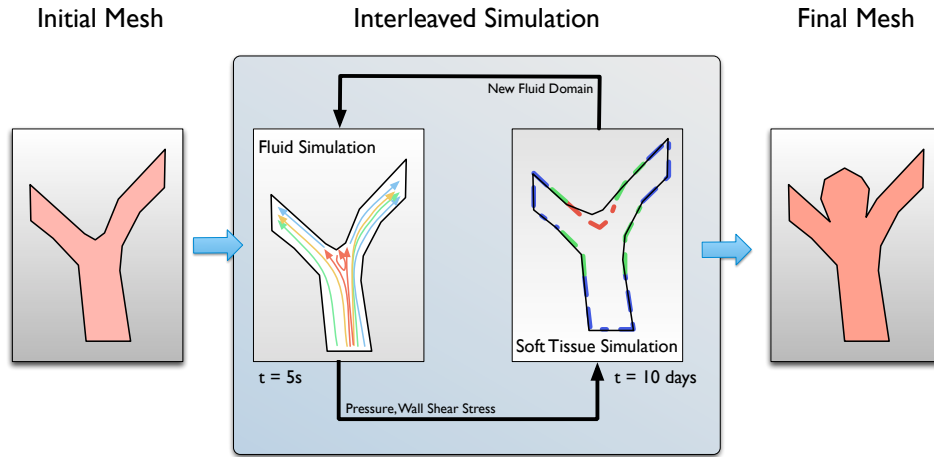


Figure 4.8: Overview of the approach. Starting from an initial mesh of the vessel, the simulations of blood flow and deforming soft tissues are performed successively for a predefined number of iterations, thus leading to the final shape of the aneurysm.

on static time-averaged boundary conditions), from which the resulting blood pressure is derived (time scale of this simulation ranges from 1 to 5s). During this stage, the vessel wall is supposed to be rigid, since little plastic deformation (the elastic deformation due to the pulsation is neglected) takes place in such a short period. Secondly, the external forces applied on the vessel and emerging aneurysm boundaries are computed from blood pressure on the vessel wall, and extrapolated in time (over a couple of weeks). Exposed to the forces caused by blood pressure, the soft tissues start to deform until an equilibrium state is reached (time scale ranges from 5 to 10 days). During this stage, blood pressure is considered as constant, since the deformation of vessel is small, and has limited influence onto the flow. Once large deformation takes place, the deformed vessel defines a new fluid domain. The blood flow simulation and the soft tissue simulation are performed repeatedly in this interleaved manner for several iterations, thus leading to the development of aneurysm.

4.3.2 Blood Pressure Computation

Usually the absolute pressure value does not mean anything, while the pressure difference plays an important role. Therefore, we explain how we use the DEC method to compute the pressure gradient along the interface, which is required to simulate the interaction with soft tissues. With the assumption of no-slip boundary conditions ($v = 0$ on the vessel wall), and after the flow reaches a stable status ($\partial v / \partial t = 0$), the pressure gradient on the boundary can be simply derived from the Navier-Stokes Equation (Equation 2.1).

$$\nabla p = \mu \Delta v.$$

The discrete pressure gradient is defined as dual 1-form G_P , and the flux U is divergence-free ($dU = 0$), so we have

$$G_P = \mu \star \Delta U = \star d \star^{-1} d^T \star U.$$

In two dimensions, the gradient can be transferred from dual edge to the corresponding primal edge as $\star_1^{-1} G_P$, with the direction of the dual edge (perpendicular to the primal edge). Then we compute the pressure gradient on each boundary vertex by averaging the pressure gradient on its incident edges. In three dimensions, the pressure gradient can be similarly computed.

4.3.3 Brain and Vessel Tissues Modeling

In our approach, brain tissues and vessels are considered as a single but heterogeneous domain. This is mainly motivated by the lack of information regarding the interaction (in particular the friction) at the interface between the external vessel layer and the surrounding tissues. Consequently we assume a non-slip condition at the interface, and we rely on a unique mesh of the soft tissue domain. To simulate the deformation of the soft tissues while aiming at computationally efficiency, we developed a corotational FEM formulation [Felippa (2000)] based on triangular elements, with non-homogeneous material properties. Typically, three different sub-domains are considered: arterial wall, brain tissues and surrounding anatomical structures of different stiffness than brain tissues (e.g., other vessels, bones).

4.3.4 Creep Modeling

As the occurrence of aneurysm is usually a process lasting for months or years, we assumed that transient or small oscillatory motion of vessel wall due to the pulsatile nature of blood flow can be neglected. On the other hand, we consider the influence of neighboring tissues, which contain not only arterial wall but also brain tissues and other structures present in the neighborhood of the emerging aneurysm. These structures are therefore included in the soft tissue deformation model. To compute the long-term effect of blood pressure, experimental approaches such as proposed in [Lakes and Vanderby (1999)] are not applicable since experimental data on aneurysms in vivo is very difficult to acquire. Alternatively, we propose to a computational approach derived from classical three-step creep models [Hadid et al. (2002)]. However, we only consider the secondary creep (permanent creep that leads to material dilation), governed by the equations as follows:

$$\dot{\epsilon} = A \left(\frac{\sigma - \sigma_0}{E} \right)^n,$$

where $\dot{\epsilon}$ is the creep strain rate, E is the Young modulus of material, σ_0 is the initial stress, σ is the applied stress, A and n are constants dependent on the

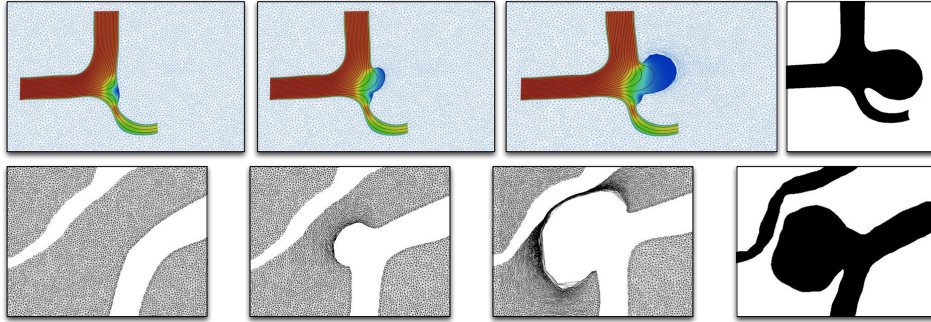


Figure 4.9: Simulation of aneurysm growth on two patient data sets. The rightmost images are extracted from patient data, other images are from our simulation. The color scale represents fluid velocities and curves represent streamlines.

material. Solving this first-order equation leads to an expression of the strain as a function of time and the applied stress. As we use the principle of interleaved simulation, we consider that the applied stress is constant during the soft tissue deformation, thus the creep strain linearly scales with time and highly depends on E .

4.3.5 Results

To assess our method, we perform the simulations using two different patient data sets. In Figure 4.9, the rightmost images are extracted from real patient data. Then the aneurysms are manually removed and meshes of about 11K triangles are generated as shown in the leftmost images, where the iterations (each consisting of flow simulation and soft tissue deformation) starts. A time of 10 days is used in the creep model. During this period, simulation of aneurysm growth is based on a constant pressure field. The various material parameters were obtained from the literature (arterial wall stiffness: $E = 2MPa$, $\nu = 0.45$; brain tissues $E = 5kPa$, $\nu = 0.35$). As aneurysm develops, the volume of the fluid domain increases. Therefore it is necessary to remesh the domain after each iteration. The second image of each row displays the status during the development of aneurysm, while the third image is the final status (after 30 iterations) where the simulated aneurysm has similar shape as the real one.

On an Intel i7 3.33GHz processor, each iteration takes about 30 seconds to compute, and the remeshing also takes about 30 seconds, thus a total time of 30 minutes is needed to simulate the equivalent actual time of 300 days. Although these results are obtained from two-dimensional simulations, the similarity between simulated and real profiles shows that our method is promising.

4.4 Discussion

Simulation of blood flow and its interaction with therapeutic devices (e.g., catheters, coils) or surrounding soft tissues (e.g., vessels, brain tissues) is a challenging problem, as it requires not only to faithfully represent the real physical processes, but also to perform in real time or at interactive rate. Before the two simulation methods described in this chapter can go into clinical service, it is necessary to make further efforts to improve the reality of the simulation.

Using our pre-computed strategy, the blood and coil motion can be simulated in real time. However, the simulated results should be further validated for the behaviors of both blood flow and coil within aneurysm during and after the procedure of coil embolization. The comparison between simulated results and in vivo data would be difficult, because current imaging techniques are not competent to provide images with a high resolution either in space or in time, and some of them can provide only two-dimensional data. Additionally, it is also not practicable to expose patients to the radiation over a long time due to safety reason. Yet, the real flow data obtained from the noisy images in a coarse time/space resolution provides interesting insights. These values can be regularized by the mathematical and CFD models. The combination of noisy real flow and simulated flow will provide more reliable hemodynamic characteristics and a more feasible operation to get three-dimensional flow with higher space/time resolution. Furthermore, the regularized real flow data is useful to set boundary conditions for the simulation. We set uniform boundary conditions in our simulation for now, which may have an impact on the reality of simulated results, especially when the inlet and outlet vessels are too short to obtain a fully-developed flow profile near the aneurysm.

In the simulation of aneurysm growth, the arterial wall is simply described as a linear elastic model, which is not sufficient to represent the complex motion and deformation. When large deformation takes place, remeshing of both the fluid region and the tissue region is required, but the latter one is ignored in our current method. In addition to geometry changes, the physical and physiological properties of the arterial wall are also changing and leading to the final stable configuration. As a result, we need more profound understanding of this physiological process to generate an advanced model. Moreover, the simulation from two dimensions to three dimensions and the validation should be undertaken.

In the future, we will aim at including multiple interactions in a single framework. The artery or aneurysm pulsation due to the pulsatile blood flow was observed over one cardiac cycle in some studies [Schwartz et al. (2009)] [Valencia et al. (2009)]. As a result, the simulation of the interactions among blood, surgical device, and vessels will provide valuable information for assisting physicians in planning and evaluating surgical procedures of repairing the vascular diseases.

More applications in medical simulation are in our consideration. In the simulation of blood-coil interaction, we only provided the results during coil embolization. Regarding the long term results, clinical data reported that aneurysm recanalization and coil compaction after coil embolization of intracranial aneurysms had occurred in as many as 40% cases [Raymond et al. (2003)], and revealed that the neck and sac dimension was crucial for the long-term success of coil embolization [Hope et al. (1999)]. But the patient-specific prediction of the long-term outcome on aneurysm occlusion is not available until today, due to the complex interactions of coils with the local blood flow and surrounding tissues. Thus it is promising to model the interaction among blood flow, coils and surrounding tissues and to predict the changes in long term using patient-specific data. Besides, the simulation of fluids other than blood flow, such as the air in the respiratory system, is also interesting for us.

CONCLUSION AND PERSPECTIVES

5.1 Conclusion

The objective of my work during this PhD study was to model the blood flow for accurate and real-time simulation in the context of coil embolization of cerebral aneurysms. Most of the previous works in this field relied on established physics-based models in order to obtain accurate hemodynamic characteristics around the aneurysm, and the computational times were generally several hours. On the other hand, many computationally efficient approaches for fluid simulation were proposed in the field of computer graphics, aiming at visually convincing simulations, but not physical accuracy. Generally speaking, these two significant pursuits, accuracy and computational efficiency, are often contradictory. In this work, we strived to achieve real-time simulation of blood flow on patient-specific model, which can lead to results accurate enough for medical planning applications.

First of all, we introduced the DEC method, initially applied in the field of computer graphics, into hemodynamics simulation for the purpose of fast computation. However, a much deeper analysis of this new method applied in the blood flow simulation was performed through various experiments both in two and three dimensions, and several solutions were proposed to overcome the limitations of the method. We validated the DEC method by comparing with a widely used commercial software, and the comparative results not only showed the similarity of the results, but also revealed that the numerical error introduced by using a coarser mesh was limited, thus an appropriate mesh resolution, allowing fast computation while minimizing the impact on the accuracy, was suggested for medical simulation. Furthermore, we also examined the stability of the DEC method, and demonstrated that more advanced backtracking schemes improved the numerical stability of the method and allowed larger time steps, which, in turn, contributed to real-time computation. More importantly, we identified the impact of mesh quality on the convergence and accuracy, which

had been ignored or underestimated in previous works because of their different objectives. And we provided several solutions to generate higher-quality meshes. Due to these improvements, our method was significantly faster than previous approaches for blood flow simulation around aneurysm while providing similar results to that of the reference software.

Secondly, we extended the fast simulation of pure blood flow to blood-coil interaction during aneurysm embolization. Porous media model was used to describe the presence of coils in the aneurysm, and was modeled by adding extra terms to the Navier-Stokes equations to consider the impact of the coil onto the blood flow. Such modification of the equation required little additional computation to be handled. On the other hand, we also modeled the reciprocal effect, i.e., the impact of the flow onto the coil. This effect had been ignored by previous works, but our simulated results demonstrated that the bilateral influence was essential in the context of planning the coil embolization training and planning. More importantly, the results showed that our approach permitted real-time simulation of the interaction between coils and blood flow during coil embolization, due to the fast computation of both fluid and structure, as well as the loosely coupled strategy we proposed.

Finally, we targeted simulating the process leading to the development of aneurysms. Since the overall process was extremely complex, and involved numerous factors, we only considered a small but important part of the process, starting from part of the vessel wall being degenerated. We proposed a computationally efficient approach for solving both the fluid and the soft tissue deformation problems. Moreover, we also considered the influence of other anatomical structures surrounding the vessels in the growth of aneurysm. By using our approach in two dimensions, we could simulate in a few minutes a process which took normally hundreds of days. This eventually permitted to study the influence of different mechanical factors, and to evaluate the size of an aneurysm after a certain period of time. Our preliminary results were very encouraging, as they showed a good correlation with existing patient data.

5.2 Perspectives

5.2.1 Accuracy and Stability

The DEC method, based on unstructured meshes, is in favor of describing irregular boundary of patient-specific anatomical geometries. Generally speaking, when a mesh of simplicial elements (triangles or tetrahedra) is used to approximate a continuous domain, the accuracy of numerical solution depends on the sizes and shapes of the elements. Moreover, the stability of the DEC method also depends on mesh geometry, as the other numerical methods (for instance,

the conditioning of the stiffness matrices in FEM are related to mesh geometry). However, the impact of mesh quality had not been studied for the DEC method in previous works; even a quantitative definition of mesh quality has not been mentioned. We are now focusing on investigating the connection between mesh quality and the accuracy, the convergence of the DEC method. We propose to quantitatively measure mesh quality by the error of numerical solution compared to analytical solution of a specified equation in terms of accuracy, and the condition number of the Laplace operators in terms of convergence. Furthermore, our objective is to further improve mesh quality with the purpose of lower errors and higher stability. Hodge-Optimized Triangulation (HOT) [Mullen et al. (2011)] is a good starting point for improving mesh quality. Using metrics which are specific to the DEC method, we have seen improvements in the results in the two-dimensional case. In particular, it results in increase of the dual edge length, which has a positive outcome on the numerical accuracy of the method. Further investigation should be made, in particular extending the optimization method to the three-dimensional case, where important improvements can be expected.

On the other hand, modification of the DEC method could be an alternative solution to the problems caused by low-quality meshes. For example, the immersed boundary method (IBM) and the DEC method can be combined, so that the absolutely high-quality regular mesh containing the fluid region but not conforming to the exact boundary can be used. In addition, the interpolation error and the discretization error are required to be further studied and reduced. As for the simulation of aneurysm growth, more advanced and complex model of the vascular wall and the remeshing process are required to reach higher fidelity. Finally, the combination of simulated results and real data obtained from imaging techniques is an interesting direction in our future work, as it not only provides more accurate results, but also is a more feasible approach to the acquisition of three-dimensional hemodynamic data in real time compared to medical imaging methods.

5.2.2 Boundary Conditions

We paid attention to the importance of patient-specific anatomical geometry in simulating the blood flow, but used simplified boundary conditions for the inflow and outflow. We set a sinusoidally pulsatile flux at inlet, and the mean and maximum values were based on the measurements from MRI [Marshall et al. (2004)]. The total flux at the outlet(s) was set to be equal to the influx. If there were more than one outlet, the distribution of the blood flow was estimated by Bernoulli's principle in the assumption that the pressure is identical at every outlet. However, we acknowledge that these boundary conditions are not either realistic or patient-specific. A better strategy is to use a multi-dimensional method

by combining one-dimensional model of the global vascular systems (which has already been established in our framework SOFA¹) and three-dimensional model of the local vessels in interest. So upstream and downstream of the local vessels can be computed in one dimension and provide boundary conditions for three-dimensional simulation [Vignon and Taylor (2004)]. Yet, blood flow is not always periodic in time, more advanced models can be applied, such as [Vignon-Clementel et al. (2010)].

In addition, other techniques could also help to obtain more realistic boundary conditions. Although the medical images obtained by current techniques (e.g., phase contrast magnetic resonance imaging and Doppler ultrasound) are noisy and cannot provide the velocity data in high space or time resolution, a better velocity profile can be fitted by combining CFD simulated results. Besides, we could also benefit from the state-of-the-art medical instruments to obtain patient-specific data, such as the ultra-miniature pressure catheter², which is a so small sensor on the catheter that it does not significantly change the blood flow.

5.2.3 Computational Efficiency

A prominent advantage of the DEC method is the computational efficiency. Not only because large time steps can be used due to the backward advection strategy, but also the accelerating techniques we employed reduce the computational time for each iteration. Yet, real-time simulation has not been achieved when performed on a mesh consisting of over 8,000 elements. We still want to more deeply investigate various computational strategies to obtain real-time computation by using more advanced numerical schemes, such as parallel implementation on GPU of the backtracking step, optimization of linear solvers by the preconditioning technique coupled with a GPU-based conjugate gradient implementation [Courtecuisse et al. (2011)]. Additionally, more advanced techniques to generate a multi-resolution mesh, such as adaptive refinement [Prakash and Ethier (2001)], could also be a solution, as it maximizes the result accuracy while minimizing the computational effort.

5.2.4 Validation

We acknowledge that further validation is required, both on the DEC method and the medical simulation. The three-dimensional simulation of aneurysm growth and the validation should be undertaken. Working on a comparison between the simulated results and the in vivo data would be difficult yet provide interesting insights. In addition, an advanced three-dimensional visualization

¹<http://www.sofa-framework.org/>

²<http://scisense.cn/bpcatheter.html>

(e.g., [Gasteiger et al. (2010)] and [Gasteiger et al. (2011)]) of flow data could also be interesting and helpful in the clinical context.

5.2.5 Other Applications

In a long term perspective, we aim at more promising applications of the DEC method in medical simulation. First of all, it is necessary to consider multiple interactions in a single framework, such as the interactions among blood, surgical devices, and blood vessels, in order to improve the realism of the simulation. Secondly, the patient-specific prediction of the long-term aneurysm occlusion outcome after coil embolization is very helpful for surgery planning. Finally, the simulation of fluids other than blood flow, such as the air in the respiratory system, could also be investigated.

REFERENCES

- [Akiyama et al., 2010] Y. Akiyama, K. Houkin, K. Nozaki and N. Hashimoto. *Practical Decision-Making in the Treatment of Unruptured Cerebral Aneurysm in Japan: The U-CARE Study*. Cerebrovascular Diseases, vol. 30, no. 5, pages 491–499, 2010, ISSN 1015-9770.
- [Alderliesten et al., 2004] T. Alderliesten, M. Konings and W. Niessen. *Simulation of minimally invasive vascular interventions for training purposes*. Computer Aided Surgery, vol. 9, no. 1-2, pages 3–15, 2004.
- [Alkonis et al., 1983] J. Alkonis, W. MacKnight and M. Shen. *Introduction to polymer viscoelasticity*. John Wiley and Sons, New York, 1983.
- [Annambhotla et al., 2008] S. Annambhotla, S. Bourgeois, X. Wang, P. Lin, Q. Yao and C. Chen. *Recent advances in molecular mechanisms of abdominal aortic aneurysm formation*. World journal of surgery, vol. 32, no. 6, pages 976–986, 2008, ISSN 0364-2313.
- [Antiga et al., 2008] L. Antiga, M. Piccinelli, L. Botti, B. Ene-Iordache, A. Remuzzi and D. Steinman. *An image-based modeling framework for patient-specific computational hemodynamics*. Medical and Biological Engineering and Computing, vol. 46, no. 11, pages 1097–1112, 2008.
- [Auer and Gasser, 2010] M. Auer and T. Gasser. *Reconstruction and finite element mesh generation of abdominal aortic aneurysms from computerized tomography angiography data with minimal user interactions*. Medical Imaging, IEEE Transactions on, vol. 29, no. 4, pages 1022–1028, 2010.
- [Baek et al., 2010] H. Baek, M. Jayaraman, P. Richardson and G. Karniadakis. *Flow instability and wall shear stress variation in intracranial aneurysms*. Journal of The Royal Society Interface, vol. 7, no. 47, page 967, 2010, ISSN 1742-5689.
- [Ballard et al., 2008] D. Ballard, G. Filardo, G. Fowkes and J. Powell. *Surgery for small asymptomatic abdominal aortic aneurysms*. Cochrane database of systematic reviews (Online), , no. 4, page CD001,835, 2008.
- [Balocco et al., 2010] S. Balocco, O. Camara, E. Vivas, T. Sola, L. Guimaraens, H. van Andel, C. Majoie, J. Pozo, B. Bijmens and A. Frangi. *Feasibility of estimating regional mechanical properties of cerebral aneurysms in vivo*. Medical physics, vol. 37, page 1689, 2010.

- [Baraff and Witkin, 1997] D. Baraff and A. Witkin. *Partitioned dynamics*. Robotics Institute, Carnegie Mellon University, 1997.
- [Barber et al., 2007] D. Barber, E. Oubel, A. Frangi and D. Hose. *Efficient computational fluid dynamics mesh generation by image registration*. Medical image analysis, vol. 11, no. 6, pages 648–662, 2007.
- [Batchelor, 2000] G. Batchelor. *An introduction to fluid dynamics*. Cambridge Univ Pr, 2000, ISBN 0521663962.
- [Bathe, 1998] M. Bathe. *A fluid-structure interaction finite element analysis of pulsatile blood flow through a compliant stenotic artery*. Ph.D. thesis, Massachusetts Institute of Technology, 1998.
- [Beck et al., 2003] J. Beck, S. Rohde, M. El Beltagy, M. Zimmermann, J. Berkefeld, V. Seifert and A. Raabe. *Difference in configuration of ruptured and unruptured intracranial aneurysms determined by biplanar digital subtraction angiography*. Acta Neurochirurgica, vol. 145, no. 10, pages 861–865, 2003, ISSN 0001-6268.
- [Bieging et al., 2011] E. Bieging, A. Frydrychowicz, A. Wentland, B. Landgraf, K. Johnson, O. Wieben and C. François. *In vivo three-dimensional MR wall shear stress estimation in ascending aortic dilatation*. Journal of Magnetic Resonance Imaging, vol. 33, no. 3, pages 589–597, 2011, ISSN 1522-2586.
- [Binder and Heermann, 2010] K. Binder and D. Heermann. *Monte Carlo simulation in statistical physics: an introduction*. Springer, 2010, ISBN 3642031625.
- [Blanchard et al., 1990] C. Blanchard, S. Burgess, Y. Harvill, J. Lanier, A. Lasko, M. Oberman and M. Teitel. *Reality built for two: a virtual reality tool*. In *ACM SIGGRAPH Computer Graphics*, vol. 24, pages 35–36, ACM, 1990.
- [Boecher-Schwarz et al., 2000] H. Boecher-Schwarz, K. Ringel, L. Kopacz, A. Heimann and O. Kempfski. *Ex vivo study of the physical effect of coils on pressure and flow dynamics in experimental aneurysms*. American journal of neuroradiology, vol. 21, no. 8, page 1532, 2000.
- [Boll, 2008] A. Boll. *Echographic screening of the abdominal aorta in older men is useful*. Nederlands tijdschrift voor geneeskunde, vol. 152, no. 13, page 750, 2008, ISSN 0028-2162.
- [Bossavit, 2001] A. Bossavit. *Generalized finite differences in computational electromagnetics*. Progress in Electromagnetics Research, PIER, vol. 32, no. 45-64, page 77, 2001.

- [Byrne et al., 1999] J. Byrne, M. Sohn and A. Molyneux. *Five-year experience in using coil embolization for ruptured intracranial aneurysms: outcomes and incidence of late rebleeding*. Journal of neurosurgery, vol. 90, no. 4, pages 656–663, 1999.
- [Calvisi et al., 2010] M. Calvisi, S. Davis and M. Miksis. *A Mathematical Model of Intracranial Saccular Aneurysms: Evidence of Hemodynamic Instability*. Bulletin of the American Physical Society, vol. 55, 2010.
- [Canton et al., 2005] G. Canton, D. Levy and J. Lasheras. *Changes in the intraaneurysmal pressure due to HydroCoil embolization*. American journal of neuroradiology, vol. 26, no. 4, page 904, 2005.
- [Cartan, 1947] É. Cartan. *Les systemes différentiels extérieurs et leurs applications géométriques*. Bull. Amer. Math. Soc. 53 (1947), 261-266. DOI: 10.1090/S0002-9904-1947-08750-4 PII: S, vol. 2, no. 9904, pages 08,750–4, 1947.
- [Cebal et al., 2005] J. Cebal, M. Castro, J. Burgess, R. Pergolizzi, M. Sheridan and C. Putman. *Characterization of cerebral aneurysms for assessing risk of rupture by using patient-specific computational hemodynamics models*. American Journal of Neuroradiology, vol. 26, no. 10, page 2550, 2005.
- [Cebal et al., 2010] J. Cebal, M. Sheridan and C. Putman. *Hemodynamics and bleb formation in intracranial aneurysms*. American Journal of Neuroradiology, vol. 31, no. 2, page 304, 2010.
- [Cebal et al., 2011] J. Cebal, F. Mut, J. Weir and C. Putman. *Quantitative characterization of the hemodynamic environment in ruptured and unruptured brain aneurysms*. American Journal of Neuroradiology, vol. 32, no. 1, page 145, 2011.
- [CGAL] CGAL. <http://www.cgal.org/>.
- [Cha et al., 2007] K. Cha, E. Balaras, B. Lieber, C. Sadasivan and A. Wakhloo. *Modeling the interaction of coils with the local blood flow after coil embolization of intracranial aneurysms*. Journal of biomechanical engineering, vol. 129, page 873, 2007.
- [Chauhan et al., 2011] S. Chauhan, R. Coelho, S. Kalan, R. Satava and V. Patel. *Evolution of Robotic Surgery: Past, Present, and Future*. Robotic Urologic Surgery, pages 3–10, 2011.
- [Chen and Doolen, 1998] S. Chen and G. Doolen. *Lattice Boltzmann method for fluid flows*. Annual review of fluid mechanics, vol. 30, no. 1, pages 329–364, 1998, ISSN 0066-4189.

- [Chien et al., 2009] A. Chien, M. Castro, S. Tateshima, J. Sayre, J. Cebral and F. Vinuela. *Quantitative hemodynamic analysis of brain aneurysms at different locations*. American Journal of Neuroradiology, vol. 30, no. 8, page 1507, 2009.
- [Comas et al., 2008] O. Comas, Z. Taylor, J. Allard and S. Ourselin. *Efficient Nonlinear FEM for Soft Tissue Modelling and Its GPU Implementation within the Open Source Framework SOFA*. In *Biomedical simulation: 4th international symposium, ISBMS 2008, London, UK, July 7-8, 2008: proceedings*, vol. 5104, page 28, Springer-Verlag New York Inc, 2008.
- [Cooper and Taqueti, 2008] J. Cooper and V. Taqueti. *A brief history of the development of mannequin simulators for clinical education and training*. Postgraduate medical journal, vol. 84, no. 997, page 563, 2008, ISSN 1469-0756.
- [Cosford and Leng, 2007] P. Cosford and G. Leng. *Screening for abdominal aortic aneurysm*. Cochrane database of systematic reviews (Online), , no. 2, page CD002,945, 2007, ISSN 1469-493X.
- [Cottet and Koumoutsakos, 2000] G. Cottet and P. Koumoutsakos. *Vortex methods: theory and practice*. Cambridge Univ Pr, 2000, ISBN 0521621860.
- [Courtecuisse et al., 2011] H. Courtecuisse, J. Allard, C. Duriez and S. Cotin. *Preconditioner-based contact response and application to cataract surgery*. Medical Image Computing and Computer-Assisted Intervention–MICCAI 2011, pages 315–322, 2011.
- [Datta et al., 2001] V. Datta, S. Mackay, M. Mandalia and A. Darzi. *The use of electromagnetic motion tracking analysis to objectively measure open surgical skill in the laboratory-based model*. Journal of the American College of Surgeons, vol. 193, no. 5, pages 479–485, 2001, ISSN 1072-7515.
- [Delp et al., 1990] S. Delp, J. Loan, M. Hoy, F. Zajac, E. Topp and J. Rosen. *An interactive graphics-based model of the lower extremity to study orthopaedic surgical procedures*. Biomedical Engineering, IEEE Transactions on, vol. 37, no. 8, pages 757–767, 1990, ISSN 0018-9294.
- [Dequidt et al., 2008] J. Dequidt, M. Marchal, C. Duriez, E. Kerien and S. Cotin. *Interactive simulation of embolization coils: Modeling and experimental validation*. Medical Image Computing and Computer-Assisted Intervention–MICCAI 2008, pages 695–702, 2008.
- [Desbrun et al., 2003] M. Desbrun, A. Hirani and J. Marsden. *Discrete exterior calculus for variational problems in computer vision and graphics*. In *Decision and Control, 2003. Proceedings. 42nd IEEE Conference on*, vol. 5, pages 4902–4907, IEEE, 2003.

- [Dhar et al., 2008] S. Dhar, M. Tremmel, J. Mocco, M. Kim, J. Yamamoto, A. Siddiqui, L. Hopkins and H. Meng. *Morphology parameters for intracranial aneurysm rupture risk assessment*. *Neurosurgery*, vol. 63, no. 2, page 185, 2008.
- [Dillon et al., 2007] M. Dillon, C. Cardwell, P. Blair, P. Ellis, F. Kee and D. Harkin. *Endovascular treatment for ruptured abdominal aortic aneurysm*. *Cochrane database of systematic reviews (Online)*, , no. 1, page CD005,261, 2007, ISSN 1469-493X.
- [Dobrin and Mrkvicka, 1994] P. Dobrin and R. Mrkvicka. *Failure of elastin or collagen as possible critical connective tissue alterations underlying aneurysmal dilatation*. *Cardiovascular surgery (London, England)*, vol. 2, no. 4, page 484, 1994, ISSN 0967-2109.
- [Drapaca et al., 2006] C. Drapaca, G. Tenti, K. Rohlf and S. Sivaloganathan. *A quasi-linear viscoelastic constitutive equation for the brain: Application to hydrocephalus*. *Journal of Elasticity*, vol. 85, no. 1, pages 65–83, 2006.
- [Duriez et al., 2006] C. Duriez, S. Cotin, J. Lenoir and P. Neumann. *New approaches to catheter navigation for interventional radiology simulation 1*. *Computer Aided Surgery*, vol. 11, no. 6, pages 300–308, 2006.
- [Elcott et al., 2007] S. Elcott, Y. Tong, E. Kanso, P. Schröder and M. Desbrun. *Stable, circulation-preserving, simplicial fluids*. *ACM Transactions on Graphics (TOG)*, vol. 26, no. 1, page 4, 2007.
- [Felippa, 2000] C. Felippa. *A systematic approach to the element-independent corotational dynamics of finite elements*. Center for Aerospace Structures Document Number CU-CAS-00-03, College of Engineering, University of Colorado, 2000.
- [Figueroa et al., 2006] C. Figueroa, I. Vignon-Clementel, K. Jansen, T. Hughes and C. Taylor. *A coupled momentum method for modeling blood flow in three-dimensional deformable arteries*. *Computer Methods in Applied Mechanics and Engineering*, vol. 195, no. 41-43, pages 5685–5706, 2006.
- [Fisher and Rossmann, 2009] C. Fisher and J. Rossmann. *Effect of non-Newtonian behavior on hemodynamics of cerebral aneurysms*. *Journal of biomechanical engineering*, vol. 131, page 091,004, 2009.
- [Fisher et al., 2007] M. Fisher, P. Schröder, M. Desbrun and H. Hoppe. *Design of tangent vector fields*. In *ACM SIGGRAPH 2007 papers*, pages 56–es, ACM, 2007.
- [Frankel, 2004] T. Frankel. *The geometry of physics: an introduction*. Cambridge Univ Pr, 2004.

- [Fu et al., 2010] W. Fu, Z. Gu, X. Meng, B. Chu and A. Qiao. *Numerical simulation of hemodynamics in stented internal carotid aneurysm based on patient-specific model*. Journal of biomechanics, vol. 43, no. 7, pages 1337–1342, 2010, ISSN 0021-9290.
- [Fung, 1993] Y. Fung. *Biomechanics: mechanical properties of living tissues*. Springer, 1993, ISBN 0387979476.
- [Gasteiger et al., 2010] R. Gasteiger, M. Neugebauer, C. Kubisch and B. Preim. *Adapted surface visualization of cerebral aneurysms with embedded blood flow information*. In *Eurographics Workshop on Visual Computing for Biology and Medicine (EG VCBM)*, pages 25–32, 2010.
- [Gasteiger et al., 2011] R. Gasteiger, M. Neugebauer, O. Beuing and B. Preim. *The FLOWLENS: A Focus-and-Context Visualization Approach for Exploration of Blood Flow in Cerebral Aneurysms*. IEEE transactions on visualization and computer graphics, vol. 17, no. 12, page 2183, 2011.
- [Glickenstein, 2005] D. Glickenstein. *Geometric triangulations and discrete Laplacians on manifolds*. Arxiv preprint math/0508188, 2005.
- [Glowinski et al., 1997] R. Glowinski, T. Pan and J. Periaux. *A Lagrange multiplier/fictitious domain method for the numerical simulation of incompressible viscous flow around moving rigid bodies:(I) case where the rigid body motions are known a priori*. Comptes Rendus de l'Académie des Sciences-Series I-Mathematics, vol. 324, no. 3, pages 361–369, 1997.
- [Gonzalez et al., 1992] C. Gonzalez, Y. Cho, H. Ortega and J. Moret. *Intracranial aneurysms: flow analysis of their origin and progression*. American journal of neuroradiology, vol. 13, no. 1, page 181, 1992.
- [Gould, 2007] D. Gould. *Interventional radiology simulation: prepare for a virtual revolution in training*. Journal of Vascular and Interventional Radiology, vol. 18, no. 4, pages 483–490, 2007.
- [Groden et al., 2001] C. Groden, J. Laudan, S. Gatchell and H. Zeumer. *Three-dimensional pulsatile flow simulation before and after endovascular coil embolization of a terminal cerebral aneurysm*. Journal of Cerebral Blood Flow & Metabolism, vol. 21, no. 12, pages 1464–1471, 2001.
- [Grotberg and Jensen, 2004] J. Grotberg and O. Jensen. *Biofluid mechanics in flexible tubes*. Annual review of fluid mechanics, vol. 36, no. 1, page 121, 2004.
- [Hadid et al., 2002] M. Hadid, S. Rechak and A. Zouani. *Empirical nonlinear viscoelastic model for injection molded thermoplastic composite*. Polymer composites, vol. 23, no. 5, pages 771–778, 2002.

- [Hayashi et al., 1980] K. Hayashi, H. Handa, S. Nagasawa, A. Okumura and K. Moritake. *Stiffness and elastic behavior of human intracranial and extracranial arteries*. Journal of biomechanics, vol. 13, no. 2, pages 175–179, 1980, ISSN 0021-9290.
- [Hernandez and Frangi, 2007] M. Hernandez and A. Frangi. *Non-parametric geodesic active regions: Method and evaluation for cerebral aneurysms segmentation in 3DRA and CTA*. Medical image analysis, vol. 11, no. 3, pages 224–241, 2007.
- [Hirani, 2003] A. Hirani. *Discrete exterior calculus*. Ph.D. thesis, 2003.
- [Hope et al., 1999] J. Hope, J. Byrne and A. Molyneux. *Factors influencing successful angiographic occlusion of aneurysms treated by coil embolization*. American journal of neuroradiology, vol. 20, no. 3, page 391, 1999.
- [Humphrey and Na, 2002] J. Humphrey and S. Na. *Elastodynamics and arterial wall stress*. Annals of Biomedical Engineering, vol. 30, no. 4, pages 509–523, 2002.
- [Ivankovic et al., 2002] A. Ivankovic, A. Karac, E. Dendrinis and K. Parker. *Towards early diagnosis of atherosclerosis: The finite volume method for fluid-structure interaction*. Biorheology, vol. 39, no. 4, pages 401–408, 2002.
- [Johnston et al., 1991] K. Johnston, R. Rutherford, M. Tilson, D. Shah, L. Hollier and J. Stanley. *Suggested standards for reporting on arterial aneurysms. Subcommittee on Reporting Standards for Arterial Aneurysms, Ad Hoc Committee on Reporting Standards, Society for Vascular Surgery and North American Chapter, International Society for Cardiovascular Surgery*. Journal of vascular surgery: official publication, the Society for Vascular Surgery [and] International Society for Cardiovascular Surgery, North American Chapter, vol. 13, no. 3, page 452, 1991, ISSN 0741-5214.
- [Juvela et al., 2001] S. Juvela, K. Poussa and M. Porras. *Factors affecting formation and growth of intracranial aneurysms: a long-term follow-up study*. Stroke, vol. 32, no. 2, page 485, 2001.
- [Kakalis et al., 2008] N. Kakalis, A. Mitsos, J. Byrne and Y. Ventikos. *The haemodynamics of endovascular aneurysm treatment: a computational modelling approach for estimating the influence of multiple coil deployment*. Medical Imaging, IEEE Transactions on, vol. 27, no. 6, pages 814–824, 2008, ISSN 0278-0062.
- [Kohn et al., 1999] L. Kohn, J. Corrigan, M. Donaldson et al.. *To err is human: building a safer health care system*. Institute of Medicine, published by National Academy of Sciences, 1999.

- [Komotar et al., 2008] R. Komotar, J. Mocco and R. Solomon. *Guidelines for the surgical treatment of unruptured intracranial aneurysms: the first annual J. Lawrence pool memorial research symposium-controversies in the management of cerebral aneurysms*. Neurosurgery, vol. 62, no. 1, page 183, 2008, ISSN 0148-396X.
- [Krummel, 1998] T. Krummel. *Surgical simulation and virtual reality: the coming revolution*. Annals of surgery, vol. 228, no. 5, page 635, 1998.
- [Kuehnafel and Neisius, 1993] U. Kuehnafel and B. Neisius. *CAD-based graphical computer simulation in endoscopic surgery*. Endoscopic surgery and allied technologies, vol. 1, no. 3, page 181, 1993.
- [Kunkler, 2006] K. Kunkler. *The role of medical simulation: an overview*. The International Journal of Medical Robotics and Computer Assisted Surgery, vol. 2, no. 3, pages 203–210, 2006, ISSN 1478-596X.
- [Küttler et al., 2010] U. Küttler, M. Gee, C. Förster, A. Comerford and W. Wall. *Coupling strategies for biomedical fluid–structure interaction problems*. International Journal for Numerical Methods in Biomedical Engineering, vol. 26, no. 3-4, pages 305–321, 2010.
- [Lakes and Vanderby, 1999] R. Lakes and R. Vanderby. *Interrelation of creep and relaxation: a modeling approach for ligaments*. TRANSACTIONS-AMERICAN SOCIETY OF MECHANICAL ENGINEERS JOURNAL OF BIOMECHANICAL ENGINEERING, vol. 121, no. 6, pages 612–615, 1999.
- [Larsson and Müller, 2011] M. Larsson and B. Müller. *Numerical Simulation of Fluid–Structure Interaction in Human Phonation: Verification of Structure Part*. Spectral and High Order Methods for Partial Differential Equations, pages 229–236, 2011.
- [Lasheras, 2007] J. Lasheras. *The biomechanics of arterial aneurysms*. Annu. Rev. Fluid Mech., vol. 39, pages 293–319, 2007, ISSN 0066-4189.
- [Lee, 1995] R. Lee. *Morphology of cerebral arteries*. Pharmacology & therapeutics, vol. 66, no. 1, pages 149–173, 1995, ISSN 0163-7258.
- [Levy, 1996] J. Levy. *Virtual reality hysteroscopy*. The Journal of the American Association of Gynecologic Laparoscopists, vol. 3, no. 4, Supplement, page S25, 1996, ISSN 1074-3804.
- [Liou and Liou, 1999] T. Liou and S. Liou. *A review on in vitro studies of hemodynamic characteristics in terminal and lateral aneurysm models*. Proceedings of the National Science Council, Republic of China. Part B, Life sciences, vol. 23, no. 4, page 133, 1999.

- [Long et al., 1998a] Q. Long, X. Xu, M. Collins, M. Bourne and T. Griffith. *Magnetic resonance image processing and structured grid generation of a human abdominal bifurcation*. Computer methods and programs in biomedicine, vol. 56, no. 3, pages 249–259, 1998a.
- [Long et al., 1998b] Q. Long, X. Xu, M. Collins, T. Griffith and M. Bourne. *The combination of magnetic resonance angiography and computational fluid dynamics: a critical review*. Critical reviews in biomedical engineering, vol. 26, no. 4, page 227, 1998b.
- [MacDonald et al., 2000] D. MacDonald, H. Finlay and P. Canham. *Directional wall strength in saccular brain aneurysms from polarized light microscopy*. Annals of Biomedical Engineering, vol. 28, no. 5, pages 533–542, 2000, ISSN 0090-6964.
- [Mantha et al., 2006] A. Mantha, C. Karmonik, G. Benndorf, C. Strother and R. Metcalfe. *Hemodynamics in a cerebral artery before and after the formation of an aneurysm*. American journal of neuroradiology, vol. 27, no. 5, page 1113, 2006.
- [Marescaux et al., 1998] J. Marescaux, J. Clément, V. Tasseti, C. Koehl, S. Cotin, Y. Russier, D. Mutter, H. Delingette and N. Ayache. *Virtual reality applied to hepatic surgery simulation: the next revolution*. Annals of Surgery, vol. 228, no. 5, page 627, 1998.
- [Marshall et al., 2004] I. Marshall, P. Papathanasopoulou and K. Wartolowska. *Carotid flow rates and flow division at the bifurcation in healthy volunteers*. Physiological Measurement, vol. 25, page 691, 2004.
- [Mazumdar, 1992] J. Mazumdar. *Biofluid mechanics*. World Scientific Pub Co Inc, 1992.
- [McGregor et al., 2009] R. McGregor, D. Szczerba, K. Muralidhar and G. Székely. *A fast alternative to computational fluid dynamics for high quality imaging of blood flow*. Medical Image Computing and Computer-Assisted Intervention–MICCAI 2009, pages 124–131, 2009.
- [McLeod et al., 2010] K. McLeod, A. Caiazzo, M. Fernández, T. Mansi, I. Vignon-Clementel, M. Sermesant, X. Pennec, Y. Boudjemline and J. Gerbeau. *Atlas-based reduced models of blood flows for fast patient-specific simulations*. Statistical Atlases and Computational Models of the Heart, pages 95–104, 2010.
- [Milner et al., 1998] J. Milner, J. Moore, B. Rutt and D. Steinman. *Hemodynamics of human carotid artery bifurcations: computational studies with models reconstructed from magnetic resonance imaging of normal subjects*. Journal of vascular surgery, vol. 28, no. 1, pages 143–156, 1998.

- [Monaghan, 2005] J. Monaghan. *Smoothed particle hydrodynamics*. Reports on Progress in Physics, vol. 68, page 1703, 2005.
- [Morales et al., 2011] H. Morales, M. Kim, E. Vivas, M. Villa-Uriol, I. Larrabide, T. Sola, L. Guimaraens and A. Frangi. *How Do Coil Configuration and Packing Density Influence Intra-Aneurysmal Hemodynamics?* American Journal of Neuroradiology, pages ajnr-A2635v1, 2011.
- [Mullen et al., 2011] P. Mullen, P. Memari, F. de Goes and M. Desbrun. *HOT: Hodge-optimized triangulations*. In *ACM Transactions on Graphics (TOG)*, vol. 30, page 103, ACM, 2011.
- [Nazari, 2010] S. Nazari. *Expandable device type III for easy and reliable approximation of dissection layers in sutureless aortic anastomosis. Ex vivo experimental study*. Interactive CardioVascular and Thoracic Surgery, vol. 10, no. 2, page 161, 2010.
- [Nazari et al., 1996] S. Nazari, F. Luzzana, C. Banfi, Z. Mourad, S. Salvi, A. Gaspari and F. Nazari-Coerezza. *Expandable prosthesis for sutureless anastomosis in thoracic aorta prosthetic substitution*. European journal of cardio-thoracic surgery, vol. 10, no. 11, page 1003, 1996.
- [Neil, 2009] J. Neil. *Simulation in Nursing Education*. Perioperative Nursing Clinics, vol. 4, no. 2, pages 97–112, 2009, ISSN 1556-7931.
- [Ning et al., 2010] G. Ning, Y. Gong, S. Gong, Q. Pan, J. Yan and A. Pries. *Simulation of Blood Pressure Wave Propagation in a Vessel by One-Dimensional Model*. In *6th World Congress of Biomechanics (WCB 2010). August 1-6, 2010 Singapore*, pages 1366–1369, Springer, 2010.
- [Paul et al., 2009] M. Paul, M. Mamun Molla and G. Roditi. *Large-Eddy simulation of pulsatile blood flow*. Medical Engineering & Physics, vol. 31, no. 1, pages 153–159, 2009.
- [Penney, 2002] D. Penney. *Hemodynamics*. 2002.
- [Peskin, 1972] C. Peskin. *Flow patterns around heart valves: a numerical method*. Journal of Computational Physics, vol. 10, no. 2, pages 252–271, 1972.
- [Popel and Johnson, 2005] A. Popel and P. Johnson. *Microcirculation and hemorheology*. Annual review of fluid mechanics, vol. 37, page 43, 2005.
- [Prakash and Ethier, 2001] S. Prakash and C. Ethier. *Requirements for mesh resolution in 3D computational hemodynamics*. Journal of biomechanical engineering, vol. 123, page 134, 2001.

- [Provenzano et al., 2001] P. Provenzano, R. Lakes, T. Keenan and R. Vanderby. *Nonlinear ligament viscoelasticity*. Annals of Biomedical Engineering, vol. 29, no. 10, pages 908–914, 2001.
- [Qiao and Liu, 2008] A. Qiao and Y. Liu. *Medical application oriented blood flow simulation*. Clinical Biomechanics, vol. 23, pages S130–S136, 2008.
- [Rappitsch and Perktold, 1996] G. Rappitsch and K. Perktold. *Pulsatile albumin transport in large arteries: a numerical simulation study*. Journal of biomechanical engineering, vol. 118, page 511, 1996.
- [Raymond et al., 2003] J. Raymond, F. Guilbert, A. Weill, S. Georganos, L. Juravsky, A. Lambert, J. Lamoureux, M. Chagnon and D. Roy. *Long-term angiographic recurrences after selective endovascular treatment of aneurysms with detachable coils*. Stroke, vol. 34, no. 6, pages 1398–1403, 2003.
- [Ren and Yuan, 2010] J. Ren and X. Yuan. *Mechanics of formation and rupture of human aneurysm*. Applied Mathematics and Mechanics, vol. 31, no. 5, pages 593–604, 2010, ISSN 0253-4827.
- [Richardson, 1911] L. Richardson. *The approximate arithmetical solution by finite differences of physical problems involving differential equations, with an application to the stresses in a masonry dam*. Philosophical Transactions of the Royal Society of London. Series A, Containing Papers of a Mathematical or Physical Character, vol. 210, pages 307–357, 1911, ISSN 0264-3952.
- [Sakalihan et al., 2005] N. Sakalihan, R. Limet and O. Defawe. *Abdominal aortic aneurysm*. The Lancet, vol. 365, no. 9470, pages 1577–1589, 2005, ISSN 0140-6736.
- [San Millán et al., 2002] R. San Millán, K. Tokunaga, A. Dehdashti, K. Sugiu, J. Delavelle and D. Rufenacht. *Is the rupture of cerebral berry aneurysms influenced by the perianeurysmal environment?* Acta neurochirurgica. Supplement, vol. 82, page 31, 2002, ISSN 0065-1419.
- [Satava, 1993] R. Satava. *Virtual reality surgical simulator. The first steps*. Surgical endoscopy, vol. 7, no. 3, page 203, 1993, ISSN 0930-2794.
- [Satava, 2008] R. Satava. *Historical review of surgical simulation—a personal perspective*. World Journal of Surgery, vol. 32, no. 2, pages 141–148, 2008, ISSN 0364-2313.
- [Sato et al., 2008] K. Sato, Y. Imai, T. Ishikawa, N. Matsuki and T. Yamaguchi. *The importance of parent artery geometry in intra-aneurysmal hemodynamics*. Medical engineering & physics, vol. 30, no. 6, pages 774–782, 2008, ISSN 1350-4533.

- [Sato et al., 2005] T. Satoh, M. Omi, C. Ohsako, A. Katsumata, Y. Yoshimoto, S. Tsuchimoto, K. Onoda, K. Tokunaga, K. Sugiu and I. Date. *Visualization of aneurysmal contours and perianeurysmal environment with conventional and transparent 3D MR cisternography*. American journal of neuroradiology, vol. 26, no. 2, page 313, 2005.
- [Schenk and Gärtner, 2006] O. Schenk and K. Gärtner. *On fast factorization pivoting methods for sparse symmetric indefinite systems*. Electronic Transactions on Numerical Analysis, vol. 23, pages 158–179, 2006.
- [Schirmer and Malek, 2010] C. Schirmer and A. Malek. *Critical Influence of Framing Coil Orientation on Intra-Aneurysmal and Neck Region Hemodynamics in a Sidewall Aneurysm Model*. Neurosurgery, vol. 67, no. 6, page 1692, 2010.
- [Schwartz et al., 2009] E. Schwartz, G. Langs, J. Holfeld, R. Gottardi, C. Loewe, P. Peloschek and M. Czerny. *Segmentation and Deformation Analysis of the Aorta in Gated CTA sequences in a MDL Framework*. In *Medical Image Understanding and Analysis*, vol. 13, pages 27–32, 2009.
- [Sharpe, 1997] R. Sharpe. *Differential geometry: Cartan's generalization of Klein's Erlangen program*, vol. 166. Springer Verlag, 1997.
- [Shojima et al., 2004] M. Shojima, M. Oshima, K. Takagi, R. Torii, M. Hayakawa, K. Katada, A. Morita and T. Kirino. *Magnitude and role of wall shear stress on cerebral aneurysm: computational fluid dynamic study of 20 middle cerebral artery aneurysms*. Stroke, vol. 35, no. 11, page 2500, 2004.
- [Shum et al., 2011] J. Shum, A. Xu, I. Chatnuntawech and E. Finol. *A Framework for the Automatic Generation of Surface Topologies for Abdominal Aortic Aneurysm Models*. Annals of biomedical engineering, pages 1–11, 2011.
- [Si, 2008] H. Si. *Adaptive tetrahedral mesh generation by constrained Delaunay refinement*. International Journal for Numerical Methods in Engineering, vol. 75, no. 7, pages 856–880, 2008.
- [Singh et al., 2009] P. Singh, A. Marzo, S. Coley, G. Berti, P. Bijlenga, P. Lawford, M. Villa-Uriol, D. Rufenacht, K. McCormack, A. Frangi et al.. *The role of computational fluid dynamics in the management of unruptured intracranial aneurysms: a clinicians' view*. Computational Intelligence and Neuroscience, vol. 2009, pages 1–12, 2009, ISSN 1687-5265.
- [Stam, 1999] J. Stam. *Stable fluids*. In *Proceedings of the 26th annual conference on Computer graphics and interactive techniques*, pages 121–128, ACM Press/Addison-Wesley Publishing Co., 1999.

- [Strother et al., 1992] C. Strother, V. Graves and A. Rappe. *Aneurysm hemodynamics: an experimental study*. American journal of neuroradiology, vol. 13, no. 4, page 1089, 1992.
- [Szilagyi et al., 1966] D. Szilagyi, R. Smith, F. DeRusso, J. Elliott and F. Sherrin. *Contribution of abdominal aortic aneurysmectomy to prolongation of life*. Annals of Surgery, vol. 164, no. 4, page 678, 1966.
- [Takeuchi and Karino, 2010] S. Takeuchi and T. Karino. *Flow patterns and distributions of fluid velocity and wall shear stress in the human internal carotid and middle cerebral arteries*. World Neurosurgery, vol. 73, no. 3, pages 174–185, 2010, ISSN 1878-8750.
- [Tateshima et al., 2007] S. Tateshima, K. Tanishita, H. Omura, J. Villablanca and F. Vinuela. *Intra-aneurysmal hemodynamics during the growth of an unruptured aneurysm: in vitro study using longitudinal CT angiogram database*. American journal of neuroradiology, vol. 28, no. 4, page 622, 2007.
- [Tateshima et al., 2010] S. Tateshima, A. Chien, J. Sayre, J. Cebral and F. Viñuela. *The effect of aneurysm geometry on the intra-aneurysmal flow condition*. Neuroradiology, pages 1–7, 2010, ISSN 0028-3940.
- [Tezduyar et al., 2008] T. Tezduyar, S. Sathe, M. Schwaab and B. Conklin. *Arterial fluid mechanics modeling with the stabilized space–time fluid–structure interaction technique*. International Journal for Numerical Methods in Fluids, vol. 57, no. 5, pages 601–629, 2008.
- [Thompson et al., 1999] J. Thompson, B. Soni and N. Weatherill. *Handbook of grid generation*. CRC, 1999.
- [Tong et al., 2006] Y. Tong, P. Alliez, D. Cohen-Steiner and M. Desbrun. *Designing quadrangulations with discrete harmonic forms*. In *Proceedings of the fourth Eurographics symposium on Geometry processing*, pages 201–210, Eurographics Association, 2006.
- [Tortoli et al., 2006] P. Tortoli, T. Morganti, G. Bambi, C. Palombo and K. Ramnarine. *Noninvasive simultaneous assessment of wall shear rate and wall distension in carotid arteries*. Ultrasound in medicine & biology, vol. 32, no. 11, pages 1661–1670, 2006, ISSN 0301-5629.
- [Tournois et al., 2009] J. Tournois, C. Wormser, P. Alliez and M. Desbrun. *Interleaving Delaunay refinement and optimization for practical isotropic tetrahedron mesh generation*. ACM Transactions on Graphics (TOG), vol. 28, no. 3, pages 1–9, 2009.

- [Tritton, 1959] D. Tritton. *Experiments on the flow past a circular cylinder at low Reynolds numbers*. Journal of Fluid Mechanics, vol. 6, no. 04, pages 547–567, 1959.
- [Turner et al., 1956] M. Turner, R. Clough, H. Martin and L. Topp. *Stiffness and deflection analysis of complex structures*. J. Aero. Sci, vol. 23, no. 9, pages 805–823, 1956.
- [Valencia et al., 2009] A. Valencia, P. Torrens, R. Rivera, M. Galvez and E. Bravo. *A mechanical study of patient-specific cerebral aneurysm models: The correlations between stress and displacement with geometrical indices*. Mechanics Research Communications, vol. 36, no. 5, pages 642–651, 2009, ISSN 0093-6413.
- [van de Vosse and Stergiopoulos, 2011] E. van de Vosse and N. Stergiopoulos. *Pulse Wave Propagation in the Arterial Tree*. Annual Review of Fluid Mechanics, vol. 43, no. 1, 2011.
- [Van Loon et al., 2004] R. Van Loon, P. Anderson, J. De Hart and F. Baaijens. *A combined fictitious domain/adaptive meshing method for fluid-structure interaction in heart valves*. International journal for numerical methods in fluids, vol. 46, no. 5, pages 533–544, 2004.
- [Van Loon et al., 2007] R. Van Loon, P. Anderson, F. Van de Vosse and S. Sherwin. *Comparison of various fluid-structure interaction methods for deformable bodies*. Computers & structures, vol. 85, no. 11-14, pages 833–843, 2007.
- [VanderZee et al., 2008] E. VanderZee, A. Hirani and D. Guoy. *Triangulation of simple 3D shapes with well-centered tetrahedra*. Proceedings of the 17th International Meshing Roundtable, pages 19–35, 2008.
- [Vanderzee et al., 2008] E. Vanderzee, A. Hirani, D. Guoy and E. Ramos. *Well-centered triangulation*. Arxiv preprint arXiv:0802.2108, 2008.
- [Vignon and Taylor, 2004] I. Vignon and C. Taylor. *Outflow boundary conditions for one-dimensional finite element modeling of blood flow and pressure waves in arteries*. Wave Motion, vol. 39, no. 4, pages 361–374, 2004.
- [Vignon-Clementel et al., 2010] I. Vignon-Clementel, C. Figueroa, K. Jansen and C. Taylor. *Outflow boundary conditions for 3D simulations of non-periodic blood flow and pressure fields in deformable arteries*. Computer Methods in Biomechanics and Biomedical Engineering, vol. 13, no. 5, pages 625–640, 2010.
- [Vito and Dixon, 2003] R. Vito and S. Dixon. *Blood vessel constitutive models-1995-2002*. Annual Review of Biomedical Engineering, vol. 5, no. 1, pages 413–439, 2003, ISSN 1523-9829.

- [Volokh and Vorp, 2008] K. Volokh and D. Vorp. *A model of growth and rupture of abdominal aortic aneurysm*. Journal of biomechanics, vol. 41, no. 5, pages 1015–1021, 2008, ISSN 0021-9290.
- [Wall and Rabczuk, 2008] W. Wall and T. Rabczuk. *Fluid–structure interaction in lower airways of CT-based lung geometries*. International Journal for Numerical Methods in Fluids, vol. 57, no. 5, pages 653–675, 2008.
- [Wang and Bernsdorf, 2009] D. Wang and J. Bernsdorf. *Lattice Boltzmann simulation of steady non-Newtonian blood flow in a 3D generic stenosis case*. Computers & Mathematics with Applications, vol. 58, no. 5, pages 1030–1034, 2009.
- [Wang et al., 2006] K. Wang et al.. *Edge subdivision schemes and the construction of smooth vector fields*. ACM Transactions on Graphics (TOG), vol. 25, no. 3, pages 1041–1048, 2006.
- [Warren et al., 2007] J. Warren, S. Schaefer, A. Hirani and M. Desbrun. *Barycentric coordinates for convex sets*. Advances in computational mathematics, vol. 27, no. 3, pages 319–338, 2007.
- [Wei and Cotin, 2012] Y. Wei and S. Cotin. *Aneurysm: A (Near) Real-Time Simulation Method of Aneurysm Coil Embolization, in progress*. InTech, 2012, ISBN 980-953-307-299-4.
- [Wei et al., 2009] Y. Wei, S. Cotin, L. Fang, J. Allard, C. Pan and S. Ma. *Toward Real-Time Simulation of Blood-Coil Interaction during Aneurysm Embolization*. Medical Image Computing and Computer-Assisted Intervention–MICCAI 2009, pages 198–205, 2009.
- [Wei et al., 2010] Y. Wei, L. Fang, S. Cotin and S. Ma. *Interactive Blood-Coil Simulation using Discrete Exterior Calculus*. International Conference on Vortex Flows and Vortex Models–ICVFM, 2010.
- [Wei et al., 2011] Y. Wei, S. Cotin, J. Allard, L. Fang, C. Pan and S. Ma. *Interactive blood-coil simulation in real-time during aneurysm embolization*. Computers & Graphics, 2011.
- [Weinberg et al., 2010] E. Weinberg, D. Shahmirzadi and M. Mofrad. *On the multiscale modeling of heart valve biomechanics in health and disease*. Biomechanics and modeling in mechanobiology, pages 1–15, 2010.
- [Wetzel et al., 2007] S. Wetzel, S. Meckel, A. Frydrychowicz, L. Bonati, E. Radue, K. Scheffler, J. Hennig and M. Markl. *In vivo assessment and visualization of intracranial arterial hemodynamics with flow-sensitized 4D MR imaging at 3T*. American journal of neuroradiology, vol. 28, no. 3, page 433, 2007.

- [Wilson et al., 1997] M. Wilson, A. Middlebrook, C. Sutton, R. Stone and R. McCloy. *MIST VR: a virtual reality trainer for laparoscopic surgery assesses performance*. Annals of the Royal College of Surgeons of England, vol. 79, no. 6, page 403, 1997.
- [Wilt et al., 2006] T. Wilt, M. E. based Practice Center, U. S. A. for Healthcare Research and Quality. *Comparison of endovascular and open surgical repairs for abdominal aortic aneurysm*. Agency for Healthcare Research Quality, 2006.
- [Zhao et al., 2008] J. Zhao, W. Yin, G. Ding, X. Yang, W. Shi and X. Zhang. *Numerical simulation and analysis on the hemodynamics of an elastic aneurysm*. Journal of Hydrodynamics, vol. 20, no. 2, pages 216–224, 2008, ISSN 1001-6058.
- [Zhao et al., 2009] J. Zhao, G. Ding, W. Yin, X. Yang, W. Shi and X. Zhang. *Analysis and Comparison of 2-D Hemodynamic Numerical Simulation of Elastic Aneurysm and Rigid Aneurysm*. New Trends in Fluid Mechanics Research, pages 614–617, 2009.